Journal of Nanomaterials

Nanostructure Materials as a Promising Route for Efficient Renewable Energy Production, Storage, and Conversion

Lead Guest Editor: Nour F. Attia
Guest Editors: Ben Slama Sami, Sally El Ashary, and Jamal Siddiqui

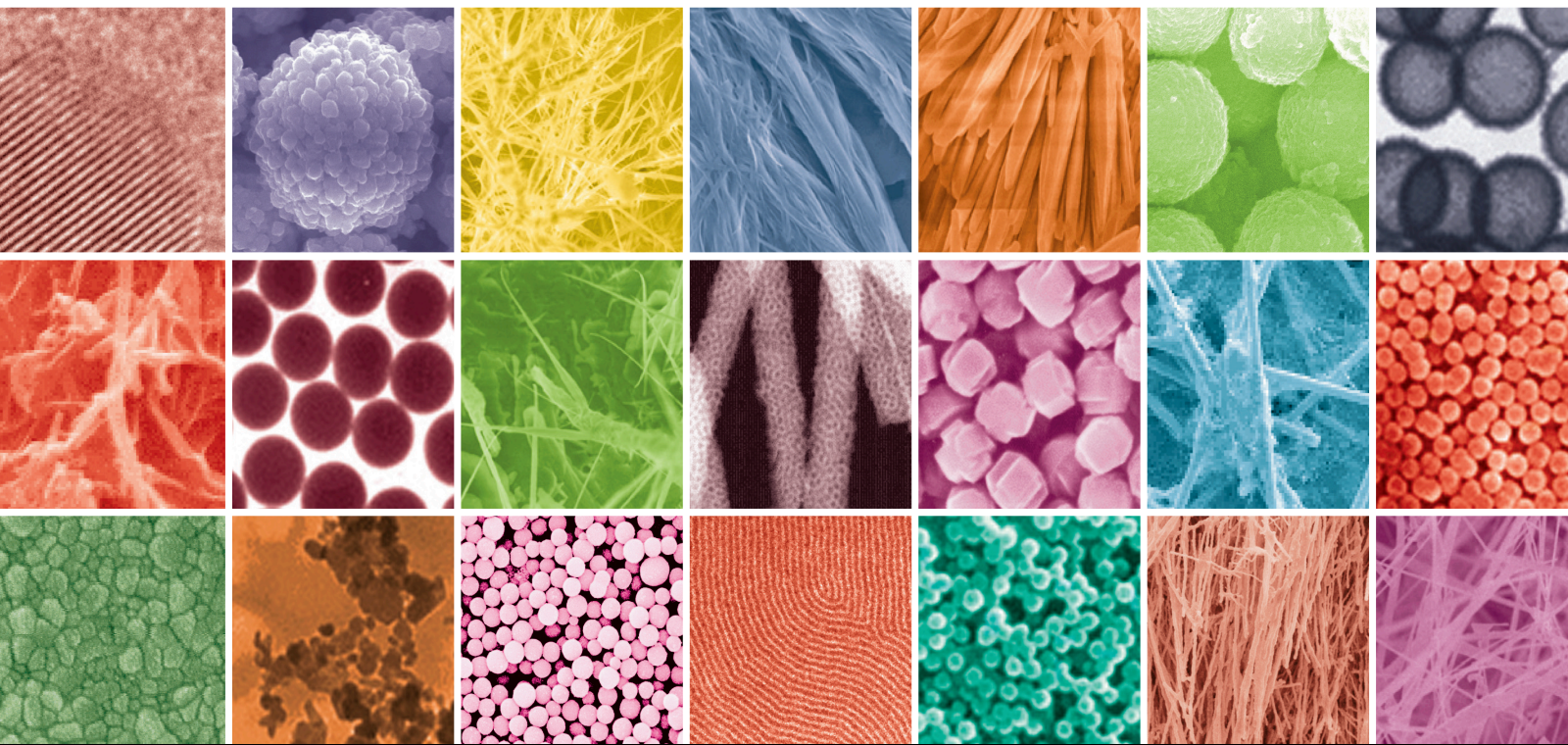

Nanostructure Materials as a Promising Route for Efficient Renewable Energy Production, Storage, and Conversion

Journal of Nanomaterials

Nanostructure Materials as a Promising Route for Efficient Renewable Energy Production, Storage, and Conversion

Lead Guest Editor: Nour F. Attia
Guest Editors: Ben Slama Sami, Sally El Ashary, and Jamal Siddiqui

Editorial Board

Contents

Hindawi
Journal of Nanomaterials
Volume 2020, Article ID 7261625, 1 page
https://doi.org/10.1155/2020/7261625

Editorial

Nanostructure Materials as a Promising Route for Efficient Renewable Energy Production, Storage, and Conversion

Nour F. Attia,[1,2] **Slama Sami**,[3] **Sally E. A. Elashery**,[4] **and Jamal Siddiqui**[5]

[1]*Fire Protection Laboratory, Chemistry Division, National Institute for Standards, 136, Giza 12211, Egypt*
[2]*Department of Energy Engineering, Gyeongnam National University of Science and Technology (GNTECH), Jinju 52725, Republic of Korea*
[3]*Jeddah Community College, King Abdulaziz University, Jeddah, Saudi Arabia*
[4]*Chemistry Department, Faculty of Science, Cairo University, Gamaa Str., 12613 Giza, Egypt*
[5]*Department of Chemistry, School of Basic Sciences and Humanity, Lingaya's University, India*

Correspondence should be addressed to Nour F. Attia; drnour2005@yahoo.com

Received 21 January 2020; Accepted 22 January 2020; Published 31 January 2020

The rapid growth of worldwide population in conjunction with expansion in industry sectors in the world attributed to huge consumption of limited stock fossil fuels. Hence, this expected energy crisis forced the world to find a clean renewable source of energy instead of consumable fossil fuel one. Therefore, there are intensive efforts to use solar energy, wind energy, and hydrogen energy. However, the production, storage, and conversion of these kinds of energy sources require development of smart materials to facilitate their rapid commercialization. On the other hand, the nanomaterials have received intensive scientists' interest for various applications due to their outstanding chemical, physical, mechanical, electrical, and electronic properties. Hence, the harness of unique properties of materials and their hybrid nanocomposites will be much appreciated and demanded to be used in energy-related applications such as production, storage, and conversion. Therefore, in this special issue, we invited the scientists and researchers all over the world to submit their original novel work based on nanomaterials for solar cells, fuel cells, hydrogen storage and production, hybrid nanocomposites, and supercapacitors. In conclusion, we are happy to announce the publication of four original research papers and one review in the field of nanostructure materials as a promising route for efficient renewable energy applications.

Conflicts of Interest

There is no conflict of interest to declare.

Acknowledgments

The lead guest editor would like to thank all authors who contributed in this special issue and the scientists who reviewed the manuscripts, also the guest editors who shared their time and effort to have this issue published.

Nour F. Attia
Slama Sami
Sally E. A. Elashery
Jamal Siddiqui

Hindawi
Journal of Nanomaterials
Volume 2019, Article ID 1562130, 17 pages
https://doi.org/10.1155/2019/1562130

Review Article

Recent Developments in Nanostructured Palladium and Other Metal Catalysts for Organic Transformation

S. M. Shakil Hussain[1], **Muhammad Shahzad Kamal**[1] **and Mohammad Kamal Hossain**[2]

[1]*Center for Integrative Petroleum Research, King Fahd University of Petroleum & Minerals, Dhahran 31261, Saudi Arabia*
[2]*Center of Research Excellence in Renewable Energy (CoRERE), King Fahd University of Petroleum & Minerals, Dhahran 31261, Saudi Arabia*

Correspondence should be addressed to Muhammad Shahzad Kamal; shahzadmalik@kfupm.edu.sa

Received 16 April 2019; Revised 25 August 2019; Accepted 12 September 2019; Published 20 October 2019

Guest Editor: Sally El Ashery

Nanocatalysis is an emerging field of research and is applicable to nearly all kinds of catalytic organic conversions. Nanotechnology is playing an important role in both industrial applications and academic research. The catalytic activities become pronounced as the size of the catalyst reduces and the surface area-to-volume ratio increases which ultimately enhance the activity and selectivity of nanocatalysts. Similarly, the morphology of the particles also has a great impact on the activity and selectivity of nanocatalysts. Moreover, the electronic properties and geometric structure of nanocatalysts can be affected by polar and nonpolar solvents. Various forms of nanocatalysts have been reported including supported nanocatalysts, Schiff-based nanocatalysts, graphene-based nanocatalysts, thin-film nanocatalysts, mixed metal oxide nanocatalysts, magnetic nanocatalysts, and core-shell nanocatalysts. Among a variety of different rare earth and transition metals, palladium-based nanocatalysts have been extensively studied both in academia and in the industry because of their applications such as in carbon-carbon cross-coupling reactions, carbon-carbon homocoupling reactions, carbon-heteroatom cross-coupling reactions, and C-H activation, hydrogenation, esterification, oxidation, and reduction. The current review highlights the recent developments in the synthesis of palladium and some other metal nanocatalysts and their potential applications in various organic reactions.

1. Introduction

After realizing the unique morphological, structural, and optoelectrical characteristics of nanomaterials, their wide range of applications has been explored in various fields [1]. These include environmental, energy harnessing, biomedical sector, and catalysis [2–7]. The chemical process that involves the use of nanomaterials as a catalyst can be termed as nanocatalysis, while the nanomaterial can be termed as nanocatalyst. Based on their morphologies, nanocatalysts can be classified into zero-dimensional (0D), one-dimensional (1D), two-dimensional (2D), and three-dimensional (3D) structures [8]. The control dimensions of these materials induced specific physicochemical characteristics, which make them special for the catalysis industry [9]. More recently, researchers show significant inclination to use nanocatalysts in advance heterogeneous and homogenous catalysis applications [10]. A number of reviews in the area gave an insightful view into the prospects of nanostructured catalysis [11–14]. The catalyst system composed of nanoparticles/nanocomposites showed greater catalytic activity and selectivity because of its morphology and nano-dimensional characteristics. Though many materials have been utilized as nanocatalysts in industries, transition metal NPs have received significant attention due to their unique physicochemical characteristics, abundant availability, and more importantly, consumer-friendly costs. It is well established that the size, morphology, and solvents play a key role in the catalytic activity, selectivity, and stability of the nanocatalysts [15].

The present review is an attempt to realize the current development and prospects in nanostructured catalysts, especially for organic synthesis. The beginning portion of the review is dedicated to the effect of various factors on the

overall performance of nanocatalysts. This is followed by a critical overview of organic transformations, with a few case studies on Pd, Pt, Fe, Cu, Ag, Au, and Zn NPs, as well as other examples. In the later part of the review, some insights are provided through the Conclusion along with a few future recommendations about the future potential of nanostructured catalysts.

2. Factors Affecting the Performance of Nanocatalysts

There are several factors that affect the performance of nanocatalysts. However, this section will mainly focus on three important factors which include particle size, particle shape, and solvent.

2.1. Particle Size Effect of Nanocatalysts. Over the past few years, significant research has been conducted to identify the effect of nanoparticle size on catalytic performance for various chemical transformations [16]. As the particle size decreases, their surface area-to-volume ratio is enhanced, allowing more atoms on the surface to take part in the reaction [17]. As a result, improved catalyst activity and selectivity can be achieved. The particle size is very important for the development of highly active and selective catalysts as well as for the reduction of catalyst loading. Yoo et al. found better electrocatalytic and electronic properties by decreasing the size of Pt/TiO_2 nanocatalysts [18]. Bond and Thompson discovered that the catalytic activity of gold nanoparticles depends on their size, support system, and synthesis methods [19]. The gold catalyst is composed of very small-sized particles (<5 nm) and is supported by TiO_2. Before such discovery, gold was assumed to be the least catalytically active metal. Li et al. synthesized palladium nanoparticle-graphene hybrids and investigated the catalytic activities of such Pd-graphene hybrids in Suzuki reaction under aerobic and aqueous conditions [20]. It was observed that a palladium-graphene hybrid with a 4 nm particle size of palladium gave a 100% yield along with 95.5% selectivity. However, a palladium-graphene hybrid with a 15 nm particle size of palladium gave a 93.7 yield along with 95.2% selectivity.

2.2. Particle Shape Effect of Nanocatalysts. The shaped-controlled synthesis of catalytic materials is widely regarded to control some important physicochemical properties of nanocatalysts [21]. Many reports are available in the literature in this regard. For instance, hemispherical gold nanoparticles gave better results as compared to spherical-shaped gold nanoparticles for the oxidation of carbon monoxide (CO) even at low temperature [22]. In 2005, Henry reported a brief review with practical examples regarding the effect of nanoparticle shape on their properties in numerous developing technologies [23]. Narayanan and El-Sayed synthesized tetrahedral- and cubic-shaped platinum nanoparticles and studied the relationship of shape reactivity [24]. Shape control is significantly reported for photocatalytic applications in the literature. Khan and Qurashi synthesized highly controlled platelet-shaped copper vanadate nanocatalysts for PEC water splitting and compared the results with NPs of conventional shape. It was determined that the shape-controlled copper vanadate enhanced the light trapping properties of the catalyst and hence enhanced the photoelectrochemical performance of the catalyst [25].

Similarly, shape-controlled NPs are also found useful in organic conversion to some extent. As reported by Luo et al., shape-controlled synthesis of Rh-based nanocrystals and supported Rh-based nanocatalysts was found efficient in heterogeneous conversions such as in methane conversion and olefin hydroformylation [26].

2.3. Solvent Effect on Nanocatalysts. A solvent has a significant impact on the reaction pathway, reaction energy, and activation energy. The geometric structure and the electronic properties of nanoparticles can be influenced by the interaction of a solvent and metal atoms. Dufour et al. reported the effects of solvents on the electronic and structural properties of small gold clusters [27]. Li and Liu demonstrated the geometrical, electronic, and photocatalytic properties of titania anatase nanoparticles in aqueous media [28]. A comprehensive study of the effects of polar and nonpolar solvents on electronic and geometrical properties of nanocatalysts was conducted by Hou et al., and it was noted that a polar solvent has a great impact on the properties of nanocatalysts. It was observed that the ionization potential decreased by increasing the polarity of the solvent. Therefore, it was easier for neutral species to donate an electron in the solvent. Moreover, the electron-donating ability of a neutral species is considerably increased in a polar solvent as compared to that in a nonpolar solvent [29]. Recently, Chowdhury et al. synthesized palladium nanoparticles in an aqueous dimethyl formamide (DMF) solvent with a changing composition of DMF. Different shapes and geometries of palladium nanoparticles, such as hexagonal, cuboidal, and triangular plates, were obtained by varying the composition of DMF. It was emphasized that the various geometries of palladium nanoparticles are due to the blocking and interaction of DMF to some planes of nanoparticles leading to different geometries [30].

3. Major Nanocatalysts for Organic Synthesis

A huge number of metals have been investigated for organic transformations, and these metals showed better results in the formation of pharmaceuticals, fine chemicals, and new materials [31]. Among the varieties of different rare earth and transition metals, palladium is one of the most widely used transition metal for carbon-carbon coupling reactions, and palladium-based nanocatalysts have been extensively studied both in academia and in industry because of their applications such as in sensors, fuel cell catalysts, hydrogen storage, dechlorination, and organic transformations. Therefore, we mainly focused on the current development of palladium-based nanocatalysts for cross-coupling reactions. However, some other metals which have been successfully applied in this field have also been highlighted.

3.1. Palladium-Based Nanocatalyst

3.1.1. Palladium-Based Nanocatalysts for Carbon-Carbon Cross-Coupling Reactions. Palladium-assisted nanocatalysts

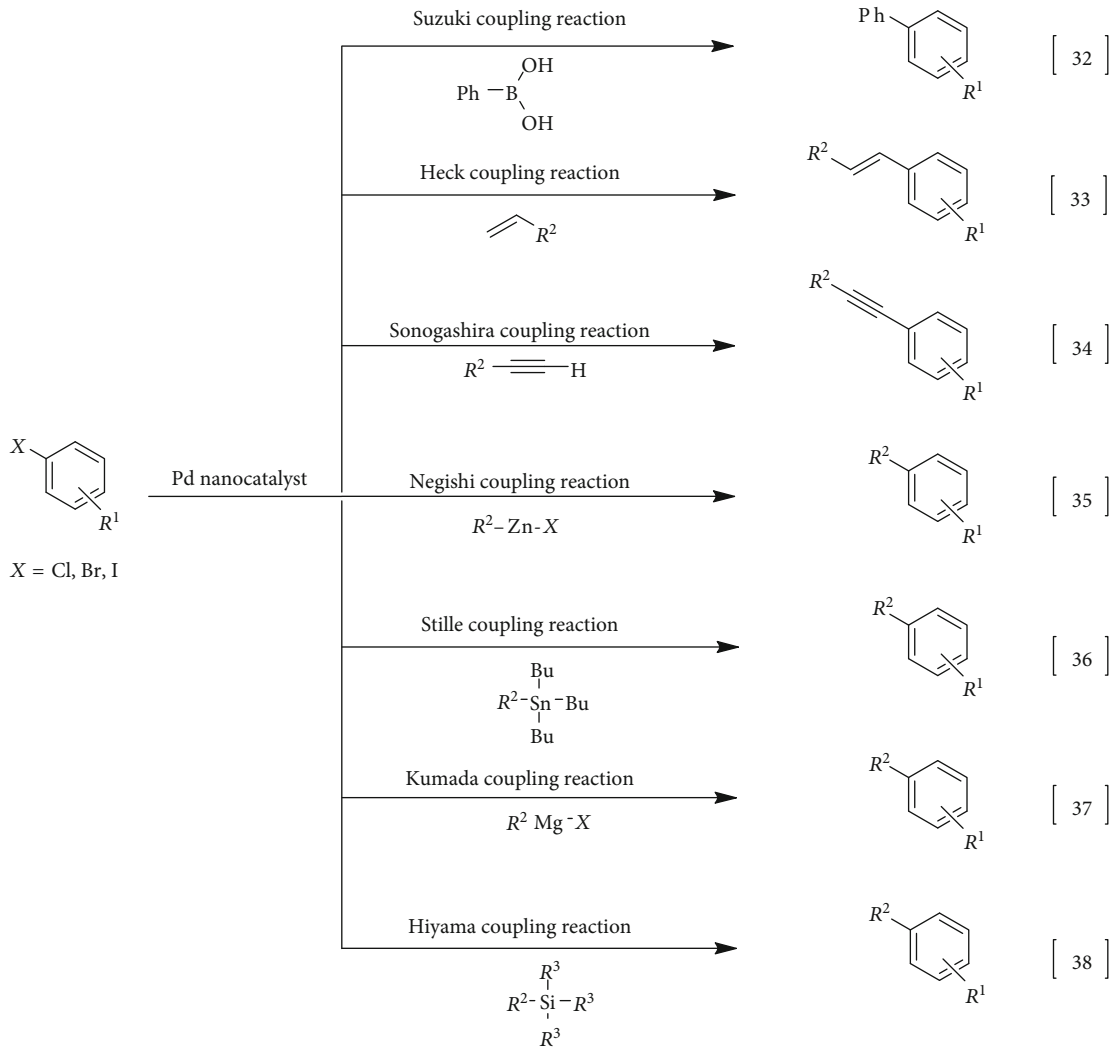

Scheme 1: Palladium-based nanocatalysts for carbon-carbon cross-coupling reactions.

for carbon-carbon bond formation including Suzuki [32], Heck [33], Sonogashira [34], Negishi [35], Stille [36], Kumada [37], and Hiyama [38] cross-coupling reactions (Scheme 1) have made a huge impact on organic reactions because of mild reaction conditions and tolerance to various functional groups [39]. Such kinds of reactions showed extensive applications in the formation of pharmaceuticals, agrochemicals, and other important industrial products [40].

Among the various carbon-carbon coupling reactions, Suzuki, Heck, and Sonogashira reactions are the most important reactions and play a central role in the formation of natural products, pharmaceutical, and agrochemicals [41]. Table 1 lists the various metal nanoparticles for catalyzing Suzuki, Heck, and Sonogashira cross-coupling reactions.

[a]Isolated yield. [b]GC yield. [c]Yield after work-up.

Within the framework of carbon-carbon cross-coupling reactions, the Suzuki reaction is the most extensively used reaction and it has been the benchmark for identifying the catalytic activity of newly prepared metal nanoparticles. In 2008, Kim et al. synthesized bimetallic nanoparticles (Pd-Ag, Pd-Ni, and Pd-Cu) on carbon support through the γ-irradiation technique for Suzuki and Heck cross-coupling reactions [52]. The catalytic efficiency of these supported bimetallic nanoparticles in Suzuki reaction were in the order of Pd – Cu/C > Pd/C > Pd – Ag/C > Pd – Ni/C based on the reaction yield 97.5% > 96.7% > 92.3% > 38.5%, respectively.

The various metal nanocatalysts used in the Suzuki reaction are listed in Table 2.

[a]Isolated yield. [b]GC yield.

3.1.2. Mechanism of Cross-Coupling Reactions. The reactants meet on a palladium atom and become so close together that reaction takes place. The major role of palladium and the other metals is to enable and encourage two coupling partners to undergo a chemical reaction. In 1972, Kumada et al. suggested that the catalytic cycle of a cross-coupling reaction occurs in three steps including oxidative addition, transmetalation, and reductive elimination (Scheme 2) [67].

The reaction mechanism usually begins with the zero-valent palladium (Pd^o) which undergoes oxidative addition (step 1) by reacting with an organic electrophile to form a Pd (II) species [68]. Usually, step 1 is the rate-determining step in this three-step catalytic cycle. Subsequently, transmetalation (step 2) occurs in the presence of a base for the

Table 1: Palladium-based nanocatalysts for carbon-carbon coupling reactions.

Catalyst (amount)	Substrate (1 mmol)	Substrate (2 mmol)	Coupling product	Base	Solvent	T (°C)	Time (h)	Reaction name	Yield (%)	Ref.
Pd-SMU-MNPs (8 mg)	PhI (1)	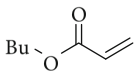 (1.2)	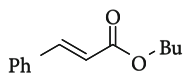	K_2CO_3	DMF	120	1.5	Heck	95[a]	[42]
Fe_3O_4@CS-Schiff-based Pd catalyst (10 mg)	PhI (1)	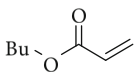 (1.2)	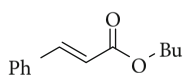	Et_3N	DMF	120	0.3	Heck	98[a]	[43]
Stabilized Pd-NPs (1 mol%)	ArI (0.5)	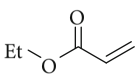 (0.6)	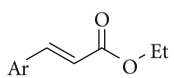	$CsCO_3$	DMF	110	2	Heck	95[a]	[41]
Pd/NH_2-SiO_2 (0.05 mol%)	PhI (1)	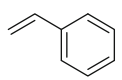 (1.2)	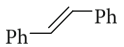	K_2CO_3	DMF	110-120	2	Heck	95[a]	[44]
Pd-PVP-Fe (0.004 g)	PhBr (1)	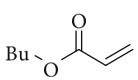 (1)	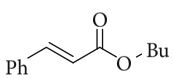	K_2CO_3	DMF	RT	0.5	Heck	91[a]	[33]
OXDH-Pd-NPs (0.0091 mmol)	ArI (6.3)	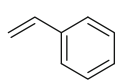 (5.8)	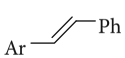	Na_2CO_3	NMP : H_2O (1 : 1)	80	0.5	Heck	97[a]	[45]
Au/Pd-NPs (0.3 mol%)	PhI (1)	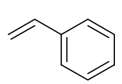 (1.5)	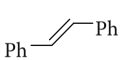	K_2CO_3	H_2O	80	8	Heck	89[c]	[46]
Fe_3O_4@SiO_2/isoniazide/Pd (10 mg)	PhI (1)	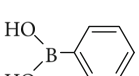 (1.1)		K_2CO_3	EtOH : H_2O (1 : 1)	25	0.5	Suzuki	96[a]	[47]
Pd-NP-HNG (0.025 mol%)	PhI (1)	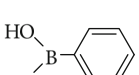 (1.3)		K_2CO_3	EtOH : H_2O (1 : 1)	60	2.5	Suzuki	98[a]	[48]

Table 1: Continued.

Catalyst (amount)	Substrate (1 mmol)	Substrate (2 mmol)	Coupling product	Base	Solvent	T (°C)	Time (h)	Reaction name	Yield (%)	Ref.
PdCo ANP-PPI-g-graphene (0.004 g)	PhI (1)	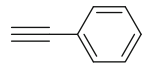 (1)		K_2CO_3	None	25	1	Sonogashira	99[b]	[49]
Pd tripods (2 mol%)	PhI (0.49)	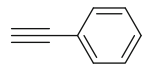 (0.74)	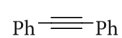	KOH	H_2O	100	6	Sonogashira	93[a]	[50]
Pd@MWCNTs (1 mmol%)	PhI (1)	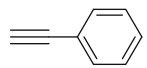 (1.2)	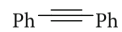	K_2CO_3	MeOH : H_2O (3 : 1)	Reflux	2.5	Sonogashira	71[a]	[51]
Pd/NH_2-SiO_2 (0.05 mol%)	PhI (1)	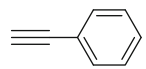 (1.5)	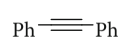	K_2CO_3	EG	120	2	Sonogashira	98[a]	[44]
Stabilized Pd-NPs (1 mol%)	PhI (0.5)	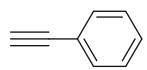 (0.6)	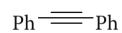	$CsCO_3$	MeOH	90	22	Sonogashira	91[a]	[41]

Table 2: Suzuki reaction with various metal nanocatalysts

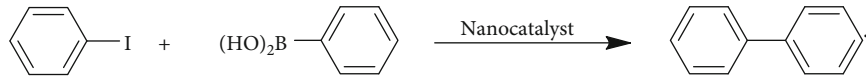

Nanocatalyst (amount)	PhI	$PhB(OH)_2$	Base	Solvent	T (°C)	Time (h)	Yield (%)	Ref.
Pd-SMU-MNPs (6 mg)	1	1	K_2CO_3	PEG	50	0.5	97[a]	[42]
Cu-C (0.1 mol%)	1	1.2	K_2CO_3	H_2O	50	3	96[a]	[53]
Fe_3O_4NPs/IL/Pd(0) (0.2 mol%)	1	1.1	K_2CO_3	H_2O/EtOH (1 : 1)	RT	0.25	96[a]	[54]
Au-graphene (1 mol%)	1	1.2	NaOH	H_2O	100	4	85[b]	[55]
Pd/TiO_2 (0.7 mol%)	1	1.1	Na_2CO_3	NMP : H_2O (2.5 : 1)	120	4	97[a]	[56]
Ru/Al_2O_3 (5 mol%)	1	1.5	NaOH	DME/H_2O (1 : 1)	60	1	96[a]	[57]
Pd@MWCNTs (1 mmol%)	1	1.2	K_2CO_3	MeOH : H_2O (3 : 1)	Reflux	2.5	84[b]	[51]
PVP-stabilized Pd-NPs (0.07 mol%)	0.5	0.75	K_3PO_4	H_2O : EtOH (3 : 1)	90	24	97[b]	[58]
Pd/NH_2-SiO_2 (0.05 mol%)	1	1.2	K_2CO_3	H_2O (2 mL)	60-70	1	96[a]	[44]
Fe_3O_4@CS-Schiff-based Pd catalyst (10 mg)	1	1.2	K_2CO_3	PEG	80	0.17	98[a]	[43]
Pd-Ni@Fe_3O_4 (0.0026 mol% of Pd and 0.001 mol% of Ni))	0.5	0.75	K_2CO_3	EtOH	80	0.25	94[a]	[59]
Pd/r-GO NP thin film	1	1.2	K_2CO_3	H_2O	80	0.25	>99[a]	[60]
LDH-DS-Pd(0) (0.5 mol%)	1	1.2	K_2CO_3	DMF/H_2O 6 mL (5 : 1, v/v)	80	5	93[a]	[61]
Pd@$MTiO_2$ (0.03 g)	1	1.2	K_2CO_3	H_2O	70	3	99[b]	[62]
Carbon nanocomposite Pd catalyst (1 mol%)	0.5	0.6	K_2CO_3	DMF/H_2O (2 : 1)	100	1.5	97[b]	[63]
Core-shell-like Ni-Pd/CB catalyst (5.5 mg, 0.1 mol% Pd)	2.5	2.75	K_2CO_3	EtOH/H_2O (1 : 1)	30	0.5	90[a]	[64]
Au-G nanocomposite (0.05 g)	1	1.5	K_2CO_3	H_2O	RT	4	99[b]	[65]
Sr/Alg/CMC/GO/Au (0.005 mol%)	2	2.4	NaOH	H_2O	80	4	98[a]	[66]
OXDH-Pd-NPs (0.0091 mmol)	5.41	4.92	Na_2CO_3	1,4 Dioxane/water (1 : 1)	80	1	98[a]	[45]
Stabilized Pd-NPs (1 mol%)	0.5	0.75	KF	DMF : H_2O (1 : 1)	RT	24	93[a]	[41]

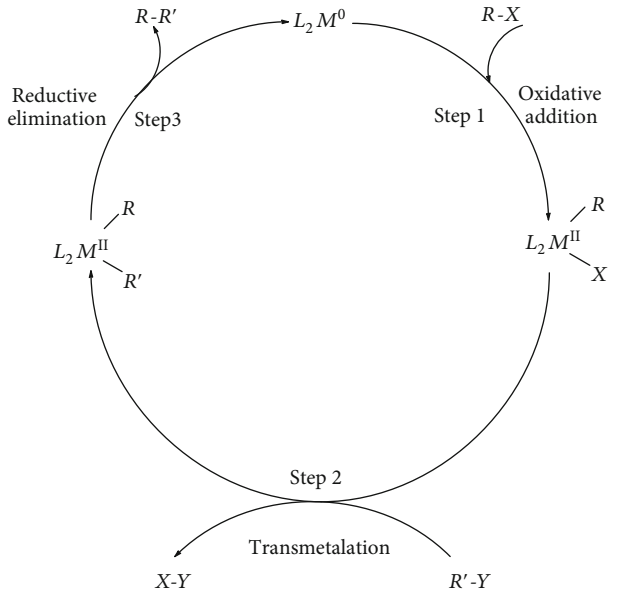

Scheme 2: The proposed mechanism of cross-coupling reactions.

transfer of R' towards a less electropositive metal. In this step, both coupling partners join the same metal center while removing the functional groups. At the end (step 3), reductive elimination occurs which leads to the formation of a new carbon-carbon bond as well as the regeneration of a zero-valent palladium species which is ready for another cycle. An unsaturated organic species was found to undergo a faster coupling reaction by following the order vinyl – vinyl > phenyl – phenyl > alkynyl – alkynyl > alkyl – alkyl.

3.1.3. Palladium-Based Nanocatalysts for Carbon-Heteroatom Cross-Coupling Reactions. Palladium nanocatalysts have been successfully applied in carbon-heteroatom cross-coupling reactions such as in Buchwald-Hartwig amination. Recently, Panahi et al. reported an immobilized palladium nanocatalyst on a silica-starch substrate (PNP-SSS) as an effective catalyst for carbon-nitrogen cross-coupling reactions through Buchwald-Hartwig amination with excellent catalytic activity and reusability [69] (Scheme 3).

Most recently, Hajipour et al. studied the efficiency of a palladium nanocatalyst supported on cysteine-functionalized magnetic nanoparticles for *N*- and *O*-arylation reactions in environmentally friendly conditions [70]. The authors claimed that the synthesized palladium catalyst system exhibited excellent recyclability with no substantial deactivation even after ten cycles (Scheme 4).

Similarly, Veisi et al. also reported a carbon-heteroatom cross-coupling reaction using a palladium nanocatalyst immobilized on carbon nanotubes and observed no change in catalytic activity for up to six cycles (Scheme 5) [71].

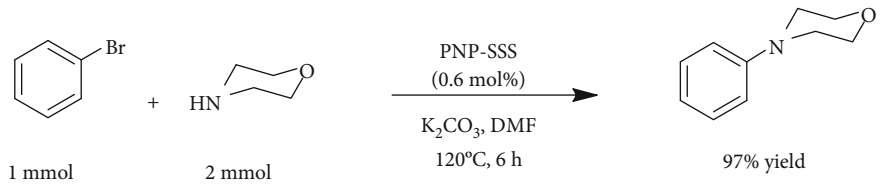

Scheme 3: Buchwald-Hartwig amination using PNP-SSS [69].

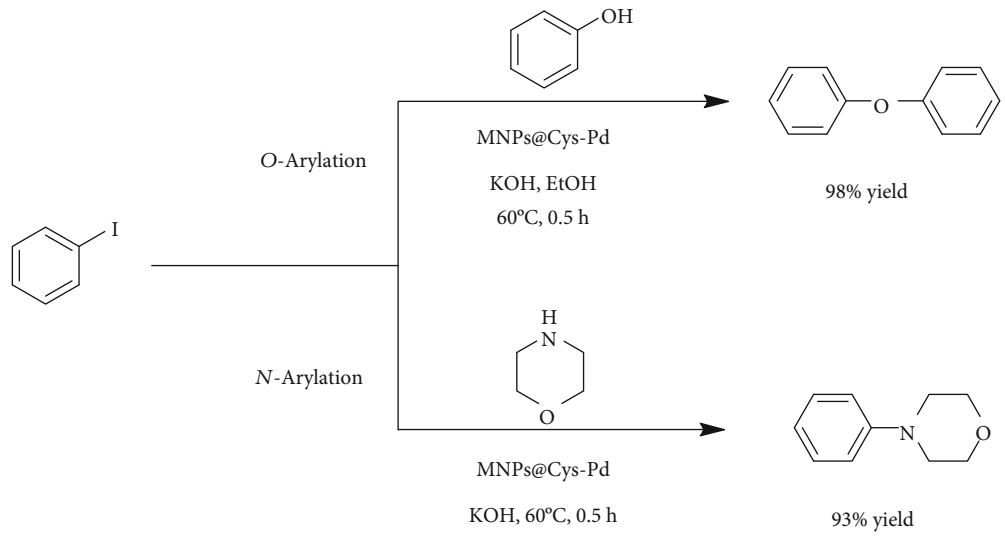

Scheme 4: *N*- and *O*-arylation using a cysteine-supported palladium nanocatalyst.

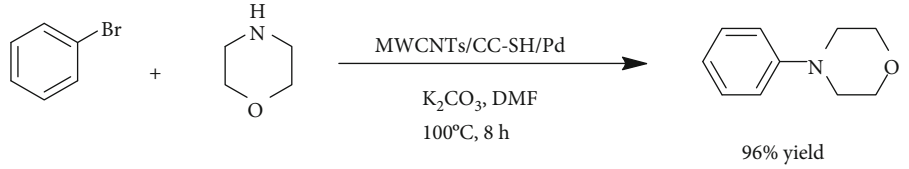

Scheme 5: C-N cross-coupling reaction using a palladium nanocatalyst immobilized on carbon nanotubes.

3.1.4. Palladium-Based Nanocatalysts for Carbon-Carbon Homocoupling Reactions. The biaryl formation is a very important reaction in the field of catalysis, total synthesis, fine chemicals, and supramolecular chemistry [72]. The bond between two aryl groups is often available in natural products, dyes, medicine, and agrochemicals. The copper-catalyzed homocoupling reaction is a well-known method for the construction of biaryls, but it requires harsh reaction conditions. Movahed et al. reported palladium nanoparticles on nitrogen-doped graphene (Pd-NP-HNG) for an Ullmann-type homocoupling reaction in water (Scheme 6) [48].

Recently, Rafiee et al. reported the synthesis of a palladium nanocatalyst immobilized on a magnetic few-layer graphene support which they applied on cross- and homocoupling reactions [73]. The catalyst system was found to be active up to six runs with no loss of its catalytic activity (Scheme 7).

Liu et al. prepared a series of polyaniline-supported palladium nanocatalysts for the Ullmann homocoupling reaction of aryl iodides to form biaryls. It was observed that the catalyst activity can be tuned by introducing electron-donating groups (Scheme 8) [74].

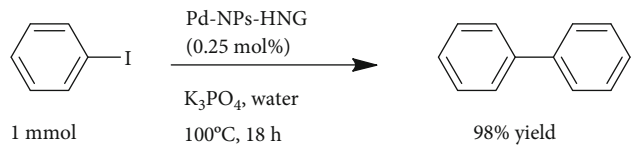

Scheme 6: Ullmann homocoupling reaction using Pd-NP-HNG nanocatalysts [48].

3.1.5. Palladium-Based Nanocatalyst for Hydrogenation Reactions. A palladium catalyst has faster hydrogenation and dehydrogenation processes and are also used in petroleum cracking. A variety of hydrogenation reactions are conducted by palladium nanocatalysts. A palladium nanocatalyst has the capability to combine with a wide range of ligands for highly selective organic reactions. Research is more focused on supported palladium nanoparticles due to their excellent

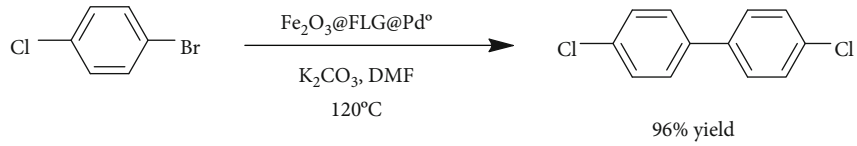

Scheme 7: Homocoupling reaction of 4-chloro-1-bromo benzene using a Fe_2O_3@FLG@Pd° catalyst.

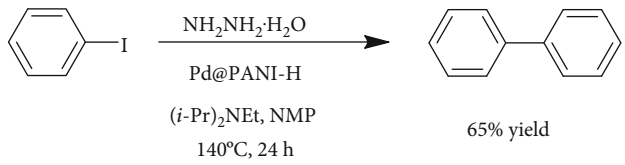

Scheme 8: Ullmann homocoupling reaction using a Pd@PANI-H catalyst.

efficiencies and faster rate of reaction. Chang et al. reported on palladium nanoparticles entrapped in aluminum oxyhydroxide for the hydrogenation of nitroaromatics and solid alkenes (Scheme 9) [75].

The same catalyst (Pd/AlO(OH) was also used by Fry and O'Connor with different concentrations for the hydrogenation of unsaturated esters [76]. The palladium nanoparticles entrapped in aluminum oxyhydroxide were found to be selective without reducing other functionalities in the molecule.

3.1.6. Palladium-Based Nanocatalysts for the Dichromate Reduction Reaction. In 2013, Tu et al. synthesized polyvinylpyrrolidone-stabilized palladium nanoparticles (PVP-Pd) through a chemical reduction protocol for Pd-catalyzed dichromate reduction [77]. Chromium exists in two oxidation states which are (Cr-VI) and (Cr-III) (Scheme 10). Among these two oxidation states, hexavalent chromium (Cr-VI) is a highly toxic and carcinogenic species. However, trivalent chromium (Cr-III) is comparatively nontoxic and even small quantities of (Cr-III) are required by the human body as an essential nutrient. Many reports appeared in the literature on the reduction of (Cr-VI) by using iron nanoparticles, aluminum oxide, titanium oxide, mixed transition metal nanoparticles, palladium nanoparticles, etc. [78]. Yang et al. demonstrated the application of tobacco mosaic virus-templated palladium nanoparticles for the reduction of (Cr-VI) and claimed that such a nanocatalyst system can be applied in different kinds of catalytic reactions [79].

3.1.7. Supported Palladium Nanoparticles. Palladium nanoparticles can lose their catalytic activity due to aggregation or precipitation. Therefore, stabilizers such as ligands, polymers, or surfactants are useful to control agglomeration and precipitation [80]. A variety of palladium nanoparticles that have appeared in the literature have described the advantages of supported systems such as carbon nanotubes [81], colloidal support [82], silica [83], metal nanoparticle support [84], polymers [85], carbon [86], and graphene [87]. Palladium nanoparticles supported onto different materials increase the surface-to-volume ratio of the composite and improve the catalytic activity and selectivity of the heterogeneous catalyst. Palladium nanoparticles either in colloidal form or deposited form have been successfully applied as a catalyst for different kinds of reactions. Liew et al. reported a new catalyst system of palladium nanoparticles (XL-HGPd) (Scheme 11) with the help of a cross-linking method [88]. Such a catalyst system was easy to recover and showed excellent recyclability with continuously high catalytic activities.

Liu et al. prepared palladium nanoparticles (1-5 nm) with the help of a helical backbone containing poly(*N*,*N*-dialkylcarbodiimide) (PDHC-Pd) as a polymeric gel for stabilizing a palladium nanocatalyst. Such a composite material was found to be very active for the Suzuki reaction under regular heating or microwave irradiation (Scheme 12) [89].

The catalyst was recycled for the second, third, fourth, and fifth time and reaction yields were 93%, 95%, 92%, and 90%, respectively. Palladium nanocatalysts with carbon nanomaterial support have been successfully applied for glucose oxidation reaction [90]. Glucose is considered as an emerging energy source for fuel cell technology improvement in order to fulfill the green energy requirement.

3.2. Platinum-Based Nanocatalysts. Platinum catalysts have been extensively used in pharmaceutical, chemical, electronic, petrochemical, and fuel cell applications [91]. Such catalysts have shown excellent catalytic and electrical activities as well as corrosion-resistant properties. Platinum-based catalysts have been successfully applied in sensors [92], fuel cells [93], methanol oxidation [94], and petroleum industries [95]. Platinum-based nanomaterials have shown remarkable properties because of their stability in different conditions. Just like other metal nanocatalysts, the activities of platinum-based nanocatalysts also depend on the size and shape of the catalyst. Several methods are available in the literature for the synthesis of platinum nanoparticles such as physical methods [96], solvothermal [97] and hydrothermal [98] approaches, sol-gel [99], and an electrodeposition [100] process. The morphology and properties of a platinum-based nanomaterial such as optical, magnetic, and catalytic properties can be tailored by changing the starting material and reaction parameters [101]. Narayanan and El-Sayed reported the Suzuki reaction between iodobenzene and phenylboronic acid to catalyze using platinum nanocatalysts (Scheme 13) [102].

3.3. Iron-Based Nanocatalysts. Iron, as a backbone of infrastructure, received great interest because of excellent magnetic and catalytic properties [103]. Due to their magnetic property, iron-based nanocatalysts can be easily separated by an external magnet after the completion of a reaction [104]. Iron oxide nanoparticles with various structures and morphologies have been widely used for drug delivery

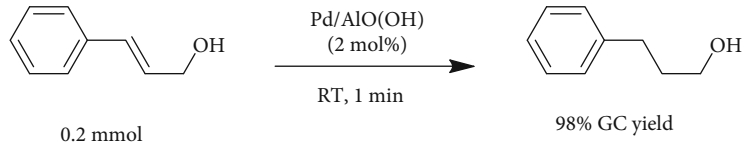

Scheme 9: Hydrogenation reaction in the presence of (Pd/AlO(OH)) nanocatalysts [75].

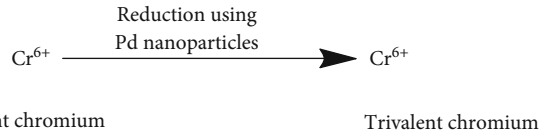

Scheme 10: Reduction of hexavalent chromium (Cr-VI) to trivalent chromium (Cr-III).

[105], biosensor [106], medical [107], and water treatment [108] applications, as well as other applications. Iron oxide nanoparticles have multiple advantages because of their low price and inherent biocompatibility. The synthetic scheme of iron nanoparticles plays a key role in terms of morphologies and chemical and physical properties [109]. Within the framework of different nanoparticles, ferromagnetic iron and cobalt nanoparticles and their oxides and alloys were found to be the most favorable probes for different applications [110].

2,4-Dichlorophenol is a toxic material and is present in both wastewater and soil. Li et al. successfully degraded 2,4-dichlorophenol by either Fenton oxidation or reductive dechlorination with the help of various iron-based nanoparticles [111]. In 2005, Park et al. reported a new synthetic way for the synthesis of monodisperse nanoparticles of iron oxide with a size of 6-13 nm [112]. The synthesis of 6-13 nm particle size was accomplished by the additional growth of the monodisperse nanoparticles of iron oxide. There are several methods available in the literature for the synthesis of iron nanoparticles; however, iron pentacarbonyl decomposition is the most widely used method because of ease of handling and because it only has carbon monoxide as a byproduct. Some other methods are also available in the literature such as the reduction of organic or inorganic salts [113], mechanical methods, and decomposition of other unstable iron compounds [114]. Jagadeesh et al. describe the synthesis of iron oxide-based nanocatalysts for the hydrogenation of nitroarenes to anilines with excellent activity and selectivity (Scheme 14) [115].

3.4. Copper-Based Nanocatalysts. Copper-based nanocatalysts have received considerable attention because of their high activity and low reaction temperature [116]. The activity of the Cu-based nanocatalyst can be influenced by synthetic protocol, composition, temperature, pressure, concentration, and reactor type [117]. Various methods are available in the literature to synthesize Cu-based nanocatalysts such as hydrothermal [118], coprecipitation [119], homogenous precipitation [120], and impregnation [121]. Recently Lamei et al. reported a green nontoxic catalyst material to comprise nanowires and nanoparticles embedded in a carbonaceous matrix [53]. Such a Cu-based ligand-free nanocatalyst system was applied to the Suzuki coupling reaction with excellent activity and no significant loss of activity observed even after four cycles (Scheme 15).

3.5. Gold-Based Nanocatalysts. Since the pioneering studies of Haruta et al. [122], gold nanocatalysts have become widely used nanoparticles for oxidation [123], reduction [124], hydrogenation [125], homocoupling [126], degradation of organic pollutants [127], and electrochemical sensor applications [128]. In order to expose more atoms on the surface, gold nanoparticles are usually dispersed on a suitable support such as activated carbon [129], starch [130], silica [131], metal oxide [132], and resin [133]. Gold along with magnetic nanoparticles such as catalytic support has gained much attention due to its superparamagnetic properties and environmentally friendly nature. The gold-magnetic nanocatalyst (Au-Fe_3O_4) has shown excellent catalytic activity in various organic reactions such as oxidation of CO [134] and reduction of H_2O_2 [135]. Lin and Doong synthesized Au-Fe_3O_4 nanocatalysts through iron-oleate decomposition in the presence of Au seeds. The catalyst system was successfully applied in the reduction of nitrophenol with excellent activity and selectivity (Scheme 16) [136].

3.6. Silver-Based Nanocatalysts. Silver nanoparticles have been successfully applied in optics, medicine, catalysis, and sensors [137]. Silver-based nanocatalysts are continuously being developed due to their strong absorption in the region of visible light which is easily detectable through a UV-visible spectrophotometer. In terms of organic reactions, silver nanocatalysts are used in reduction reactions [138], alkylation [139], degradation [140], reduction [141], and synthesis of fine chemicals [142]. Recently, Mandi et al. reported the synthesis of supported silver nanocatalysts via acrylic acid polymerization and subsequent immobilization with silver nanoparticles to form nanocomposite Ag-MCP-1. The nanocomposite material was used in a reductive coupling reaction of nitrobenzene with alcohols in the presence of a hydrogen source such as glycerol (Scheme 17) [143].

Apart from colloidal Ag nanoparticles, 1D and 2D structures of Ag and their composites have also shown huge prospects in catalytic conversion. Ag nanowires and copper oxide-embedded Ag nanowires showed excellent and rapid catalytic activity [144]. The activity and selectivity of such composites were reported to be ecofriendly and distinguished. However, Ag nanowires possessed 40% conversion efficiency along with 95% selectivity, and copper oxide-embedded Ag nanowires showed much higher activity and stability compared to individual metal oxides or metal nanowires [145]. Such demonstration paves way for further

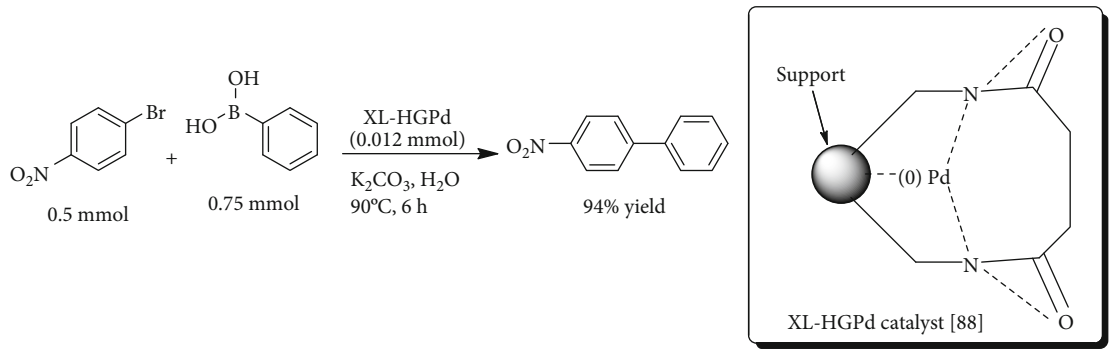

Scheme 11: Suzuki reaction catalyzed by an XL-HGPd nanocatalyst [88].

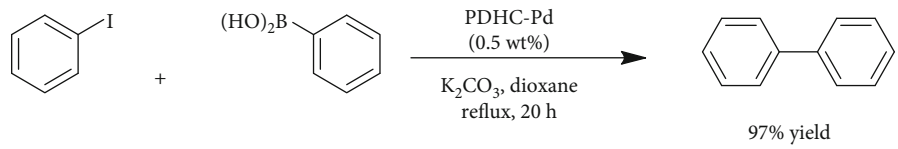

Scheme 12: Suzuki reaction in the presence of PDHC-Pd nanocatalysts [89].

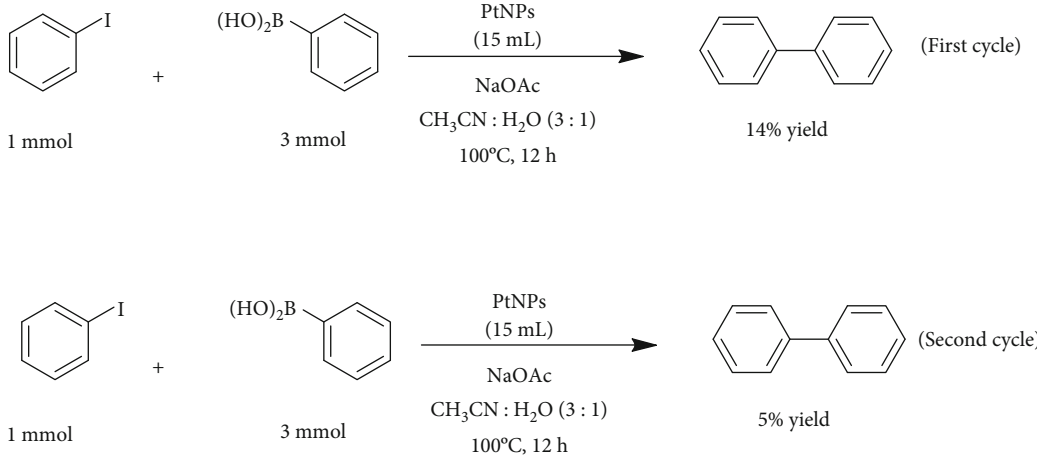

Scheme 13: Suzuki reaction between iodobenzene and phenylboronic acid catalyze using platinum nanocatalysts [102].

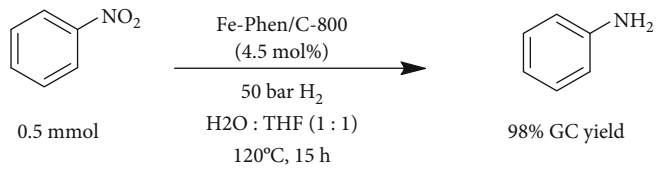

Scheme 14: Hydrogenation of nitrobenzene to aniline using iron nanocatalysts [115].

efficient designs and innovative applications of metal oxide-embedded 1D and 2D materials as new nanocatalysts for organic conversion.

3.7. Zinc-Based Nanocatalysts. The nanocomposite system containing zinc oxide mixed with other metal oxides has been a material of choice due to several applications such as the production of biodiesel [146], CO_2 conversion [147], aldehyde oxidation [148], hydrogen production [118], trans-esterification [149], wastewater treatment [150], azo dye decoloration [151], and chemoselective acetylation [152]. The activity and selectivity of the zinc oxide-based

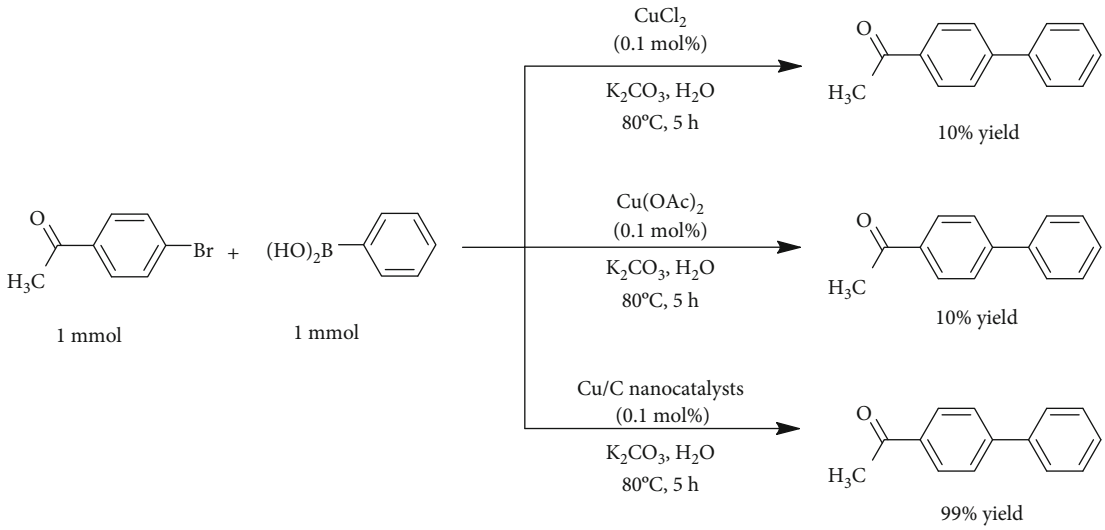

Scheme 15: Suzuki coupling reaction using different copper catalysts [53].

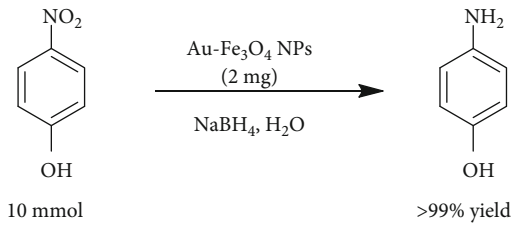

Scheme 16: Reduction of nitrophenol using gold-magnetic nanocatalysts (Au-Fe_3O_4) [136].

nanocatalysts rely on size and morphology of the synthesized material. Different methods are available in the literature to describe the synthetic procedures for controlling the size and morphology of the zinc oxide nanocatalysts such as coprecipitation [119], microwave assisted [153], combustion [154], ion exchange, and vapor phase transport [155]. In 2015, Saikia et al. reported the synthesis of zinc oxide nanocatalysts through the leaf extract of *Carica papaya* and its application in the synthesis of oxime derivatives [156]. The reaction was run without a solvent under microwave irradiation to form an oxime with an excellent yield and with a recycle capability up to 5th run (Scheme 18).

4. Future Prospects and Challenges

Carbon-carbon cross-coupling protocols such as Suzuki, Heck, and Sonogashira reactions are industrially important reactions, and a review of the literature reveals that these reactions are catalyzed by precious metals including palladium or gold nanoparticles. Therefore, it is highly anticipated that the focus of research will be on the development of either metal-free or nonnoble metal nanocatalysts with high activity and selectivity for carbon-carbon cross-coupling reactions. Nanocatalysts are known to have high activity and selectivity, but they suffer from instability and reusability issues. One way to achieve high stability and reusability is for the nanocatalyst to have a strong interaction with the support system which can prevent an aggregation problem. To achieve this, the support system should have chelating properties to bind the nanoparticles more strongly. Severe conditions such as high-temperature reactions can cause the leaching of metal in the nanocatalysts. Initially, it was thought that the leaching process mainly occurs with nanocatalysts containing the palladium metal. However, in recent times, a number of reports appeared in the literature describing the leaching of other noble metals in nanocatalysts. Therefore, the development of new nanocatalysts that can bear harsh conditions is highly desirable. As depicted earlier, the shape and size of the nanocatalyst have a great impact on their catalytic properties and stabilities. Hence, new methods with a well-controlled size and shape of the nanocatalysts need to be developed. The multistep synthesis using a costly starting material and low yield hinders their commercial applications. Such synthetic protocols need to be replaced with a facile route, a green process, and large-scale production with high quality.

5. Conclusion

In this review, we highlighted the recent progress on the design and development of nanocatalysts and discussed their catalytic application in important organic reactions. The synthetic procedure of nanocatalysts contains various metals such as Pd, Pt, Fe, Cu, Au, Ag, and Zn and have been reviewed along with their important applications. Among the various metals, the palladium-based nanocatalysts are the most widely investigated material for coupling reactions. Palladium nanocatalysts either with a suitable support or as mixed metal oxides are known to increase the surface-to-volume ratio of the composite and improve the catalytic activity and selectivity of the heterogeneous catalyst. The industrially important organic reactions such as carbon-carbon bond coupling reactions, carbon-heteroatom bond coupling reactions, carbon-carbon homocoupling reactions, hydrogenation, reduction, and oxime formation reactions have been reviewed. Similarly, the Suzuki reaction has been a benchmark to explore the catalytic activities of newly

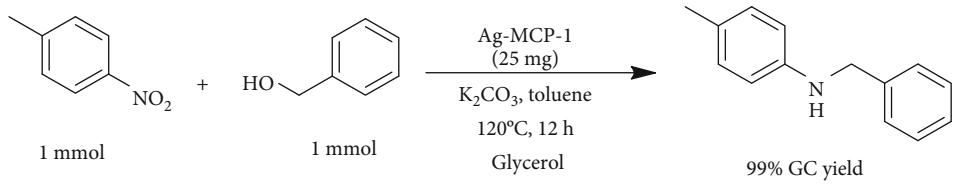

Scheme 17: Reductive amination reaction between 4-methylnitrobenzene and benzyl alcohol using a Ag-MCP-1 nanocatalyst [143].

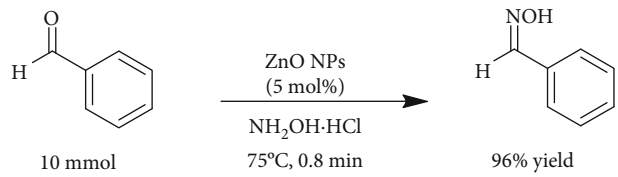

Scheme 18: Conversion of aldehyde/ketone into oximes using zinc oxide nanocatalysts [156].

synthesized palladium-based nanocatalysts. The future prospects that need to be addressed, on the basis of literature review, have also been highlighted at the end. Consequently, this review article may help on the design and development of new nanocomposite catalysts containing a well-defined shape and size with high activity, selectivity, stability, and reusability. This literature search will also help to identify the best support system for high-performance supported nanocatalysts. Due to the ease of synthesis, high activity, and selectivity, more nanocatalyst systems will be developed in the near future for organic conversion.

Conflicts of Interest

The authors declare that there is no conflict of interest regarding the publication of this paper.

Acknowledgments

The authors are thankful to the Center for Integrative Petroleum Research (CIPR) for the research start-up project SF-17003, the Center of Research Excellence in Renewable Energy (CoRERE), and the Deanship of Scientific Research (DSR) at King Fahd University of Petroleum & Minerals (KFUPM) through project No. IN151003.

References

[1] L. A. Kolahalam, I. K. Viswanath, B. S. Diwakar, B. Govindh, V. Reddy, and Y. L. Murthy, "Review on nanomaterials: synthesis and applications," *Materials Today: Proceedings*, 2019.

[2] B. R. Cuenya and F. Behafarid, "Nanocatalysis: size- and shape-dependent chemisorption and catalytic reactivity," *Surface Science Reports*, vol. 70, no. 2, pp. 135–187, 2015.

[3] M. S. Kamal, A. A. Adewunmi, A. S. Sultan, M. F. Al-Hamad, and U. Mehmood, "Recent advances in nanoparticles enhanced oil recovery: rheology, interfacial tension, oil recovery, and wettability alteration," *Journal of Nanomaterials*, vol. 2017, Article ID 2473175, 15 pages, 2017.

[4] L. Li, H. Yang, D. Zhou, and Y. Zhou, "Progress in application of CNTs in lithium-ion batteries," *Journal of Nanomaterials*, vol. 2014, Article ID 187891, 8 pages, 2014.

[5] R. Liu, Q. Zhao, Y. Li, G. Zhang, F. Zhang, and X. Fan, "Graphene supported Pt/Ni nanoparticles as magnetically separable nanocatalysts," *Journal of Nanomaterials*, vol. 2013, Article ID 602602, 7 pages, 2013.

[6] Y. Xu, Y. Liang, L. Jiang, H. Wu, H. Zhao, and D. Xue, "Preparation and magnetic properties of $ZnFe_2O_4$ nanotubes," *Journal of Nanomaterials*, vol. 2011, Article ID 525967, 5 pages, 2011.

[7] L. Song, Y. Han, F. Guo et al., "Mesoporous nickel-based zeolite capsule complex with Fe_3O_4 as electrode for advanced supercapacitor," *Journal of Nanomaterials*, vol. 2018, Article ID 9813203, 13 pages, 2018.

[8] V. V. Pokropivny and V. V. Skorokhod, "New dimensionality classifications of nanostructures," *Physica E: Low-dimensional Systems and Nanostructures*, vol. 40, no. 7, pp. 2521–2525, 2008.

[9] E. González, J. E. Villegas, D. Jaque, E. Navarro, and J. L. Vicent, "Fabrication of 2D, 1D and 0D ordered metallic nanostructures," *Vacuum*, vol. 67, no. 3, pp. 693–698, 2002.

[10] D. Astruc, F. Lu, and J. R. Aranzaes, "Nanoparticles as recyclable catalysts: the frontier between homogeneous and heterogeneous catalysis," *Angewandte Chemie International Edition*, vol. 44, no. 48, pp. 7852–7872, 2005.

[11] A. Makawana, C. B. Sangani, Y.-F. Yao, Y.-T. Duan, P.-C. Lv, and H.-L. Zhu, "Recent developments of metal and metal oxide nanocatalysts in organic synthesis," *Mini Reviews in Medicinal Chemistry*, vol. 16, no. 16, pp. 1303–1320, 2016.

[12] J. Choi and G. C. Fu, "Transition metal-catalyzed alkyl-alkyl bond formation: another dimension in cross-coupling chemistry," *Science*, vol. 356, no. 6334, article eaaf7230, 2017.

[13] N. V. Tzouras, I. K. Stamatopoulos, A. T. Papastavrou, A. A. Liori, and G. C. Vougioukalakis, "Sustainable metal catalysis in CH activation," *Coordination Chemistry Reviews*, vol. 343, pp. 25–138, 2017.

[14] M. M. Lorion, K. Maindan, A. R. Kapdi, and L. Ackermann, "Heteromultimetallic catalysis for sustainable organic syntheses," *Chemical Society Reviews*, vol. 46, no. 23, pp. 7399–7420, 2017.

[15] N. Sharma, H. Ojha, A. Bharadwaj, D. P. Pathak, and R. K. Sharma, "Preparation and catalytic applications of nanomaterials: a review," *RSC Advances*, vol. 5, no. 66, pp. 53381–53403, 2015.

[16] T. P. N. Tran, A. Thakur, D. X. Trinh, A. T. N. Dao, and T. Taniike, "Design of Pd@graphene oxide framework nanocatalyst with improved activity and recyclability in Suzuki-Miyaura cross-coupling reaction," *Applied Catalysis A: General*, vol. 549, pp. 60–67, 2017.

[17] Y.-Y. Yu, Q.-W. Cheng, C. Sha, Y.-X. Chen, S. Naraginti, and Y.-C. Yong, "Size-controlled biosynthesis of FeS nanoparticles for efficient removal of aqueous Cr(VI)," *Chemical Engineering Journal*, vol. 379, article 122404, 2019.

[18] S. J. Yoo, T.-Y. Jeon, K.-S. Lee, K.-W. Park, and Y.-E. Sung, "Effects of particle size on surface electronic and electrocatalytic properties of Pt/TiO_2 nanocatalysts," *Chemical Communications*, vol. 46, no. 5, pp. 794–796, 2010.

[19] G. C. Bond and D. T. Thompson, "Catalysis by gold," *Catalysis Reviews*, vol. 41, no. 3-4, pp. 319–388, 1999.

[20] Y. Li, X. Fan, J. Qi et al., "Palladium nanoparticle-graphene hybrids as active catalysts for the Suzuki reaction," *Nano Research*, vol. 3, no. 6, pp. 429–437, 2010.

[21] E. Dube and T. Nyokong, "Effect of gold nanoparticle shape on the photophysicochemical properties of sulphur containing metallophthalocyanines," *Journal of Molecular Structure*, vol. 1181, pp. 312–320, 2019.

[22] M. Haruta, "Nanoparticulate gold catalysts for low-temperature CO oxidation," *ChemInform*, vol. 35, no. 48, 2004.

[23] C. R. Henry, "Morphology of supported nanoparticles," *Progress in Surface Science*, vol. 80, no. 3, pp. 92–116, 2005.

[24] R. Narayanan and M. A. El-Sayed, "Effect of nanocatalysis in colloidal solution on the tetrahedral and cubic nanoparticle shape: electron-transfer reaction catalyzed by platinum nanoparticles," *The Journal of Physical Chemistry B*, vol. 108, no. 18, pp. 5726–5733, 2004.

[25] I. Khan and A. Qurashi, "Shape controlled synthesis of copper vanadate platelet nanostructures, their optical band edges, and solar-driven water splitting properties," *Scientific Reports*, vol. 7, no. 1, article 14370, 2017.

[26] L. Luo, H. Li, Y. Peng, and C. Feng, "Recent advances in Rh-based nanocatalysts for heterogeneous reactions," *ChemNanoMat*, vol. 4, 2018.

[27] F. Dufour, B. Fresch, O. Durupthy, C. Chaneac, and F. Remacle, "Ligand and solvation effects on the structural and electronic properties of small gold clusters," *The Journal of Physical Chemistry C*, vol. 118, no. 8, pp. 4362–4376, 2014.

[28] Y.-F. Li and Z.-P. Liu, "Particle size, shape and activity for photocatalysis on titania anatase nanoparticles in aqueous surroundings," *Journal of the American Chemical Society*, vol. 133, no. 39, pp. 15743–15752, 2011.

[29] M. Hou, Q. Mei, and B. Han, "Solvent effects on geometrical structures and electronic properties of metal Au, Ag, and Cu nanoparticles of different sizes," *Journal of Colloid and Interface Science*, vol. 449, pp. 488–493, 2015.

[30] S. R. Chowdhury, P. S. Roy, and S. K. Bhattacharya, "Room temperature synthesis of polyvinyl alcohol stabilized palladium nanoparticles: solvent effect on shape and electrocatalytic activity," *Nano-Structures & Nano-Objects*, vol. 14, pp. 11–18, 2018.

[31] Y. Zhu and N. S. Hosmane, "Nanocatalysis: recent advances and applications in boron chemistry," *Coordination Chemistry Reviews*, vol. 293–294, pp. 357–367, 2015.

[32] A. Y. Khormi, T. A. Farghaly, and M. R. Shaaban, "Pyrimidyl formamidine palladium(II) complex as a nanocatalyst for aqueous Suzuki-Miyaura coupling," *Heliyon*, vol. 5, no. 3, article e01367, 2019.

[33] E. Rafiee, M. Joshaghani, and P. G.-S. Abadi, "Effect of a weak magnetic field on the Mizoroki-Heck coupling reaction in the presence of wicker-like palladium-poly(N-vinylpyrrolidone)-iron nanocatalyst," *Journal of Magnetism and Magnetic Materials*, vol. 408, pp. 107–115, 2016.

[34] S. Rohani, G. M. Ziarani, A. Ziarati, and A. Badiei, "Designer 3D CoAl-layered double hydroxide@N, S doped graphene hollow architecture decorated with Pd nanoparticles for Sonogashira couplings," *Applied Surface Science*, vol. 496, article 143599, 2019.

[35] A. Balanta, C. Godard, and C. Claver, "Pd nanoparticles for C-C coupling reactions," *Chemical Society Reviews*, vol. 40, no. 10, pp. 4973–4985, 2011.

[36] T. Tamoradi, A. Ghorbani-Choghamarani, and M. Ghadermazi, "Synthesis of a new Pd(0)-complex supported on magnetic nanoparticles and study of its catalytic activity for Suzuki and Stille reactions and synthesis of 2,3-dihydroquinazolin-4(1H)-one derivatives," *Polyhedron*, vol. 145, pp. 120–130, 2018.

[37] D. Astruc, "Palladium nanoparticles as efficient green homogeneous and heterogeneous carbon-carbon coupling precatalysts: a unifying view," *Inorganic Chemistry*, vol. 46, no. 6, pp. 1884–1894, 2007.

[38] A. R. Hajipour and P. Abolfathi, "Nickel embedded on triazole-modified magnetic nanoparticles: a novel and sustainable heterogeneous catalyst for Hiyama reaction in fluoride-free condition," *Catalysis Communications*, vol. 103, pp. 92–95, 2018.

[39] A. Trzeciak and A. Augustyniak, "The role of palladium nanoparticles in catalytic C-C cross-coupling reactions," *Coordination Chemistry Reviews*, vol. 384, pp. 1–20, 2019.

[40] M. J. Mphahlele and M. M. Maluleka, "Advances in metal-catalyzed cross-coupling reactions of halogenated quinazolinones and their quinazoline derivatives," *Molecules*, vol. 19, no. 11, pp. 17435–17463, 2014.

[41] D. Ganapathy and G. Sekar, "Palladium nanoparticles stabilized by metal-carbon covalent bond: an efficient and reusable nanocatalyst in cross-coupling reactions," *Catalysis Communications*, vol. 39, pp. 50–54, 2013.

[42] A. Ghorbani-Choghamarani, B. Tahmasbi, N. Noori, and S. Faryadi, "Pd-S-methylisothiourea supported on magnetic nanoparticles as an efficient and reusable nanocatalyst for Heck and Suzuki reactions," *Comptes Rendus Chimie*, vol. 20, no. 2, pp. 132–139, 2017.

[43] A. Naghipour and A. Fakhri, "Heterogeneous Fe_3O_4@chitosan-Schiff base Pd nanocatalyst: fabrication, characterization and application as highly efficient and magnetically-recoverable catalyst for Suzuki-Miyaura and Heck-Mizoroki C-C coupling reactions," *Catalysis Communications*, vol. 73, pp. 39–45, 2016.

[44] P. Veerakumar, M. Velayudham, K.-L. Lu, and S. Rajagopal, "Silica-supported PEI capped nanopalladium as potential catalyst in Suzuki, Heck and Sonogashira coupling reactions," *Applied Catalysis A: General*, vol. 455, pp. 247–260, 2013.

[45] M. Panchal, A. Kongor, V. Mehta, M. Vora, K. Bhatt, and V. Jain, "Heck-type olefination and Suzuki coupling reactions using highly efficient oxacalix[4]arene wrapped nanopalladium catalyst," *Journal of Saudi Chemical Society*, vol. 22, no. 5, pp. 558–568, 2017.

[46] M. Nasrollahzadeh and A. Banaei, "Hybrid Au/Pd nanoparticles as reusable catalysts for Heck coupling reactions in water under aerobic conditions," *Tetrahedron Letters*, vol. 56, no. 3, pp. 500–503, 2015.

[47] F. Heidari, M. Hekmati, and H. Veisi, "Magnetically separable and recyclable Fe_3O_4@SiO_2/isoniazide/Pd nanocatalyst for highly efficient synthesis of biaryls by Suzuki coupling reactions," *Journal of Colloid and Interface Science*, vol. 501, pp. 175–184, 2017.

[48] S. K. Movahed, M. Dabiri, and A. Bazgir, "Palladium nanoparticle decorated high nitrogen-doped graphene with high catalytic activity for Suzuki-Miyaura and Ullmann-type coupling reactions in aqueous media," *Applied Catalysis A: General*, vol. 488, Supplement C, pp. 265–274, 2014.

[49] A. Shaabani and M. Mahyari, "PdCo bimetallic nanoparticles supported on PPI-grafted graphene as an efficient catalyst for Sonogashira reactions," *Journal of Materials Chemistry A*, vol. 1, no. 32, pp. 9303–9311, 2013.

[50] Y.-T. Chu, K. Chanda, P.-H. Lin, and M. H. Huang, "Aqueous phase synthesis of palladium tripod nanostructures for Sonogashira coupling reactions," *Langmuir*, vol. 28, no. 30, pp. 11258–11264, 2012.

[51] M. Radtke, S. Stumpf, B. Schröter, S. Höppener, U. S. Schubert, and A. Ignaszak, "Electrodeposited palladium on MWCNTs as "semi-soluble heterogeneous" catalyst for cross-coupling reactions," *Tetrahedron Letters*, vol. 56, no. 27, pp. 4084–4087, 2015.

[52] S.-J. Kim, S.-D. Oh, S. Lee, and S.-H. Choi, "Radiolytic synthesis of Pd-M (M = Ag, Ni, and Cu)/C catalyst and their use in Suzuki-type and Heck-type reaction," *Journal of Industrial and Engineering Chemistry*, vol. 14, no. 4, pp. 449–456, 2008.

[53] K. Lamei, H. Eshghi, M. Bakavoli, S. A. Rounaghi, and E. Esmaeili, "Carbon coated copper nanostructures as a green and ligand free nanocatalyst for Suzuki cross-coupling reaction," *Catalysis Communications*, vol. 92, pp. 40–45, 2017.

[54] H. Veisi and A. Kakanejadifard, "Immobilization of palladium nanoparticles on ionic liquid-triethylammonium chloride functionalized magnetic nanoparticles: as a magnetically separable, stable and recyclable catalyst for Suzuki-Miyaura cross-coupling reactions," *Tetrahedron Letters*, vol. 58, no. 45, pp. 4269–4276, 2017.

[55] Y. Li, X. Fan, J. Qi et al., "Gold nanoparticles-graphene hybrids as active catalysts for Suzuki reaction," *Materials Research Bulletin*, vol. 45, no. 10, pp. 1413–1418, 2010.

[56] M. Nasrollahzadeh and S. M. Sajadi, "Green synthesis, characterization and catalytic activity of the Pd/TiO_2 nanoparticles for the ligand-free Suzuki-Miyaura coupling reaction," *Journal of Colloid and Interface Science*, vol. 465, pp. 121–127, 2016.

[57] Y. Na, S. Park, S. B. Han, H. Han, S. Ko, and S. Chang, "Ruthenium-catalyzed Heck-type olefination and Suzuki coupling reactions: studies on the nature of catalytic species," *Journal of the American Chemical Society*, vol. 126, no. 1, pp. 250–258, 2004.

[58] P. M. Uberman, L. A. Pérez, G. I. Lacconi, and S. E. Martín, "PVP-stabilized palladium nanoparticles electrochemically obtained as effective catalysts in aqueous medium Suzuki-Miyaura reaction," *Journal of Molecular Catalysis A: Chemical*, vol. 363, pp. 245–253, 2012.

[59] N. Ghanbari, S. J. Hoseini, and M. Bahrami, "Ultrasonic assisted synthesis of palladium-nickel/iron oxide core-shell nanoalloys as effective catalyst for Suzuki-Miyaura and p-nitrophenol reduction reactions," *Ultrasonics Sonochemistry*, vol. 39, pp. 467–477, 2017.

[60] S. J. Hoseini, M. Dehghani, and H. Nasrabadi, "Thin film formation of Pd/reduced-graphene oxide and Pd nanoparticles at oil-water interface, suitable as effective catalyst for Suzuki-Miyaura reaction in water," *Catalysis Science & Technology*, vol. 4, no. 4, pp. 1078–1083, 2014.

[61] L. Shiyong, Q. Zhou, Z. Jin, H. Jiang, and X. Jiang, "Dodecylsulfate anion embedded layered double hydroxide supported nanopalladium catalyst for the Suzuki reaction," *Chinese Journal of Catalysis*, vol. 31, no. 5, pp. 557–561, 2010.

[62] P. Mondal, P. Bhanja, R. Khatun, A. Bhaumik, D. Das, and S. M. Islam, "Palladium nanoparticles embedded on mesoporous TiO_2 material (Pd@MTiO_2) as an efficient heterogeneous catalyst for Suzuki-coupling reactions in water medium," *Journal of Colloid and Interface Science*, vol. 508, pp. 378–386, 2017.

[63] M. Shokouhimehr, T. Kim, S. W. Jun et al., "Magnetically separable carbon nanocomposite catalysts for efficient nitroarene reduction and Suzuki reactions," *Applied Catalysis A: General*, vol. 476, pp. 133–139, 2014.

[64] J. Xia, Y. Fu, G. He, X. Sun, and X. Wang, "Core-shell-like Ni-Pd nanoparticles supported on carbon black as a magnetically separable catalyst for green Suzuki-Miyaura coupling reactions," *Applied Catalysis B: Environmental*, vol. 200, pp. 39–46, 2017.

[65] P. Mondal, N. Salam, A. Mondal, K. Ghosh, K. Tuhina, and S. M. Islam, "A highly active recyclable gold-graphene nanocomposite material for oxidative esterification and Suzuki cross-coupling reactions in green pathway," *Journal of Colloid and Interface Science*, vol. 459, pp. 97–106, 2015.

[66] M. Thomas, M. U. D. Sheikh, D. Ahirwar, M. Bano, and F. Khan, "Gold nanoparticle and graphene oxide incorporated strontium crosslinked alginate/carboxymethyl cellulose composites for o-nitroaniline reduction and Suzuki-Miyaura cross-coupling reactions," *Journal of Colloid and Interface Science*, vol. 505, pp. 115–129, 2017.

[67] Y. Kiso, K. Yamamoto, K. Tamao, and M. Kumada, "Asymmetric homogeneous hydrosilylation with chiral phosphine-palladium complexes," *Journal of the American Chemical Society*, vol. 94, no. 12, pp. 4373-4374, 1972.

[68] J. K. Stille and K. S. Y. Lau, "Mechanisms of oxidative addition of organic halides to group 8 transition-metal complexes," *Accounts of Chemical Research*, vol. 10, no. 12, pp. 434–442, 1977.

[69] F. Panahi, F. Daneshgar, F. Haghighi, and A. Khalafi-Nezhad, "Immobilized Pd nanoparticles on silica-starch substrate (PNP-SSS): efficient heterogeneous catalyst in Buchwald-Hartwig C-N cross coupling reaction," *Journal of Organometallic Chemistry*, vol. 851, pp. 210–217, 2017.

[70] A. R. Hajipour, Z. Khorsandi, and S. F. M. Metkazini, "Palladium nanoparticles supported on cysteine-functionalized MNPs as robust recyclable catalysts for fast O-and N-arylation reactions in green media," *Journal of Organometallic Chemistry*, vol. 899, article 120793, 2019.

[71] H. Veisi, P. Safarimehr, and S. Hemmati, "Buchwald-Hartwig C-N cross coupling reactions catalyzed by palladium nanoparticles immobilized on thio modified-multi walled carbon nanotubes as heterogeneous and recyclable nanocatalyst," *Materials Science and Engineering: C*, vol. 96, pp. 310–318, 2019.

[72] S. Santra, P. Ranjan, S. K. Mandal, and P. K. Ghorai, "Living nanocatalyst for effective synthesis of symmetrical biaryls," *Inorganica Chimica Acta*, vol. 372, no. 1, pp. 47–52, 2011.

[73] F. Rafiee, P. Khavari, Z. Payami, and N. Ansari, "Palladium nanoparticles immobilized on the magnetic few layer graphene support as a highly efficient catalyst for ligand free Suzuki cross coupling and homo coupling reactions," *Journal of Organometallic Chemistry*, vol. 883, pp. 78–85, 2019.

[74] Y. Liu, D. Tang, K. Cao, L. Yu, J. Han, and Q. Xu, "Probing the support effect at the molecular level in the polyaniline-supported palladium nanoparticle-catalyzed Ullmann reaction of aryl iodides," *Journal of Catalysis*, vol. 360, pp. 250–260, 2018.

[75] F. Chang, H. Kim, B. Lee, S. Park, and J. Park, "Highly efficient solvent-free catalytic hydrogenation of solid alkenes and nitro-aromatics using Pd nanoparticles entrapped in aluminum oxy-hydroxide," *Tetrahedron Letters*, vol. 51, no. 32, pp. 4250–4252, 2010.

[76] D. Fry and K. O'Connor, "The solvent-less hydrogenation of unsaturated esters using 0.5% Pd/Al (O) OH as a catalyst," *The Chemical Educator*, vol. 18, pp. 144–146, 2013.

[77] W. Tu, K. Li, X. Shu, and W. W. Yu, "Reduction of hexavalent chromium with colloidal and supported palladium nanocatalysts," *Journal of Nanoparticle Research*, vol. 15, no. 4, pp. 1–9, 2013.

[78] C. Yang, J. H. Meldon, B. Lee, and H. Yi, "Investigation on the catalytic reduction kinetics of hexavalent chromium by viral-templated palladium nanocatalysts," *Catalysis Today*, vol. 233, pp. 108–116, 2014.

[79] C. Yang, A. K. Manocchi, B. Lee, and H. Yi, "Viral templated palladium nanocatalysts for dichromate reduction," *Applied Catalysis B: Environmental*, vol. 93, no. 3, pp. 282–291, 2010.

[80] S. Karaboga and S. Özkar, "Nanoalumina supported palladium(0) nanoparticle catalyst for releasing H_2 from dimethylamine borane," *Applied Surface Science*, vol. 487, pp. 433–441, 2019.

[81] J. V. Rojas and C. H. Castano, "Production of palladium nanoparticles supported on multiwalled carbon nanotubes by gamma irradiation," *Radiation Physics and Chemistry*, vol. 81, no. 1, pp. 16–21, 2012.

[82] I. Miguel-García, Á. Berenguer-Murcia, T. García, and D. Cazorla-Amorós, "Effect of the aging time of PVP coated palladium nanoparticles colloidal suspensions on their catalytic activity in the preferential oxidation of CO," *Catalysis Today*, vol. 187, no. 1, pp. 2–9, 2012.

[83] X. Le, Z. Dong, X. Li, W. Zhang, M. Le, and J. Ma, "Fibrous nano-silica supported palladium nanoparticles: an efficient catalyst for the reduction of 4-nitrophenol and hydrodechlorination of 4-chlorophenol under mild conditions," *Catalysis Communications*, vol. 59, pp. 21–25, 2015.

[84] M. Gholinejad and A. Aminianfar, "Palladium nanoparticles supported on magnetic copper ferrite nanoparticles: the synergistic effect of palladium and copper for cyanation of aryl halides with $K_4[Fe(CN)_6]$," *Journal of Molecular Catalysis A: Chemical*, vol. 397, pp. 106–113, 2015.

[85] M. M. Dell'Anna, V. F. Capodiferro, M. Mali et al., "Highly selective hydrogenation of quinolines promoted by recyclable polymer supported palladium nanoparticles under mild conditions in aqueous medium," *Applied Catalysis A: General*, vol. 481, no. 0, pp. 89–95, 2014.

[86] C. Shang, W. Hong, J. Wang, and E. Wang, "Carbon supported trimetallic nickel-palladium-gold hollow nanoparticles with superior catalytic activity for methanol electrooxidation," *Journal of Power Sources*, vol. 285, pp. 12–15, 2015.

[87] M. Gómez-Martínez, E. Buxaderas, I. M. Pastor, and D. A. Alonso, "Palladium nanoparticles supported on graphene and reduced graphene oxide as efficient recyclable catalyst for the Suzuki-Miyaura reaction of potassium aryltrifluoroborates," *Journal of Molecular Catalysis A: Chemical*, vol. 404–405, pp. 1–7, 2015.

[88] K. H. Liew, W. Z. Samad, N. Nordin et al., "Preparation and characterization of HypoGel-supported Pd nanocatalysts for Suzuki reaction under mild conditions," *Chinese Journal of Catalysis*, vol. 36, no. 5, pp. 771–777, 2015.

[89] Y. Liu, C. Khemtong, and J. Hu, "Synthesis and catalytic activity of a poly(*N*,*N*-dialkylcarbodiimide)/palladium nanoparticle composite: a case in the Suzuki coupling reaction using microwave and conventional heating," *Chemical Communications*, no. 4, pp. 398-399, 2004.

[90] C.-C. Chen, C.-L. Lin, and L.-C. Chen, "Functionalized carbon nanomaterial supported palladium nano-catalysts for electrocatalytic glucose oxidation reaction," *Electrochimica Acta*, vol. 152, pp. 408–416, 2015.

[91] R. Serra-Maia, S. Chastka, M. Bellier, T. Douglas, J. D. Rimstidt, and F. M. Michel, "Effect of particle size on catalytic decomposition of hydrogen peroxide by platinum nanocatalysts," *Journal of Catalysis*, vol. 373, pp. 58–66, 2019.

[92] W. Liu, K. Hiekel, R. Hübner, H. Sun, A. Ferancova, and M. Sillanpää, "Pt and Au bimetallic and monometallic nanostructured amperometric sensors for direct detection of hydrogen peroxide: influences of bimetallic effect and silica support," *Sensors and Actuators B: Chemical*, vol. 255, pp. 1325–1334, 2017.

[93] J. Lin, V. Kamavaram, and A. Kannan, "Synthesis and characterization of carbon nanotubes supported platinum nanocatalyst for proton exchange membrane fuel cells," *Journal of Power Sources*, vol. 195, no. 2, pp. 466–470, 2010.

[94] C. Berghian-Grosan, T. Radu, A. R. Biris et al., "Platinum nanoparticles coated by graphene layers: a low-metal loading catalyst for methanol oxidation in alkaline media," *Journal of Energy Chemistry*, vol. 40, pp. 81–88, 2020.

[95] H. Gobara, R. S. Mohamed, F. H. Khalil, M. S. El-Shall, and S. A. Hassan, "Various characteristics of Ni and Pt-Al_2O_3 nanocatalysts prepared by microwave method to be applied in some petrochemical processes," *Egyptian Journal of Petroleum*, vol. 23, no. 1, pp. 105–118, 2014.

[96] E. Gharibshahi, E. Saion, A. Ashraf, and L. Gharibshahi, "Size-controlled and optical properties of platinum nanoparticles by gamma radiolytic synthesis," *Applied Radiation and Isotopes*, vol. 130, pp. 211–217, 2017.

[97] J. Lai, W. Niu, R. Luque, and G. Xu, "Solvothermal synthesis of metal nanocrystals and their applications," *Nano Today*, vol. 10, no. 2, pp. 240–267, 2015.

[98] Y. Yang, L.-M. Luo, J.-J. Du et al., "Facile one-pot hydrothermal synthesis and electrochemical properties of carbon nanospheres supported Pt nanocatalysts," *International Journal of Hydrogen Energy*, vol. 41, no. 28, pp. 12062–12068, 2016.

[99] A. Chen and P. Holt-Hindle, "Platinum-based nanostructured materials: synthesis, properties, and applications," *Chemical Reviews*, vol. 110, no. 6, pp. 3767–3804, 2010.

[100] F. Ye, W. Hu, T. Zhang, J. Yang, and Y. Ding, "Enhanced electrocatalytic activity of Pt-nanostructures prepared by electrodeposition using poly(vinyl pyrrolidone) as a shape-control agent," *Electrochimica Acta*, vol. 83, pp. 383–386, 2012.

[101] K. A. Manbeck, N. E. Musselwhite, L. M. Carl et al., "Factors affecting activity and selectivity during cyclohexanone hydrogenation with colloidal platinum nanocatalysts," *Applied Catalysis A: General*, vol. 384, no. 1-2, pp. 58–64, 2010.

[102] R. Narayanan and M. A. El-Sayed, "Effect of colloidal nanocatalysis on the metallic nanoparticle shape: the Suzuki reaction," *Langmuir*, vol. 21, no. 5, pp. 2027–2033, 2005.

[103] C. Dai, C. Wang, R. Hu et al., "Photonic/magnetic hyperthermia-synergistic nanocatalytic cancer therapy enabled by zero-valence iron nanocatalysts," *Biomaterials*, vol. 219, article 119374, 2019.

[104] A. R. Hajipour and P. Abolfathi, "Nickel embedded on triazole-modified magnetic nanoparticles: a novel and sustainable heterogeneous catalyst for Hiyama reaction in fluoride-free condition," *Catalysis Communications*, vol. 103, pp. 92–95, 2017.

[105] M. Hałupka-Bryl, M. Bednarowicz, B. Dobosz et al., "Doxorubicin loaded PEG-b-poly(4-vinylbenzylphosphonate) coated magnetic iron oxide nanoparticles for targeted drug delivery," *Journal of Magnetism and Magnetic Materials*, vol. 384, pp. 320–327, 2015.

[106] L. Li, C. Zeng, L. Ai, and J. Jiang, "Synthesis of reduced graphene oxide-iron nanoparticles with superior enzyme-mimetic activity for biosensing application," *Journal of Alloys and Compounds*, vol. 639, pp. 470–477, 2015.

[107] H. J. Kim, S.-M. Lee, K.-H. Park, C. H. Mun, Y.-B. Park, and K.-H. Yoo, "Drug-loaded gold/iron/gold plasmonic nanoparticles for magnetic targeted chemo-photothermal treatment of rheumatoid arthritis," *Biomaterials*, vol. 61, pp. 95–102, 2015.

[108] D.-W. Cho, H. Song, F. W. Schwartz, B. Kim, and B.-H. Jeon, "The role of magnetite nanoparticles in the reduction of nitrate in groundwater by zero-valent iron," *Chemosphere*, vol. 125, pp. 41–49, 2015.

[109] A. Saritha, B. Raju, D. N. Rao, A. Roychowdhury, D. Das, and K. A. Hussain, "Facile green synthesis of iron oxide nanoparticles via solid-state thermolysis of a chiral, 3D anhydrous potassium tris(oxalato)ferrate(III) precursor," *Advanced Powder Technology*, vol. 26, no. 2, pp. 349–354, 2015.

[110] J. Castelló, M. Gallardo, M. A. Busquets, and J. Estelrich, "Chitosan (or alginate)-coated iron oxide nanoparticles: a comparative study," *Colloids and Surfaces A: Physicochemical and Engineering Aspects*, vol. 468, pp. 151–158, 2015.

[111] R. Li, Y. Gao, X. Jin, Z. Chen, M. Megharaj, and R. Naidu, "Fenton-like oxidation of 2,4-DCP in aqueous solution using iron-based nanoparticles as the heterogeneous catalyst," *Journal of Colloid and Interface Science*, vol. 438, pp. 87–93, 2015.

[112] J. Park, E. Lee, N.-M. Hwang et al., "One-nanometer-scale size-controlled synthesis of monodisperse magnetic iron oxide nanoparticles," *Angewandte Chemie*, vol. 117, no. 19, pp. 2932–2937, 2005.

[113] L. C. Varanda, M. Jafelicci, P. Tartaj et al., "Structural and magnetic transformation of monodispersed iron oxide particles in a reducing atmosphere," *Journal of Applied Physics*, vol. 92, no. 4, pp. 2079–2085, 2002.

[114] F. Dumestre, B. Chaudret, C. Amiens, P. Renaud, and P. Fejes, "Superlattices of iron nanocubes synthesized from $Fe[N(SiMe_3)_2]_2$," *Science*, vol. 303, no. 5659, pp. 821–823, 2004.

[115] R. V. Jagadeesh, T. Stemmler, A.-E. Surkus, H. Junge, K. Junge, and M. Beller, "Hydrogenation using iron oxide-based nanocatalysts for the synthesis of amines," *Nature Protocols*, vol. 10, no. 4, pp. 548–557, 2015.

[116] J. Wu, G. Gao, Y. Li, P. Sun, J. Wang, and F. Li, "Highly chemoselective hydrogenation of lactone to diol over efficient copper-based bifunctional nanocatalysts," *Applied Catalysis B: Environmental*, vol. 245, pp. 251–261, 2019.

[117] H. Ajamein, M. Haghighi, R. Shokrani, and M. Abdollahifar, "On the solution combustion synthesis of copper based nanocatalysts for steam methanol reforming: effect of precursor, ultrasound irradiation and urea/nitrate ratio," *Journal of Molecular Catalysis A: Chemical*, vol. 421, pp. 222–234, 2016.

[118] S. B. Bagherzadeh and M. Haghighi, "Plasma-enhanced comparative hydrothermal and coprecipitation preparation of $CuO/ZnO/Al_2O_3$ nanocatalyst used in hydrogen production via methanol steam reforming," *Energy Conversion and Management*, vol. 142, pp. 452–465, 2017.

[119] S. Allahyari, M. Haghighi, A. Ebadi, and S. Hosseinzadeh, "Ultrasound assisted co-precipitation of nanostructured $CuO\text{-}ZnO\text{-}Al_2O_3$ over HZSM-5: effect of precursor and irradiation power on nanocatalyst properties and catalytic performance for direct syngas to DME," *Ultrasonics Sonochemistry*, vol. 21, no. 2, pp. 663–673, 2014.

[120] J. Baneshi, M. Haghighi, N. Jodeiri, M. Abdollahifar, and H. Ajamein, "Homogeneous precipitation synthesis of $CuO\text{-}ZrO_2\text{-}CeO_2\text{-}Al_2O_3$ nanocatalyst used in hydrogen production via methanol steam reforming for fuel cell applications," *Energy Conversion and Management*, vol. 87, pp. 928–937, 2014.

[121] S. Danwittayakul and J. Dutta, "Two step copper impregnated zinc oxide microball synthesis for the reduction of activation energy of methanol steam reformation," *Chemical Engineering Journal*, vol. 223, pp. 304–308, 2013.

[122] M. Haruta, N. Yamada, T. Kobayashi, and S. Iijima, "Gold catalysts prepared by coprecipitation for low-temperature oxidation of hydrogen and of carbon monoxide," *Journal of Catalysis*, vol. 115, no. 2, pp. 301–309, 1989.

[123] J. Papavasiliou, "Interaction of atomically dispersed gold with hydrothermally prepared copper-cerium oxide for preferential CO oxidation reaction," *Catalysis Today*, 2019.

[124] L. Qin, G. Zeng, C. Lai et al., "Synthetic strategies and application of gold-based nanocatalysts for nitroaromatics reduction," *Science of the Total Environment*, vol. 652, pp. 93–116, 2018.

[125] X. Sun, F. Li, J. Shi et al., "Gold nanoparticles supported on $MgO_x\text{-}Al_2O_3$ composite oxide: an efficient catalyst for selective hydrogenation of acetylene," *Applied Surface Science*, vol. 487, pp. 625–633, 2019.

[126] A. Monopoli, A. Afzal, C. di Franco et al., "Design of novel indium oxide supported gold nanocatalysts and their application in homocoupling of arylboronic acids," *Journal of Molecular Catalysis A: Chemical*, vol. 386, pp. 101–107, 2014.

[127] H. S. Devi, N. R. Singh, H. P. Singh, and T. D. Singh, "Facile synthesis of biogenic gold nanocatalyst for efficient degradation of organic pollutants," *Journal of Environmental Chemical Engineering*, vol. 3, no. 3, pp. 2042–2049, 2015.

[128] T. Xiao, J. Huang, D. Wang, T. Meng, and X. Yang, "Au and Au-based nanomaterials: synthesis and recent progress in electrochemical sensor applications," *Talanta*, vol. 206, article 120210, 2019.

[129] A. E. Shanahan, M. McNamara, J. A. Sullivan, and H. J. Byrne, "An insight into the superior performance of a gold

nanocatalyst on single wall carbon nanotubes to that on titanium dioxide and amorphous carbon for the green aerobic oxidation of aromatic alcohols," *New Carbon Materials*, vol. 32, no. 3, pp. 242–251, 2017.

[130] S. Chairam, W. Konkamdee, and R. Parakhun, "Starch-supported gold nanoparticles and their use in 4-nitrophenol reduction," *Journal of Saudi Chemical Society*, vol. 21, no. 6, pp. 656–663, 2015.

[131] A. Shajkumar, B. Nandan, S. Sanwaria et al., "Silica-supported Au@ hollow-SiO_2 particles with outstanding catalytic activity prepared via block copolymer template approach," *Journal of Colloid and Interface Science*, vol. 491, pp. 246–254, 2017.

[132] P. Sudarsanam, B. Mallesham, A. Rangaswamy, B. G. Rao, S. K. Bhargava, and B. M. Reddy, "Promising nanostructured gold/metal oxide catalysts for oxidative coupling of benzylamines under eco-friendly conditions," *Journal of Molecular Catalysis A: Chemical*, vol. 412, pp. 47–55, 2016.

[133] D. Shah and H. Kaur, "Resin-trapped gold nanoparticles: an efficient catalyst for reduction of nitro compounds and Suzuki-Miyaura coupling," *Journal of Molecular Catalysis A: Chemical*, vol. 381, pp. 70–76, 2014.

[134] C. Wang, H. Yin, S. Dai, and S. Sun, "A general approach to noble metal-metal oxide dumbbell nanoparticles and their catalytic application for CO oxidation," *Chemistry of Materials*, vol. 22, no. 10, pp. 3277–3282, 2010.

[135] Y. Lee, M. A. Garcia, N. A. Frey Huls, and S. Sun, "Synthetic tuning of the catalytic properties of Au-Fe_3O_4 nanoparticles," *Angewandte Chemie International Edition*, vol. 49, no. 7, pp. 1271–1274, 2010.

[136] F. Lin and R. Doong, "Bifunctional Au-Fe_3O_4 heterostructures for magnetically recyclable catalysis of nitrophenol reduction," *The Journal of Physical Chemistry C*, vol. 115, no. 14, pp. 6591–6598, 2011.

[137] H. Veisi, N. Dadres, P. Mohammadi, and S. Hemmati, "Green synthesis of silver nanoparticles based on oil-water interface method with essential oil of orange peel and its application as nanocatalyst for A3 coupling," *Materials Science and Engineering: C*, vol. 105, article 110031, 2019.

[138] R. Sedghi, S. Asadi, B. Heidari, and M. M. Heravi, "TiO_2/polymeric supported silver nanoparticles applied as superior nanocatalyst in reduction reactions," *Materials Research Bulletin*, vol. 92, pp. 65–73, 2017.

[139] P. Paul, P. Bhanja, N. Salam et al., "Silver nanoparticles supported over mesoporous alumina as an efficient nanocatalyst for *N*-alkylation of hetero (aromatic) amines and aromatic amines using alcohols as alkylating agent," *Journal of Colloid and Interface Science*, vol. 493, pp. 206–217, 2017.

[140] Y. Junejo and M. Safdar, "Highly effective heterogeneous doxycycline stabilized silver nanocatalyst for the degradation of ibuprofen and paracetamol drugs," *Arabian Journal of Chemistry*, 2015.

[141] Q. Yi, H. Chu, M. Tang, Z. Yang, Q. Chen, and X. Liu, "Carbon nanotube-supported binary silver-based nanocatalysts for oxygen reduction reaction in alkaline media," *Journal of Electroanalytical Chemistry*, vol. 739, pp. 178–186, 2015.

[142] B. K. Ghosh, D. Moitra, M. Chandel, H. Lulla, and N. N. Ghosh, "Ag nanoparticle immobilized mesoporous TiO_2-cobalt ferrite nanocatalyst: a highly active, versatile, magnetically separable and reusable catalyst," *Materials Research Bulletin*, vol. 94, pp. 361–370, 2017.

[143] U. Mandi, A. S. Roy, S. K. Kundu, S. Roy, A. Bhaumik, and S. M. Islam, "Mesoporous polyacrylic acid supported silver nanoparticles as an efficient catalyst for reductive coupling of nitrobenzenes and alcohols using glycerol as hydrogen source," *Journal of Colloid and Interface Science*, vol. 472, pp. 202–209, 2016.

[144] Z. Ye, L. Hu, J. Jiang, J. Tang, X. Cao, and H. Gu, "CuO@Ag as a highly active catalyst for the selective oxidation of *trans*-stilbene and alcohols," *Catalysis Science & Technology*, vol. 2, no. 6, pp. 1146–1149, 2012.

[145] C. Chen, J. Qu, C. Cao, F. Niu, and W. Song, "CuO nanoclusters coated with mesoporous SiO_2 as highly active and stable catalysts for olefin epoxidation," *Journal of Materials Chemistry*, vol. 21, no. 15, pp. 5774–5779, 2011.

[146] M. J. Borah, A. Devi, R. Borah, and D. Deka, "Synthesis and application of Co doped ZnO as heterogeneous nanocatalyst for biodiesel production from non-edible oil," *Renewable Energy*, vol. 133, pp. 512–519, 2019.

[147] E. Vessally, M. Babazadeh, A. Hosseinian, S. Arshadi, and L. Edjlali, "Nanocatalysts for chemical transformation of carbon dioxide," *Journal of CO2 Utilization*, vol. 21, pp. 491–502, 2017.

[148] A. Esmaeili and S. Kakavand, "Nanocomposites with different metals as magnetically separable nanocatalysts for oxidation of aldehydes," *Comptes Rendus Chimie*, vol. 19, no. 8, pp. 936–941, 2016.

[149] R. Madhuvilakku and S. Piraman, "Biodiesel synthesis by TiO_2-ZnO mixed oxide nanocatalyst catalyzed palm oil transesterification process," *Bioresource Technology*, vol. 150, pp. 55–59, 2013.

[150] R. Bharati and S. Suresh, "Biosynthesis of ZnO/SiO_2 nanocatalyst with palash leaves' powder for treatment of petroleum refinery effluent," *Resource-Efficient Technologies*, vol. 3, no. 4, pp. 528–541, 2017.

[151] G. R. Andrade, C. C. Nascimento, E. C. Silva Júnior, D. T. S. L. Mendes, and I. F. Gimenez, "ZnO/Au nanocatalysts for enhanced decolorization of an azo dye under solar, UV-A and dark conditions," *Journal of Alloys and Compounds*, vol. 710, pp. 557–566, 2017.

[152] J. Albadi, A. Alihosseinzadeh, and M. Mardani, "Efficient approach for the chemoselective acetylation of alcohols catalyzed by a novel metal oxide nanocatalyst CuO-ZnO," *Chinese Journal of Catalysis*, vol. 36, no. 3, pp. 308–313, 2015.

[153] H. Ajamein, M. Haghighi, and S. Alaei, "The role of various fuels on microwave-enhanced combustion synthesis of CuO/ZnO/Al_2O_3 nanocatalyst used in hydrogen production via methanol steam reforming," *Energy Conversion and Management*, vol. 137, pp. 61–73, 2017.

[154] S. Minaei, M. Haghighi, N. Jodeiri, H. Ajamein, and M. Abdollahifar, "Urea-nitrates combustion preparation of CeO_2-promoted CuO/ZnO/Al_2O_3 nanocatalyst for fuel cell grade hydrogen production via methanol steam reforming," *Advanced Powder Technology*, vol. 28, no. 3, pp. 842–853, 2017.

[155] K. Ranjith and R. R. Kumar, "Surfactant free, simple, morphological and defect engineered ZnO nanocatalyst: effective study on sunlight driven and reusable photocatalytic properties," *Journal of Photochemistry and Photobiology A: Chemistry*, vol. 329, pp. 35–45, 2016.

[156] I. Saikia, M. Hazarika, and C. Tamuly, "Synthesis, characterization of bio-derived ZnO nanoparticles and its catalytic activity," *Materials Letters*, vol. 161, pp. 29–32, 2015.

Hindawi
Journal of Nanomaterials
Volume 2019, Article ID 6126031, 7 pages
https://doi.org/10.1155/2019/6126031

Research Article

Solid-Phase Hydrogen Storage Based on NH_3BH_3-SiO_2 Nanocomposite for Thermolysis

Joon-Hyung Jin, Seunghun Shin, and Jihoon Jung

Department of Chemical Engineering, Kyonggi University, 154-42 Gwanggyosan-ro, Yeongtong-gu, Suwon-si, Gyeonggi-do 16227, Republic of Korea

Correspondence should be addressed to Jihoon Jung; jhjung@kgu.ac.kr

Received 26 February 2019; Accepted 30 July 2019; Published 2 September 2019

Guest Editor: Nour F. Attia

Current H_2-proton exchange membrane fuel cell systems available for commercial applications employ heavy and high-risk physical hydrogen storage containers. However, these compressed or liquefied H_2-containing cylinders are only suitable for ground-based electric vehicles, because although highly purified H_2 can be stored in a cylinder, it is not compatible with unmanned aerial vehicles (UAVs), which require a lighter and more stable energy source. Here, we introduce a chemical hydrogen storage composite, composed of ammonia borane (AB) as a hydrogen source and various heterogeneous catalysts, to elevate the thermal dehydrogenation rate. Nanoscale SiO_2 catalysts with a cotton structure dramatically increase the hydrogen evolution rate on demand, while simultaneously lowering the startup temperature for AB thermolysis. Results show that the dehydrogenation reaction of AB with a cotton-structured SiO_2 nanocatalyst composite occurs below 90°C, the reaction time is less than a minute, and the hydrogen generation yield is over 12 wt%, with an activation energy of 63.9 kJ·mol^{-1}.

1. Introduction

Hydrogen—an abundant element in the universe—is a theoretically eco-friendly fuel and a clean energy source for fuel cells, as it produces no environmentally hazardous exhaust. Recent interest in hydrogen fuel has centered on how to safely store hydrogen with enhanced energy density. Essentially, there are two major hydrogen storage methods available: physical and chemical storage, where the latter includes sorbents, metal hydrides, and chemical hydrides [1]. Most commercially available hydrogen fuel cell-driven automobiles utilize physical storage, which is more reliable than chemical storage because pure hydrogen molecules are highly compressed, or even liquefied, to be stored in a physical storage tank. However, continuously raised safety concerns and the heavy weights of hydrogen fuel containers, which are absolutely incompatible with aerial vehicles, limit the employment of physical storage for some ground-based transportation vehicles.

Chemical hydrides store hydrogen fuel in various hydride forms such as sodium borohydride, alane, and ammonia borane (AB). These hydride compounds can be decomposed thermally or hydrolytically to generate H_2 gas. Although hydrolytic dehydrogenation of chemical hydrides occurs at temperatures lower than 80°C, the requirement of expensive catalysts for hydrolysis, the production of ammonia as a byproduct, and the low H_2 yield are practically incompatible with aerial vehicles [2–8]. Thermolysis of the chemical hydride does not require a noble metal catalyst and is relatively free of ammonia poisoning [9–11]. The H_2 yield through thermolysis of AB, which is a frequently employed hydride compound belonging to the chemical hydride group, can be increased up to 13 wt% [9]. In addition, a mixed approach has been introduced, involving a combination of both thermolysis and hydrolysis in series for the dehydrogenation of the AB-TiO_2 composite to enhance the hydrogen yield to the theoretical maximum [12]. Nevertheless, a high temperature requirement for the thermal dehydrogenation reaction and ammonia poisoning through trace amounts of water content in a reactor or reactants remain challenging.

In accordance with recent demands for unmanned aerial vehicles (UAVs) for aerial surveys, weather observations,

radio communication relays, and military purposes [13], here, we propose AB as a component for a disposable hydrogen fuel composite, which can be used for proton exchange membrane fuel cells (PEMFC). As an alternative energy storage device, a PEMFC powered by hydrogen fuel can immediately take advantage of the high efficiency of PEMFC (~50%) and high specific energy density of H_2 gas (~39,500 Wh·kg^{-1}). Indeed, a mechanically low-noise H_2-PEMFC system will perform better for a long-distance and low-altitude flight with UAVs than secondary lithium batteries, which are presently widely utilized, but commonly suffer from low energy density (~250 Wh·kg^{-1}) [14, 15]. Safe hydrogen storage and effective hydrogen generation on demand are of considerable importance in H_2-PEMFC power supply systems. Although some research on hydrogen storage/generation methods for PEMFC-based UAVs has been conducted [16, 17], a further enhanced energy density and highly efficient chemical hydride composite to reduce the weights of UAVs and effectively optimize PEMFC-based power pack systems are still required, especially for longer duration flights with UAVs [18–20].

AB contains 19.6 wt% of high hydrogen content per unit of mass. However, the thermal dehydrogenation temperature should be increased up to hundreds of degrees Celsius to obtain the theoretical maximum H_2 yield. Finding an appropriate catalyst to decrease the working temperature of the AB decomposition reaction with increased H_2 yield is of considerable importance. In this work, we present a characterization of a specifically designed chemical hydride composite, composed of AB and SiO_2 nanopowders (NP). Other researchers have reported on the availability of silicon-based catalysts, including quartz wool and mesoporous silica, in the thermal decomposition of AB. However, the actual working mechanism is not yet clearly understood [21–25]. Furthermore, the characteristics of the AB-SiO_2 NP composite are compared with those of other AB composites, containing various catalysts such as zeolites, metal, and metal oxide NP and boric acid (BA) as an additive. The optimization of the weight ratio between the AB and the catalysts is described, as well as the screening of the composites for fast H_2 evolution rate and low dehydrogenation temperature, to meet the demands of PEMFC-driven UAVs. Fourier transform infrared (FTIR) spectroscopy (ALPHA series, Bruker Corp.) is utilized to verify the hydrogen evolution of AB by thermolysis.

2. Materials and Methods

2.1. Catalyst Preparation and Reactor Design. Commercial zeolite ammonium ZSM-5 powder (CBV2314) is available from Zeolyst International (PA, USA). Laboratory preparation of the ZSM-5 in an attempt to remove tetrapropylammonium hydroxide (TPAOH) is as follows: Sodium aluminate dispersed in a basic aqueous medium is mixed in a flask with a basic Ludox® AS-40 colloidal silica suspension (40 wt% in H_2O) and stirred at room temperature for 3 h. Then, the suspended solution (the weight percentage of Si to Al is 67) is autoclaved at 190°C and 1.013 MPa for 12 h, and finally, the hydrothermally synthesized white powder-dispersed solution is filtrated and dried at 110°C overnight to produce the sodium-substituted TPAOH-free ZSM-5 catalyst (Na-ZSM-5). Na-ZSM-5 can be further stirred in a flask with ammonium nitrate at 80°C for 4 h. After filtration and drying at 110°C, the white product is calcined in an electric furnace at 600°C for 4 h to obtain hydrogen-substituted ZSM-5 (H-ZSM-5). The other materials and reagents are of analytical grade and purchased from Sigma-Aldrich (Milwaukee, USA), unless stated otherwise.

The laboratory-made hydrogen evolution reactor is composed of three thermocouples and a pressure gauge (Figures 1(a) and 1(b)). Thermocouple 1 directly measures the inside temperature of the vial that actually contains a fuel composite of AB and various catalysts and is feedback-controlled for precise control of the working temperature of the dehydrogenation reaction. Thermocouples 2 and 3 determine the temperatures of the inside and outside of the reactor, respectively, and the temperature difference between them gives the approximate energy loss of the reactor. The pressure gauge determines the amount of hydrogen gas generated by the heat-liberating AB dehydrogenation reaction.

2.2. Preparation of Fuel Composites. The weight of a fuel composite is 0.15 g. An AB : SiO_2 NP = 6 : 4 composite contains nine portions of AB (0.09 g) and six portions of SiO_2 NP (0.06 g). If the ratio were 8 : 2, then the composite would contain 0.12 g AB and 0.03 g SiO_2 NP. All reagent components are stored in a desiccator before use, to remove traces of water. After mixing both components gently in a 2 mL volume vial, the fuel composite is carefully placed in the reactor, followed by argon gas being blown into the reactor for 1 min. Then, the heating block increases the reactor temperature at a rate of 2°C min^{-1}.

2.3. Thermolysis of Ammonia Borane. The theoretical maximum H_2 yield from AB is 19.6 wt%: one-third of the hydrogen is generated at around 120°C, another third is dehydrogenated at around 160°C, and the final third requires over 500°C [26–28] (see Supplementary Material Fig. S1). Thermal dehydrogenation of AB can avoid the ammonia poisoning commonly observed in catalytic hydrolysis of AB, which generates one unit of ammonia for every three units of generated hydrogen. Even a level of ammonia of a few ppm can poison a PEMFC, depending on the exposure time to ammonia [29]. Although sodium borohydride ($d \approx 1.074$ g cm^{-3}) does not contain any amine or ammonia substituents and may provide a good alterative hydrogen fuel source without ammonia poisoning, the lighter AB ($d \approx 0.78$ g cm^{-3}) is a better energy source for aerial vehicles.

3. Results and Discussion

Various catalysts with an additive such as SiO_2 NP, aluminosilicate zeolites (CBV2314, H-ZSM-5, and Na-ZSM-5), Ni NP, metal oxides (ZrO_2, TiO_2, and Al_2O_3), and BA are compared in terms of the H_2 yield, reaction time, and onset reaction temperature for the thermal dehydrogenation of AB. The highly exothermic dehydrogenation reaction of AB

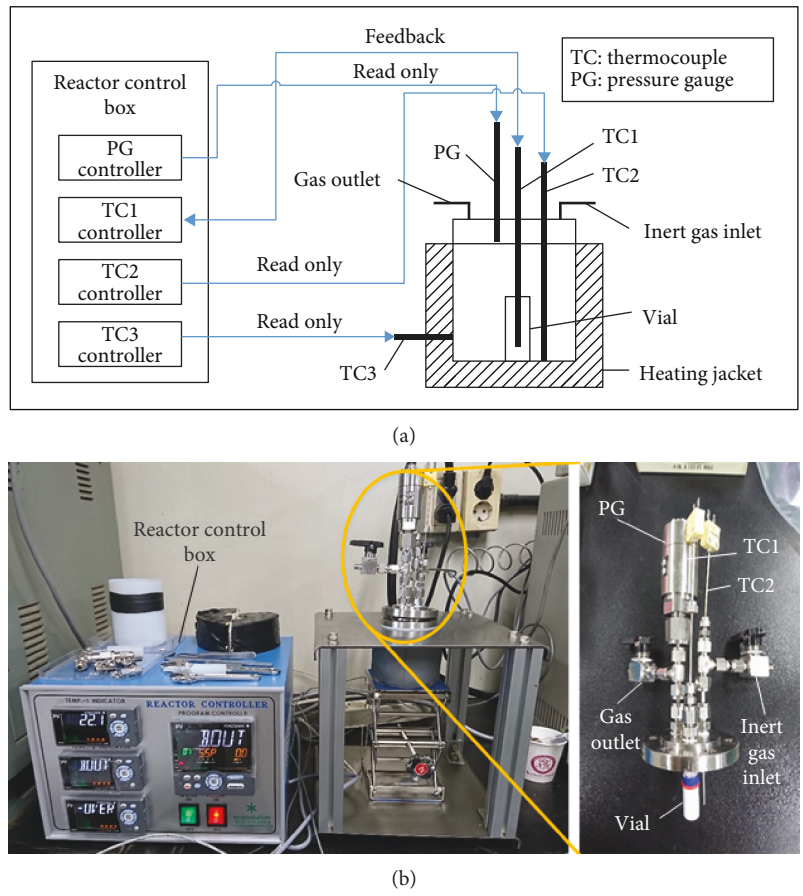

FIGURE 1: (a) Schematic drawing of the laboratory-made hydrogen evolution reactor, and (b) photo images. Note that the reactor is composed of three thermocouples, a pressure gauge (0–700 kPa), and the reactor controller box, which is interfaced with a PC. The inner volume of the reactor is approximately 44.6 mL.

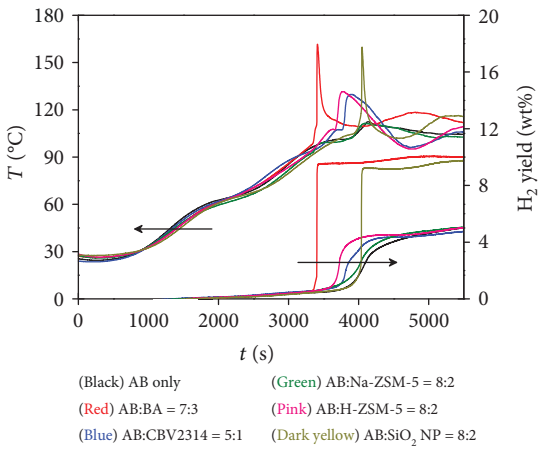

FIGURE 2: Thermolytic dehydrogenation of AB in the presence of various additives or catalysts. The set temperature is 100°C, and the heating rate is 2°C·min^{-1}. Dehydrogenation of AB is a strong exothermic reaction, and an increase in temperature is observed with H_2 gas evolution.

yields a sharp increase in temperature with the release of H_2 gas (Figure 2). As an additive, BA, which has achieved the best known thermal dehydrogenation performance for AB, produces a H_2 yield of 9.56 wt%. This means that a 2.15 mole of H_2 gas is generated for one mole of AB, based on the ideal gas equation of state, considering that the optimized weight ratio between AB and BA for the hydrogen evolution reactor employed in this work, shown in Figure 1, is 7 : 3.

The weight ratio optimization of the AB–BA composite is described in the Supplementary Material, Fig. S2. The mole-equivalent H_2 yield increases to 2.20 with the van der Waals equation, i.e., $(P + aN^2/V^2)(V - bN) = NRT$, where van der Waal constants a and b are 0.2453 bar·L^2·mol^{-2} and 0.02651 L·mol^{-1}, respectively. The higher the content ratio of the additives or catalysts in the hydrogen fuel composites, the faster the hydrogen evolution rate, and usually the lower the onset temperature of the dehydrogenation reactions. However, the H_2 yield as a weight percentage, defined by the weight ratio of hydrogen to the total weight of a composite, decreases as the amount of additive or catalyst in the composite increases. The onset temperature of the AB-BA composite is between 94 and 100°C, and the reaction time duration is less than 3 min. The AB-SiO_2 NP composite exhibits a H_2 yield of 9.26 wt% and a reaction time duration of 2 min, which are comparable with those of the AB-BA composite. While the temperature curve of the AB-BA composite exhibits a small shoulder peak directly before the abrupt temperature increase, the AB-SiO_2 NP composite

Table 1: Major catalytic parameters of additives and catalysts involved in the dehydrogenation reaction of AB via thermal decomposition.

Catalyst/additive (wt%)[a]	Onset temp. (°C)	H_2 yield (wt%)	Reaction time (s)
BA (30)	94	9.56	50
SiO_2 NP (20)	91	9.26	118
Na-ZSM-5 (20)	93	5.70	557
H-ZSM-5 (20)	95	5.70	433
CBV2314 (16.7)	94	4.75	749
No catalyst	98	5.05	588

[a]Content ratios are optimized for each additive or catalyst.

exhibits a single sharp peak. The other catalysts exhibit relatively large and wide shoulder peaks. Table 1 summarizes thermolytic parameters of the catalytic dehydrogenation of AB with various additives and catalysts. Only the thermolytic parameters of SiO_2 NP are comparable with those of BA, and the CBV2314 catalyst actually acts as an anticatalyst in AB thermolysis. The H_2 evolution curves of the other metal or metal oxide NP, including Ni, ZrO_2, anatase TiO_2, and Al_2O_3 are also provided (see Supplementary Material Fig. S3), but these exhibit poorer H_2 yields than that of SiO_2 NP, because the metal and metal oxides are significantly heavier and probably less porous than SiO_2 NP, as shown in Figure 3 and Supplementary Material Fig. S4.

In general, heat conduction mechanisms in powders and flake media differ from each other [30, 31]. Heat transfer in a heat conductor is similar to electron transfer in an electric semiconductor. Electron movement in randomly oriented bulk NP becomes faster through directional electron transfer [32, 33]. Similarly, a mechanical arrangement of AB-based fuel composite can allow a faster heat transfer rate in the in-plane direction of the composite. Effective heat transfer during the exothermic dehydrogenation of AB thermolysis enables enhanced hydrogen evolution compared with a simple powder-based AB composite. Hence, it can be assumed that a unidirectional compression force provides the AB-SiO_2 NP composite with a favorable orientation for better heat conduction in the fuel composite. Supplementary Material Fig. S5 illustrates how to prepare directionally favorable AB-SiO_2 NP composite. After gently mixing both components in a vial, the composite is carefully pressed from the top until only half of the original volume is left.

Even though the compositional optimization of the AB-SiO_2 NP composite shows that the 8 : 2 composite appears to provide the best H_2 yield with a minimized time requirement for a given amount of AB composite (Table 1), a greater H_2 yield can be obtained at a different optimized condition with the unidirectionally pressed AB-SiO_2 NP composite (Figure 4). Note that hydrogen gas is liberated even before the sharp temperature peaks are observed. A physically favorable arrangement of the composite increases the H_2 yield by over 20% and decreases the reaction time by approximately 50%. Table 2 summarizes the thermolytic parameters of various AB-SiO_2 NP composites.

The AB thermolysis reaction requires heat to initiate the dehydrogenation reaction, and the set temperature of the reactor strongly affects the H_2 yield, as shown in Figure 5. No reaction occurs at a set temperature of 50°C, meaning that the AB-SiO_2 NP composite is stable under normal atmospheric conditions. As the set temperature increases from 80 to 110°C, the reaction time and H_2 yield increase from 77 to 140 s and 10.37 to 11.67 wt%, respectively. Because a typical PEMFC system functions correctly at a working temperature of around 85°C, it would be reasonable to set the reactor temperature to approximately the same as the operation temperature of the PEMFC. Otherwise, additional equipment for insulation is required to thermally separate the PEMFC system from the hydrogen fuel supplier. The activation energy (E_a) of the SiO_2 NP-catalyzed dehydrogenation reaction of AB is 63.9 kJ·mol^{-1} (Supplementary Material Fig. S6). This is just one-third of the typical activation barrier of 180 kJ·mol^{-1} to the AB decomposition reaction [34].

Figure 6 shows the FTIR spectra of the AB-SiO_2 NP composite. Boron, nitrogen, and hydrogen atoms in a tetrahedral backbone with covalent single bonds lead to three characteristic FTIR bands for AB (Supplementary Material Fig. S7): the peaks observed in a range of 648–1822 cm^{-1} are assigned to B-N stretching vibrations, peaks between 2260 and 2820 cm^{-1} are assigned to B-H stretching vibrations, and N-H stretching modes are observed in a range of 3167–3712 cm^{-1} [21, 35, 36]. The evolution of hydrogen gas by heating the composite increases the bond order along the principal axis of AB. This means that the π-bond character becomes involved, in addition to the σ-bond character, and stretching frequencies are upshifted upon the bond order increase. More importantly, the B-H and N-H stretching intensities diminish when a large quantity of hydrogen gas is generated. As shown in Figure 6, both the B-H and N-H stretching intensities are considerably reduced after the thermal decomposition of AB, and the same result is observed with additive BA (Supplementary Material Fig. S7).

4. Conclusions

In this work, AB, a stable chemical hydride at room temperature and pressure, was thermally decomposed to produce hydrogen gas at a temperature of approximately 90°C, in the presence of SiO_2 NP. We designed our own hydrogen evolution reactor and hydrogen fuel composite to directly compare the results for the AB-SiO_2 NP composite with that of AB-BA, which has achieved the best thermolytic performance in other studies with a composite ratio of AB : BA of 8 : 2. The H_2 yield of the AB-SiO_2 NP composite (AB : SiO_2 NP = 7 : 3 in wt%) was 9.26 wt%, and the yield of the mechanically pressed one (8.5 : 1.5 composite in wt%) was 12 wt%, with a reaction time of less than a minute, which is comparable to that of the AB-BA composite. In general, chemical hydride-based hydrogen fuel composites for H_2-PEMFC for aerial vehicles should satisfy the following criteria: It should be sufficiently stable not to be dehydrogenated at a conventional atmospheric condition (<50°C), have a high capability for hydrogen storage to save

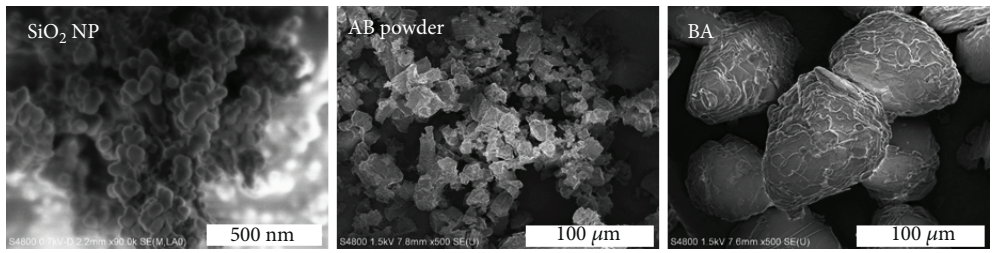

Figure 3: SEM images of the components of hydrogen fuel composites. SiO_2 NP shows much better porosity than those of AB and BA powders.

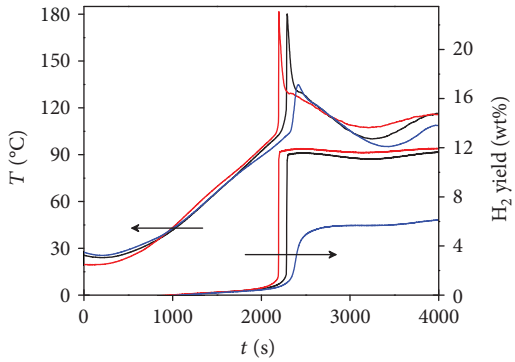

Figure 4: Hydrogen evolution curves and the catalytic parameters of various compositional ratios between AB and SiO_2 NP. The best result is obtained for the 8.5 : 1.5 composite, achieving 12.00 wt% H_2 yield, with a reaction time duration of less than 1 min.

Table 2: Hydrogen evolution parameters of various AB-SiO_2 NP composites in the dehydrogenation reaction of AB via thermolysis.

Composites	Onset temp. (°C)	H_2 yield (wt%)[a]	Reaction time (s)
AB : SiO_2 NP = 8 : 2	90	11.59	106
AB : SiO_2 NP = 8.5 : 1.5	89	12.00	48
AB : SiO_2 NP = 9 : 1	91	5.67	95

[a]1.0217 times increased by data fitting with the van der Waals equation instead of the ideal gas equation. Note that some harmful byproducts, e.g., NH_3 gas, may be included at an approximate level of thousands of ppm for each sample.

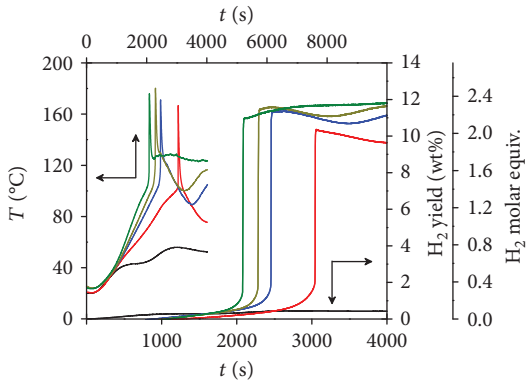

Figure 5: Hydrogen evolution curves at 50°C (black), 80°C (red), 90°C (blue), 100°C (dark yellow), and 110°C (green). The corresponding Arrhenius plot to measure the activation energy of the thermal dehydrogenation reaction of AB in the presence of the SiO_2 NP catalyst is also available (Supplementary Material Fig. S6). Note that mechanically pressed composites were employed, as shown in Supplementary Material Fig. S5, and the AB content in each composite is equal to 80 wt%.

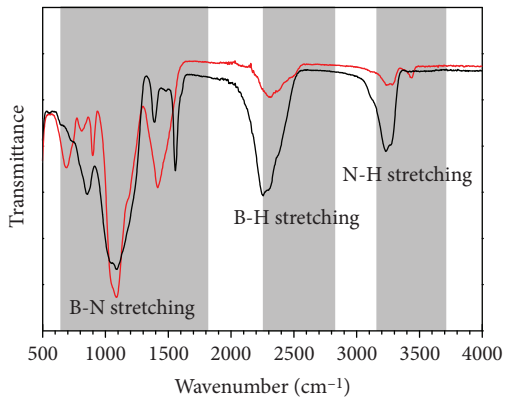

Figure 6: FTIR spectra of AB-SiO_2 NP composite before (black solid line) and after (red solid line) the thermal dehydrogenation reaction. H_2 gas evolution increases the bond order along the principal axis of AB. Therefore, the B-N stretching frequencies are upshifted, and the B-H and N-H stretching intensities decrease simultaneously.

weight, achieve a fast hydrogen evolution rate on demand at a temperature of less than 90°C, and have an in-built hydrogen fuel filtration system for the sake of ammonia-susceptible PEMFC (we did not seriously consider the by-product issue in the present work) [1]. The hydrogen evolution curves of the AB-SiO_2 NP composites showed that none of the compositional ratios investigated in this work thermally decomposed at a temperature below 50°C. Once the thermal dehydrogenation of AB occurred, the reaction ended within a couple of minutes. More precise optimization of the weight ratio between the two components, concerning not only compositional optimization but also the physical shape, density, and molecular orientation, could additionally enhance the hydrogen storage capability and

eventually reduce the total weight of a power generation package for UAVs. Given a thermally shielded fuel cartridge, the AB-SiO_2 NP composite could lead to the commercialization of disposable hydrogen fuel for UAVs.

Data Availability

The data used to support the findings of this study are included within the article. Additional information could be obtained from the supplementary materials.

Conflicts of Interest

The authors declare that there is no conflict of interest regarding the publication of this paper.

Authors' Contributions

The first and second authors contributed equally to this work.

Acknowledgments

This study was supported by the Agency for Defense Development (ADD) of Korea (Grant number 17-114-407-038).

Supplementary Materials

Fig. S1: TGA of pure AB. Thermal behavior of silica gel and SiO2 NP is also shown for comparison. Notable two peaks shown at 120 OC and 160 OC stems from formation of polyamidoboranes and/or polyimidoboranes by the AB decomposition. Note that a slight mass loss of silica gel and SiO2 NP is due to evaporation of the surface-adsorbed water vapor and unspecified polymeric contaminants. Fig. S2: the weight ratio optimization of the AB-BA composites. The onset temperature and the H2 yield of each composite are as follows, respectively: 94 OC and 8.21 wt% for AB : BA = 6 : 4 composites; 98 OC and 9.56 wt% for AB : BA = 7 : 3 composites; 100 OC and 5.55 wt% for AB : BA = 8 : 2 composites. Fig. S3: hydrogen evolution curves of AB composites containing various metal or metal oxide NP such as Ni (black), ZrO2 (red), anatase TiO2 (blue), and Al2O3 (green). H2 yield of each composite is 4.27, 7.44, 3.74, and 3.97 wt% in order. Note that AB content in each composite is the same as 60 wt%. Fig. S4: photo images (×1200) of various metal or metal oxide NP catalysts including Ni ($d \approx 8.91$ g cm^{-3}), ZrO2 ($d \approx 5.68$ g cm^{-3}), anatase TiO2 ($d \approx 3.8$ g cm^{-3}), and Al2O3 ($d \approx 3.99$ g cm^{-3}). Fig. S5: unidirectional compression of AB-SiO2 NP composite to reduce the volume by half. Fig. S6: Arrhenius plot based on the hydrogen evolution curves at 4 different temperatures shown in Figure 5. Note that the obtained E_a from the slope measures 63.9 kJ·mol^{-1}. Fig. S7: (a) FTIR spectra of AB flake and AB powder. Both spectra commonly show 3 characteristic bands, i.e., BN stretching, BH stretching, and NH stretching bands. (b) FTIR spectra of AB and BA composites before and after the thermal dehydrogenation reaction. Note that the BH and NH stretching peaks are simultaneously reduced after the dehydrogenation reaction. *(Supplementary Materials)*

References

[1] H. T. Hwang and A. Varma, "Hydrogen storage for fuel cell vehicles," *Current Opinion in Chemical Engineering*, vol. 5, pp. 42–48, 2014.

[2] C. Li, J. Zhou, W. Gao et al., "Binary Cu–Co catalysts derived from hydrotalcites with excellent activity and recyclability towards NH_3BH_3 dehydrogenation," *Journal of Materials Chemistry A*, vol. 1, no. 17, pp. 5370–5376, 2013.

[3] L. Cui, Y. Xu, L. Niu, W. Yang, and J. Liu, "Monolithically integrated CoP nanowire array: an on/off switch for effective on-demand hydrogen generation via hydrolysis of $NaBH_4$ and NH_3BH_3," *Nano Research*, vol. 10, no. 2, pp. 595–604, 2017.

[4] S. Akbayrak and S. Ozkar, "Ruthenium(0) nanoparticles supported on multiwalled carbon nanotube as highly active catalyst for hydrogen generation from ammonia-borane," *ACS Applied Materials & Interfaces*, vol. 4, no. 11, pp. 6302–6310, 2012.

[5] N. Sahiner and A. O. Yasar, "Imidazolium based polymeric ionic liquid microgels as an alternative catalyst to metal catalysts for H_2 generation from methanolysis of $NaBH_4$," *Fuel Processing Technology*, vol. 152, pp. 316–324, 2016.

[6] M. J. Valero-Pedraza, D. Cot, E. Petit, K. F. Aguey-Zinsou, J. G. Alauzun, and U. B. Demirci, "Ammonia borane nanospheres for hydrogen storage," *Acs Applied Nano Materials*, vol. 2, no. 2, pp. 1129–1138, 2019.

[7] N. Sahiner and F. Seven, "The use of superporous p(AAc (acrylic acid)) cryogels as support for Co and Ni nanoparticle preparation and as reactor in H_2 production from sodium borohydride hydrolysis," *Energy*, vol. 71, pp. 170–179, 2014.

[8] B. Coşkuner, A. Kantürk Figen, and S. Pişkin, "Solid state preparation and reaction kinetics for Co/B as a catalytic/acidic accelerator for $NaBH_4$ hydrolysis," *Reaction Kinetics Mechanisms and Catalysis*, vol. 109, no. 2, pp. 375–392, 2013.

[9] H. T. Hwang, P. Greenan, S. J. Kim, and A. Varma, "Effect of boric acid on thermal dehydrogenation of ammonia borane: H_2 yield and process characteristics," *AICHE Journal*, vol. 59, no. 9, pp. 3359–3364, 2013.

[10] J. Luo, X. Kang, C. Chen, J. Song, D. Luo, and P. Wang, "Rapidly releasing over 9 wt % of H_2 from NH_3BH_3–Mg or NH_3BH_3–MgH_2 composites around 85°C," *Journal of Physical Chemistry C*, vol. 120, no. 33, pp. 18386–18393, 2016.

[11] J. Luo, X. Kang, and P. Wang, "Synthesis, formation mechanism, and dehydrogenation properties of the long-sought $Mg(NH_2BH_3)_2$ compound," *Energy & Environmental Science*, vol. 6, no. 3, pp. 1018–1025, 2013.

[12] O. V. Komova, V. I. Simagina, N. L. Kayl et al., "Improved low-temperature hydrogen generation from NH_3BH_3 and TiO_2 composites pretreated with water," *International Journal of Hydrogen Energy*, vol. 38, no. 15, pp. 6442–6449, 2013.

[13] O. Gonzalez-Espasandin, T. J. Leo, and E. Navarro-Arevalo, "Fuel cells: a real option for unmanned aerial vehicles propulsion," *Scientific World Journal*, vol. 2014, article 497642, 12 pages, 2014.

[14] S. F. J. Flipsen, "Power sources compared: the ultimate truth?," *Journal of Power Sources*, vol. 162, no. 2, pp. 927–934, 2006.

[15] J. M. Tarascon and M. Armand, "Issues and challenges facing rechargeable lithium batteries," *Nature*, vol. 414, no. 6861, pp. 359–367, 2001.

[16] K. Kim, T. Kim, K. Lee, and S. Kwon, "Fuel cell system with sodium borohydride as hydrogen source for unmanned aerial

vehicles," *Journal of Power Sources*, vol. 196, no. 21, pp. 9069–9075, 2011.

[17] J. E. Seo, Y. Kim, Y. Kim et al., "Portable ammonia-borane-based H_2 power-pack for unmanned aerial vehicles," *Journal of Power Sources*, vol. 254, pp. 329–337, 2014.

[18] C. K. Dyer, "Fuel cells for portable applications," *Journal of Power Sources*, vol. 106, no. 1-2, pp. 31–34, 2002.

[19] J. H. Wee, "Applications of proton exchange membrane fuel cell systems," *Renewable & Sustainable Energy Reviews*, vol. 11, no. 8, pp. 1720–1738, 2007.

[20] Z. Liu, Y. Dai, Z. Zheng, and B. Huang, "Covalently-terminated germanane GeH and $GeCH_3$ for hydrogen generation from catalytic hydrolysis of ammonia borane under visible light irradiation," *Catalysis Communications*, vol. 118, pp. 46–50, 2019.

[21] H. T. Hwang, A. Al-Kukhun, and A. Varma, "High and rapid hydrogen release from thermolysis of ammonia borane near PEM fuel cell operating temperatures," *International Journal of Hydrogen Energy*, vol. 37, no. 3, pp. 2407–2411, 2012.

[22] H. T. Hwang, A. Al-Kukhun, and A. Varma, "High and rapid hydrogen release from thermolysis of ammonia borane near PEM fuel cell operating temperatures: effect of quartz wool," *International Journal of Hydrogen Energy*, vol. 37, no. 8, pp. 6764–6770, 2012.

[23] A. Gutowska, L. Li, Y. Shin et al., "Nanoscaffold mediates hydrogen release and the reactivity of ammonia borane," *Angewandte Chemie-International Edition*, vol. 44, no. 23, pp. 3578–3582, 2005.

[24] A. Paolone, O. Palumbo, P. Rispoli, R. Cantelli, T. Autrey, and A. Karkamkar, "Absence of the structural phase transition in ammonia borane dispersed in mesoporous silica: evidence of novel thermodynamic properties," *Journal of Physical Chemistry C*, vol. 113, no. 24, pp. 10319–10321, 2009.

[25] L. Q. Wang, A. Karkamkar, T. Autrey, and G. J. Exarhos, "Hyperpolarized ^{129}Xe NMR investigation of ammonia borane in mesoporous silica," *Journal of Physical Chemistry C*, vol. 113, no. 16, pp. 6485–6490, 2009.

[26] U. B. Demirci, S. Bernard, R. Chiriac, F. Toche, and P. Miele, "Hydrogen release by thermolysis of ammonia borane NH_3BH_3 and then hydrolysis of its by-product $[BNH_x]$," *Journal of Power Sources*, vol. 196, no. 1, pp. 279–286, 2011.

[27] T. Kobayashi, S. Gupta, M. A. Caporini, V. K. Pecharsky, and M. Pruski, "Mechanism of solid-state thermolysis of ammonia borane: a ^{15}N NMR study using fast magic-angle spinning and dynamic nuclear polarization," *Journal of Physical Chemistry C*, vol. 118, no. 34, pp. 19548–19555, 2014.

[28] L. Li, X. Yao, C. Sun et al., "Lithium-catalyzed dehydrogenation of ammonia borane within mesoporous carbon framework for chemical hydrogen storage," *Advanced Functional Materials*, vol. 19, no. 2, pp. 265–271, 2009.

[29] R. Halseid, P. J. S. Vie, and R. Tunold, "Effect of ammonia on the performance of polymer electrolyte membrane fuel cells," *Journal of Power Sources*, vol. 154, no. 2, pp. 343–350, 2006.

[30] C. J. Gomes, M. Madrid, J. V. Goicochea, and C. H. Amon, "In-plane and out-of-plane thermal conductivity of silicon thin films predicted by molecular dynamics," *Journal of Heat Transfer*, vol. 128, no. 11, pp. 1114–1121, 2006.

[31] C. Pohlmann, L. Rontzsch, S. Kalinichenka, T. Hutsch, T. Weissgarber, and B. Kieback, "Hydrogen storage properties of compacts of melt-spun $Mg_{90}Ni_{10}$ flakes and expanded natural graphite," *Journal of Alloys and Compounds*, vol. 509, pp. S625–S628, 2011.

[32] S. H. Kang, S. H. Choi, M. S. Kang et al., "Nanorod-based dye-sensitized solar cells with improved charge collection efficiency," *Advanced Materials*, vol. 20, no. 1, pp. 54–58, 2008.

[33] R. Jose, V. Thavasi, and S. Ramakrishna, "Metal oxides for dye-sensitized solar cells," *Journal of the American Ceramic Society*, vol. 92, no. 2, pp. 289–301, 2009.

[34] A. C. Gangal, P. Kale, R. Edla, J. Manna, and P. Sharma, "Study of kinetics and thermal decomposition of ammonia borane in presence of silicon nanoparticles," *International Journal of Hydrogen Energy*, vol. 37, no. 8, pp. 6741–6748, 2012.

[35] S. Frueh, R. Kellett, C. Mallery et al., "Pyrolytic decomposition of ammonia borane to boron nitride," *Inorganic Chemistry*, vol. 50, no. 3, pp. 783–792, 2011.

[36] J. Zhang, Y. Zhao, D. L. Akins, and J. W. Lee, "CO_2-enhanced thermolytic H_2 release from ammonia borane," *Journal of Physical Chemistry C*, vol. 115, no. 16, pp. 8386–8392, 2011.

Hindawi
Journal of Nanomaterials
Volume 2019, Article ID 2094767, 9 pages
https://doi.org/10.1155/2019/2094767

Research Article

Preparation and Performance of Capric-Myristic Acid Binary Eutectic Mixtures for Latent Heat Thermal Energy Storages

Dongyi Zhou,[1,2,3] **Yuhong Zhou**,[2] **Yicai Liu**,[1] **Xianzhi Luo**,[2] **and Jiawei Yuan**[2]

[1]*School of Energy Science and Engineering, Central South University, Changsha 410083, China*
[2]*School of Mechanical and Energy Engineering, Shaoyang University, Shaoyang 422000, China*
[3]*Key Laboratory of Hunan Province for Efficient Power System and Intelligent Manufacturing, Shaoyang University, Shaoyang 422000, China*

Correspondence should be addressed to Dongyi Zhou; zhoudongyi2005@163.com and Yicai Liu; lyc0301@163.com

Received 10 April 2019; Revised 11 June 2019; Accepted 19 June 2019; Published 19 August 2019

Guest Editor: Jamal Siddiqui

The capric-myristic acid (CA-MA) binary eutectic mixture phase change material (PCM) was prepared for low-temperature latent heat thermal energy storage (LHTES). The thermal properties, thermal stability, and long-term cycling reliability of the PCMs were measured. Differential scanning calorimetry results showed that the CA-MA binary eutectic mixture at the mass ratio (72/28 wt%) indicated a high-performance PCM for its suitable phase change temperature (T_m: 18.21°C, T_f: 17.40°C) and high latent heat (H_m: 148.5 J/g, H_f: 134.0 J/g). Thermal gravimetric analysis results indicated that the CA-MA binary eutectic mixture had excellent thermal stability in its operating temperature range. The thermal cycling tests and Fourier transform infrared spectroscopy results revealed that the CA-MA binary eutectic mixture had good long-term cycling thermal chemical reliability. In summary, in terms of thermal property, thermal stability, and reliability, the prepared CA-MA PCM could be applied particularly for low-temperature LHTES systems and backfill materials of ground source heat pump systems.

1. Introduction

Thermal energy storage technologies have elicited increasing attention due to its broad application prospects in the fields of solar energy utilization, electric power peak-load shifting, industrial waste heat recovery, building heating, and air conditioning [1–5]. Latent heat thermal energy storage (LHTES) has elicited wide attention and application because of its larger storage energy density, less temperature change during energy storage, better stability, and higher safety compared with other methods [6, 7].

The core technology of LHTES is phase change material (PCM). Various inorganic, organic, and mixed PCMs, such as paraffin [8, 9], polyols [10, 11], inorganic salts [12], and fatty acids [13], have been studied in building energy conservation. Among these materials, fatty acid is one of the most relevant organic PCMs because of its several advantages, such as large latent heat, nontoxicity, suitable phase change temperature, zero corrosion, low degree of subcooling, no or minimal volume change, and good thermal stability [14, 15]. Furthermore, fatty acids can be extracted from oils, animal fat, and plants; thus, the raw materials are abundant and readily available [16, 17]. In addition, a low phase change temperature may be achieved by mixing two or more fatty acids on the basis of their eutectic effect [18–20]. Thus, the phase change temperature can be controlled by selecting an appropriate eutectic system formed by different fatty acids for several engineering applications.

Numerous recent studies have been conducted on the performance of fatty acids, such as on their thermal property, thermal stability, and long-term cycling reliability [21, 22]. Sarı et al. [23, 24] studied the thermal properties of many binary eutectic mixture systems, such as the mixtures of lauric-stearic, myristic-palmitic, palmitic-stearonic, lauric-myristic, lauric-palmitic, and myristic-stearic acids; the data measured by differential scanning calorimetry (DSC) showed that the melting temperatures of those binary systems were 37.00° C, 42.60°C, 52.30°C, 34.20°C, 35.20°C, and 44.10°C, respectively, and their phase change latent heat values were

182.70, 169.70, 181.70, 166.80, 166.30, and 182.40 J/g, respectively. Wen et al. [25] prepared a PCM of capric-lauric acid (CA-LA)/diatomite/EG composite and studied its thermal properties. Yuan et al. [26] and Wei et al. [27] prepared some ternary fatty acid composite PCMs and studied their thermal properties. These aforementioned research results prove that PCMs can be applied for solar energy utilization and building energy conservation and have a guiding effect on the development of eutectic mixture fatty acid.

Most of the aforementioned studies focus on single and binary or ternary eutectic fatty acids in the temperature range of 20°C–60°C, mainly used in building energy saving and solar energy utilization. However, as the backfill material in the ground source heat pump (GSHP) system, PCM with a phase change temperature of approximately 19°C has yet to be reported. GSHP is a heat pump technology that utilizes shallow geothermal energy. The heat transfer performance between the buried pipes and around the soil plays a decisive role in the operational stability and operating efficiency of the GSHP. The underground soil temperature is unchanged below 15 m. For example, the temperature is approximately 19°C in Shanghai, China [28]. However, after the GSHP system operates for a certain period of time, the soil temperature around the buried pipe will change, thereby reducing the system operating rate. Thus, the performance of the backfill materials around the buried pipe is particularly important.

In this study, the capric-myristic acid (CA-MA) binary eutectic mixture PCM was prepared for LHTES and as backfill materials around the buried pipe of a GSHP system. The thermal properties and thermal cycling reliability of the materials were tested via DSC, and the thermal decomposition stability was investigated via thermal gravimetric analysis (TGA). In addition, Fourier transform infrared (FTIR) spectroscopy was used to investigate whether the chemical composition of the PCMs changed before and after preparation and determine the possible reason that caused the change of the thermal properties of the materials with the increase in the thermal cycling number.

2. Experiments

2.1. Materials. Capric acid (CA, ≥98.5% purity) and myristic acid (MA, ≥98% purity) were purchased from Shanghai Zhunyun Chemical Co. Ltd.

2.2. Preparation of CA-MA PCMs. The solid CA and MA were weighed separately at different weight ratios from 0 wt% to 100 wt%, and the sample weight errors were controlled within 0.1 mg. Then, the CA and MA were mixed in a beaker. Then, the beaker was stored in a vacuum drying oven at a constant temperature of 80°C for 2 h. After completely melting, the fatty acid mixtures were stirred for 30 min at 60°C and 500 r/min in a magnetic stirrer. The beaker of the molten liquid fatty acid mixtures was then placed in an ultrasonic water bath; the temperature was controlled at 60°C to ensure that the fatty acids were constantly in the melting state. Furthermore, the time of ultrasonic vibration was approximately 2 min to ensure that the two types of fatty acids were sufficiently mixed to form binary eutectic mixtures. With these methods, a set of CA-MA binary eutectic mixtures was prepared.

2.3. Characterization. The phase change temperature (melting temperature (T_m) and freezing temperature (T_f)) and phase change latent heat (melting latent heat (H_m) and freezing latent heat (H_f)) of the samples were determined by DSC (TA Q20, USA) calibrated with indium standard in the temperature range of 0°C–80°C. The temperature increasing rate of DSC measurements had a 5°C/min heating rate. DSC measurements of the same samples were conducted three times, and the accuracy was ±0.1% for phase change temperatures and ±4% for latent heat.

To investigate the effect of the thermal cycling number on thermal properties, the CA-MA eutectic mixtures were heated from solid to liquid state and then cooled from liquid to solid state by a heating controller. The above thermal cycling process was conducted continuously until the values were 500, 1000, and 2000. The changes in the performance of the mixtures were measured by DSC and FT-IR.

The thermal stability of the CA-MA PCM was analyzed by TGA (TA Q50, USA) in the temperature range of 20°C–450°C with a 10°C/min heating rate under nitrogen gas atmosphere and an accuracy of ±0.2%.

The samples of CA, MA, and CA-MA eutectic mixtures were analyzed by FTIR (Thermo Scientific Nicolet iS5, USA). The uncycled and cycled samples were measured by FTIR to explore the reason of the variation of thermal properties of the CA-MA mixtures after thermal cycling.

3. Results and Discussion

3.1. Thermal Properties of CA and MA Used. The CA-MA PCM was prepared by mixing CA and MA at different mass ratios. The phase change temperatures and latent heat of the CA and MA in some references [29–32] are listed in Table 1. The DSC curves of the CA and MA used in this study are shown in Figure 1. The phase change temperatures and latent heat from the curves are shown in Table 1. From the table, the melting points of CA and MA used are 31.17°C and 52.68°C, respectively, and the latent heat values of fusion are 169.4 J/g and 188.6 J/g, respectively. These results suggest that CA and MA can be used as raw materials to produce the CA-MA PCM with suitable phase change temperatures and large latent heat.

3.2. Mass Ratio of CA-MA PCM. In a binary system, if the two solid components are completely immiscible and can form a eutectic system, then the phase system will become a eutectic binary system [33]. In a solid-liquid two-phase equilibrium system of a two-component system whose liquids are completely mutually soluble while the solids are completely immiscible, a temperature lower than the phase change temperature of the two pure components will be observed. At this temperature, the solid mixtures, named the lowest eutectic, which has the same composition as the liquid phase, will precipitate, and its temperature is the lowest eutectic temperature or the lowest eutectic point; similarly, the mechanical mixture of the two solids can also be melted together at the minimum eutectic temperature [34].

Table 1: Thermal properties of pure CA, pure MA, and CA-MA binary eutectic mixture.

PCM	Thermal properties				References
	T_m (°C)	H_m (J/g)	T_f (°C)	H_f (J/g)	
CA	31.53	165.21	32.05	168.43	Sarı et al. [29]
MA	53.51	192.68	53.24	195.36	
CA	27.69	164.7	32.06	163.5	Fu et al. [30]
MA	50.78	203.7	55.17	201.0	
CA	31.5	155.5	—	—	Gao and Qian [31]
MA	51.6	204.5	—	—	
CA	32.14	156.04	32.53	154.24	Karaipekli et al. [32]
MA	53.86	192.58	53.74	190.11	
CA	31.17	169.4	31.69	170.3	This study
MA	52.68	188.6	51.63	193.1	
CA-MA eutectic mixture	18.21	148.5	17.40	134.0	This study

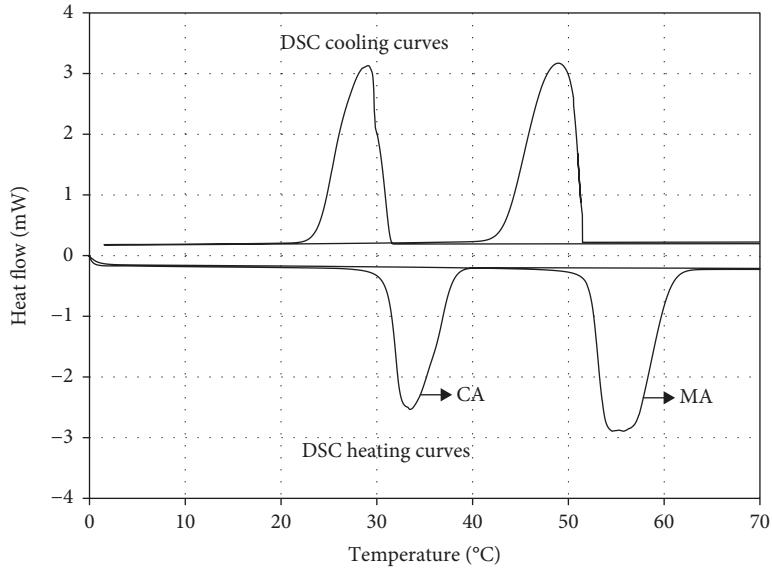

Figure 1: DSC curves of pure CA and pure MA.

Thus, the binary eutectic mixture fatty acids have a lower phase change point than any of the fatty acids. Zhang et al. [35] derived the relationship of melting temperature, latent heat, and content of components A and B and eutectic mixtures based on the second law of thermodynamics and phase equilibrium theory, shown as follows:

$$\begin{cases} -\dfrac{H_A(T_m - T_A)}{T_A} + RT_m \ln(1 - X_A) + G_{A,ex} = 0, \\ -\dfrac{H_B(T_m - T_B)}{T_B} + RT_m \ln(1 - X_B) + G_{B,ex} = 0, \end{cases} \quad (1)$$

where T_m is the phase change temperature of the eutectic mixtures (K); T_A and T_B are the melting temperatures of constituents A and B, respectively (K); H_A and H_B are the latent heat of constituents A and B, respectively (J/mol); X_A and X_B are the mole percent ratio of constituents A and B of the eutectic mixture, respectively, (%) and $\sum(X_A + X_B) = 1$; R is the gas constant (8.315 J/(mol·K)); and $G_{A,ex}$ and $G_{B,ex}$ are the excess free enthalpy of constituents A and B, respectively.

For fatty acids, $G_{A,ex} = G_{B,ex} = 0$ is an excellent approximation. Accordingly, equation (1) can be rewritten as

$$\begin{cases} T_m = \left[\dfrac{1}{T_A} - \dfrac{R \ln X_A}{H_A}\right]^{-1}, \\ T_m = \left[\dfrac{1}{T_B} - \dfrac{R \ln X_B}{H_B}\right]^{-1}. \end{cases} \quad (2)$$

The relevant parameters of CA and MA in Table 1 are replaced in equation (2), and equation (3) can be obtained.

$$\begin{cases} \ln X_{CA} = \dfrac{11.53 - 3509.6}{T_m}, \\ \ln X_{CA} = \dfrac{15.90 - 5179.9}{T_m}. \end{cases} \quad (3)$$

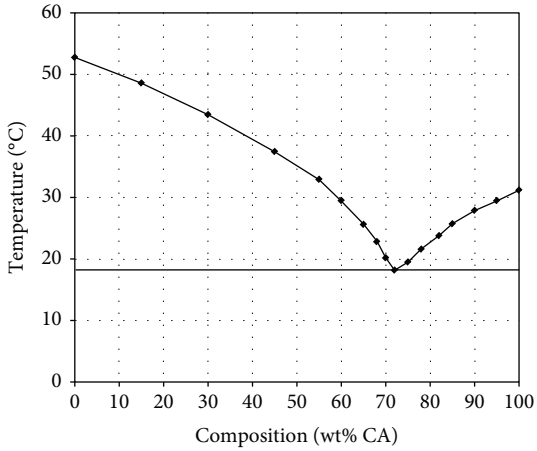

Figure 2: Effects of composition mass ratios (wt%) on the melting temperatures of CA-MA binary eutectic mixtures.

The theoretical phase diagram of the CA-MA eutectic mixtures can be drawn, and the corresponding theoretical ratios and phase change temperatures can be determined by equation (3).

However, experiments have proven that some errors occur if equation (3) is adopted because the purity of a single fatty acid supplied may affect the mass ratio and the phase change temperature. Thus, the actual mass ratios of the eutectic mixtures must be experimentally determined.

The effects of the composition mass ratios on the melting temperatures of the CA-MA binary eutectic mixtures are shown in Figure 2, and the data are taken from our experiments. The melting temperature of the CA-MA binary eutectic mixtures decreases with the increase in the mass ratio of CA, and the temperature range narrows when the mass ratio approaches the eutectic mixing ratio. At the eutectic mixing ratio, the lowest melting temperature is obtained. Then, the melting temperature of the CA-MA mixture increases again with the CA mass ratio. As shown in Figure 2, the lowest melting temperature is 18.21°C at the mass ratio (72% CA/28% MA *w*/*w*). The melting temperature of the CA-MA PCM is lower than that of any of the pure fatty acids.

3.3. Thermal Property of CA-MA PCM. The DSC curve of the prepared CA-MA PCM is shown in Figure 3, and the thermal performance parameters are shown in Table 1. The melting and freezing temperatures are 18.21°C and 17.40°C, respectively, and the melting and freezing latent heat values are 148.5 J/g and 134.0 J/g, respectively. The indoor comfortable temperature range is 16°C–25°C; thus, the eutectic mixture can be used for building LHTES to reduce the load of heating, ventilation, and air conditioning systems in winter and summer. The soil temperature around the buried pipe of the GSHP is approximately 19°C. Therefore, the eutectic mixture can be used as a backfill material of the geothermal heat exchanger to enhance the heat transfer effect and improve the operating efficiency of the GSHP system.

The phase change temperatures and latent heat of the CA-MA mixtures in some references [29–32] are listed in Table 2; the values slightly differ from the data in Table 1. Two causes for the different results are probable. One is that the single fatty acids supplied contain a certain amount of impurities, and the other is experimental error [36].

3.4. FTIR Analysis of CA-MA PCM. FTIR spectroscopy was conducted to ascertain the chemical structure of the CA-MA PCM. The FTIR spectra of the single fatty acid CA and MA and the CA-MA mixture are shown in Figure 4.

The infrared spectrum curves of CA and MA in Figure 4 show a strong peak at 1696.66 cm^{-1} (CA) and 1700.45 cm^{-1} (MA), which is the absorption of C=O stretching vibration in the hydroxyl group; this absorption peak is highly typical for fatty acids. Fatty acids usually exist in the form of bimolecular associations due to the presence of hydrogen bonds, and its O–H stretching vibration at 3100–2500 cm^{-1} usually overlaps with the C–H bond stretching vibration peak of the aliphatic group. In this characteristic band, the stretching vibration peak corresponds to $-CH_3$ at 2916.16 cm^{-1} (CA) and 2914.45 cm^{-1} (MA), which correspond to $-CH_2-$ at 2844.53 cm^{-1} (CA) and 2847.70 cm^{-1} (MA).

The infrared spectrum curve of the CA-MA in Figure 4 shows that 1708.79 cm^{-1} is the characteristic peak of C=O of the CA-MA eutectic mixtures, thereby indicating that fatty acid molecules still exist in the form of a dimer in the binary eutectic CA-MA. Furthermore, the absorption peak of the –OH group is in the range of 3050–2800 cm^{-1}. The infrared spectrum of the binary eutectic mixture is similar to the pure fatty acids; thus, its molecular structure has not changed and the phase change heat storage properties and chemical properties of the fatty acids are maintained.

3.5. Thermal Stability of CA-MA PCM. Thermal stability refers to the resistance of PCMs to high temperatures. Thus, whether a significant mass loss occurs in the temperature range in which the PCM was used can be determined. Generally, PCMs, especially organic PCMs, often undergo significant mass loss because of oxidation, decomposition, and volatilization reactions when subjected to high-temperature tests. Therefore, the temperature range must be controlled when using those materials. The thermal stability of fatty acid PCMs is commonly analyzed via TGA.

As shown by the thermal gravimetric (TG) and DTG curves of the CA-MA PCM in Figure 5, its initial mass loss temperature is approximately 110°C, which indicates that the CA-MA eutectic mixture begins to evaporate slowly, the epitaxial starting temperature is 181.84°C, and the temperature range of 120°C–230°C is the main mass loss area. The mass loss is caused by the volatilization of the samples. The temperature of the maximum mass loss rate is 217.61°C. At 243°C, the weight loss of the samples is nearly 98.5%, and the samples have almost completely evaporated; the remaining components are impurities in the system. On the basis of the analysis, the CA-MA eutectic mixture has high thermal stability below 100°C; however, when the working temperature rises above this temperature, the CA-MA eutectic mixture easily decomposes and volatilizes, thereby resulting in high mass loss. The thermal energy storage performance and the service life of the materials will be greatly affected if mass loss occurs. Therefore, the CA-MA PCM cannot

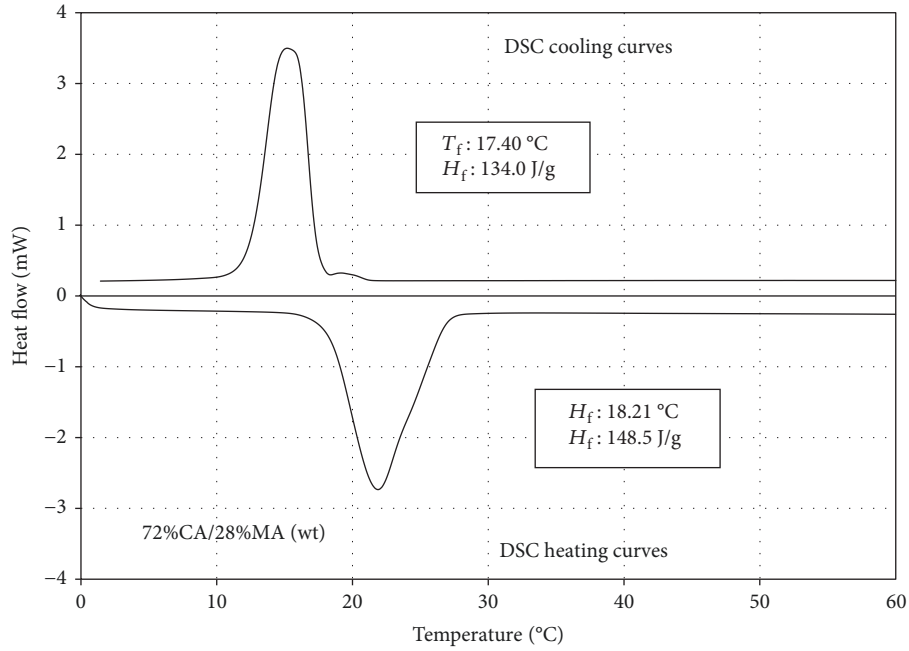

Figure 3: DSC curve of the CA-MA binary eutectic mixture.

Table 2: Thermal properties of CA-MA mixtures in this study and other references.

PCM	Phase change temperature (°C)	Phase change latent heat (J/g)	References
CA/MA mixture (75.0/25.0 wt%)	22.17	153.19	Sarı et al. [29]
CA/MA mixture (76.0/24.0 wt%)	23.64	147.70	Fu et al. [30]
CA/MA mixture (78.0/22.0 wt%)	19.65	149.02	Gao and Qian [31]
CA/MA mixture (73.0/27.0 wt%)	21.70	168.37	Karaipekli et al. [32]
CA/MA mixture (72.0/28.0 wt%)	18.21	148.50	This study

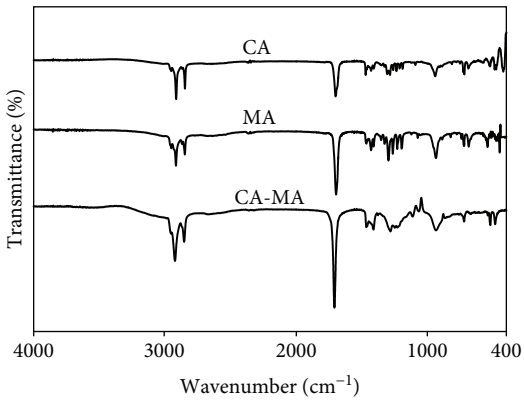

Figure 4: FTIR spectra of CA, MA, and CA-MA.

be used in medium–high-temperature phase change thermal energy storage, although it can be applied for low-temperature phase change thermal energy storage, such as a building energy conservation system and backfill material around the buried pipe of the GSHP system.

3.6. Thermal Reliability of CA-MA PCM. The thermal cycle reliability of PCMs refers to whether the thermal energy storage performance decays after repeated storage/discharge processes. The reliability is an important parameter to measure the service life of PCMs. The thermal cycle reliability of PCMs is often tested by accelerated thermal cycling to study the changes of two important thermodynamic parameters, phase change temperature, and latent heat, before and after thermal cycling. The DSC curves of the CA-MA PCMs after 500, 1000, and 2000 thermal cycles are shown in Figure 6.

The changes in melting and freezing temperatures of the CA-MA PCM with the thermal cycling number are shown in Figure 7. After 500, 1000, and 2000 thermal cycles, the T_m values change to 0.07°C, 1.21°C, and 0.46°C, respectively, and the T_f values change to −0.75°C, −0.52°C, and− 0.87°C, respectively. As the thermal cycling number increases, the variations of the T_m and T_f values are irregular and the change values are extremely small, such that the influence on the phase change energy storage system is negligible. Therefore, on the basis of the changes in the melting and freezing temperatures, the CA-MA PCM has high thermal cycle reliability.

As the thermal cycling number increases, the variations of the melting and freezing latent heat values of the CA-MA PCM are shown in Figure 8. After 500, 1000, and 2000 thermal cycles, the melting latent heat (H_m) values of the

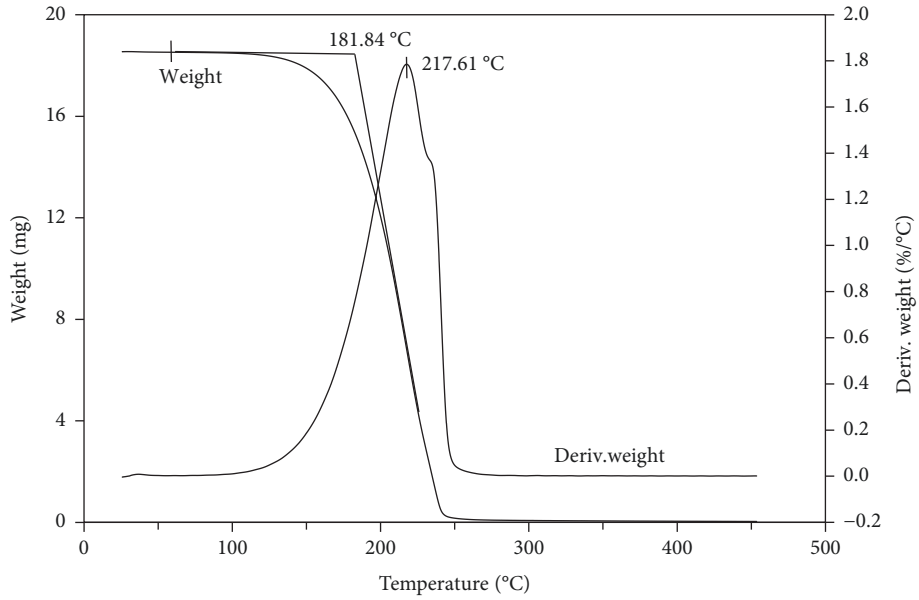

Figure 5: TG and DTG curves of CA-MA PCM.

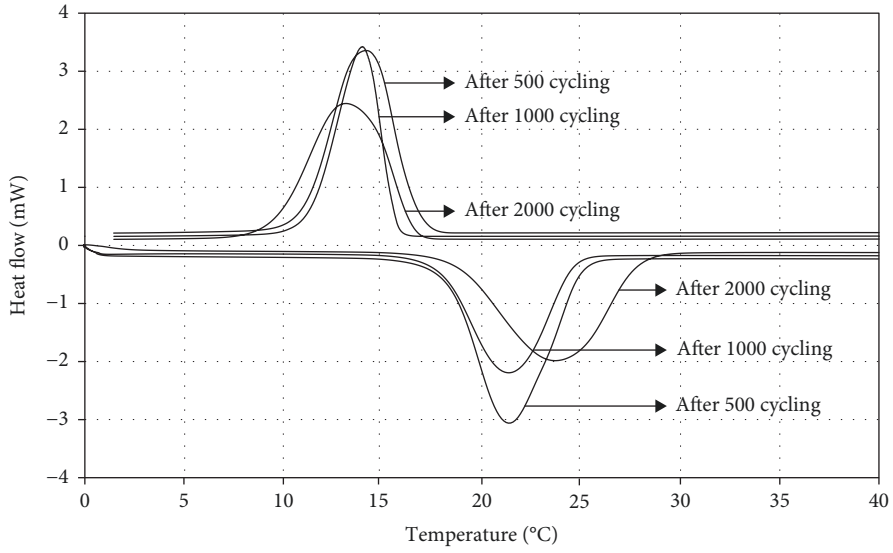

Figure 6: DSC curves of CA-MA PCM after 500, 1000, and 2000 thermal cycles.

mixtures changed by −3.2%, 1.15%, and− 12.1%, respectively, and the freezing latent heat (H_f) values changed by 3.7%, 0.5%, and− 4.4%, respectively. As the number of thermal cycling increases, the variations of H_m and H_f values are irregular. When the number of thermal cycling increases from 500 to 4000, the values of H_m and H_f vary between −12.1% and 3.7%, respectively. These results are acceptable for PCMs applied to LHTES and GSHP systems.

As shown in Figures 7 and 8, small variations of the thermal properties of the PCMs occur before and after thermal cycling, which are caused by the following two factors: one is that the single fatty acids supplied contain a certain amount of impurities, and the other is that the PCMs may undergo chemical degradation [36]. The uncycled and cycled (after 2000 times) samples of CA/MA eutectic mixtures were

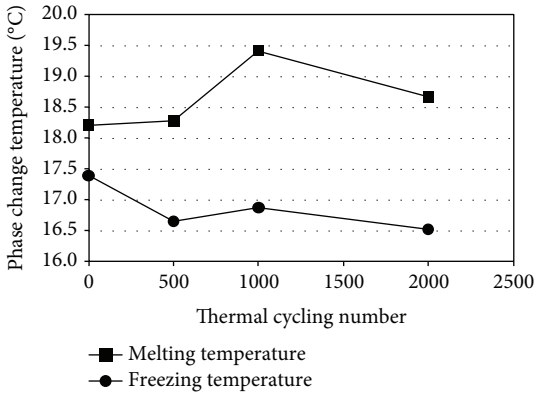

Figure 7: Variations of the phase change temperatures of the CA-MA PCM with the thermal cycling number.

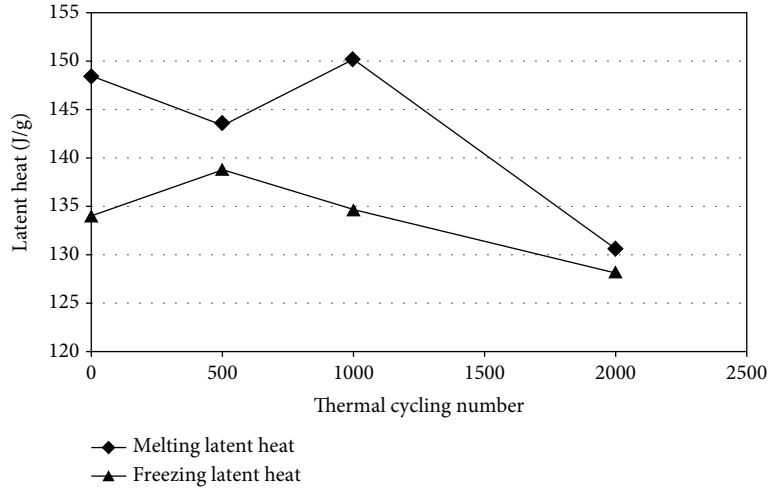

Figure 8: Changes in the latent heat of CA-MA PCM with the thermal cycling number.

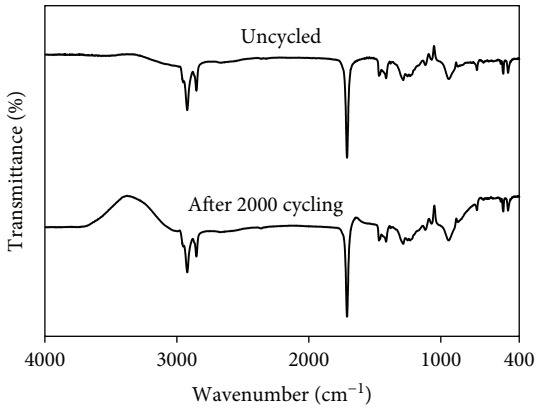

Figure 9: FTIR spectra of the uncycled and cycled CA-MA PCMs.

measured by FTIR for the second factor, and the infrared spectrum is shown in Figure 9. The figure shows that the peaks of the two spectra are in the same frequency band and match each other. Thus, the mixtures do not undergo any chemical degradation after thermal cycling. Thus, as the thermal cycling number increases, the thermal properties of the materials change only because the supplied single fatty acids contain a certain amount of impurities.

4. Conclusion

The CA-MA binary eutectic mixture PCM was prepared. The thermal properties, thermal stability, and long-term cycling reliability of the binary eutectic mixtures were studied.

(1) The DSC results show that the CA-MA PCM is highly suitable for LHTES and as backfill materials around the buried pipe for GSHP systems because of the phase change temperatures (T_m: 18.21°C, T_f: 17.40°C) and latent heat (H_m: 148.5 J/g, H_f: 134.0 J/g)

(2) The TGA results show that the CA-MA PCM has excellent thermal stability below 100°C. Thermal cycling tests show that the CA-MA PCM has good long-term cycling thermal reliability because of the small variations of phase change temperatures and latent heat with thermal cycling number

(3) The FTIR results indicate that the molecular structure of the CA-MA binary eutectic mixture has not changed; the phase change heat storage performance and chemical properties of fatty acid are maintained. In addition, the CA-MA PCM does not undergo any chemical degradation after thermal cycling, and its thermal property changes only because the single fatty acids supplied contain a certain amount of impurities

The CA-MA PCM has promising application prospects in LHTES and as backfill materials around the buried pipe of GSHP systems due to its good performance.

Data Availability

The data availability of the manuscript can be found at https://figshare.com/s/5d017c6ae301c9bdffd9.

Conflicts of Interest

The authors declare that there are no conflicts of interest.

Acknowledgments

This study is supported by the National Natural Science Foundation of China (Project No. 51776226), Natural Science Foundation of Hunan Province (Grant No. 2018JJ2366), Scientific Research Fund of Hunan Provincial Education Department (Grant No. 18K097), and Key R&D Project of Hunan Province (Grant No. 2018GK2074).

References

[1] F. Souayfane, F. Fardoun, and P.-H. Biwole, "Phase change materials (PCM) for cooling applications in buildings: a review," *Energy and buildings.*, vol. 129, pp. 396–431, 2016.

[2] A. Sarı, C. Alkan, and A. Karaipekli, "Preparation, characterization and thermal properties of PMMA/n-heptadecane microcapsules as novel solid–liquid microPCM for thermal energy storage," *Applied Energy.*, vol. 87, no. 5, pp. 1529–1534, 2010.

[3] A. Jamekhorshid, S. M. Sadrameli, and M. Farid, "A review of microencapsulation methods of phase change materials (PCMs) as a thermal energy storage (TES) medium," *Renewable and Sustainable Energy Reviews.*, vol. 31, pp. 531–542, 2014.

[4] G. Li, Y. Hwang, and R. Radermacher, "Review of cold storage materials for air conditioning application," *International journal of refrigeration.*, vol. 35, no. 8, pp. 2053–2077, 2012.

[5] J. P. da Cunha and P. Eames, "Thermal energy storage for low and medium temperature applications using phase change materials–a review," *Applied Energy.*, vol. 177, pp. 227–238, 2016.

[6] A. Horibe, H. Jang, N. Haruki, Y. Sano, H. Kanbara, and K. Takahashi, "Melting and solidification heat transfer characteristics of phase change material in a latent heat storage vessel: Effect of perforated partition plate," *International Journal of Heat and Mass Transfer*, vol. 82, no. 82, pp. 259–266, 2015.

[7] O. Chung, S. G. Jeong, and S. Kim, "Preparation of energy efficient paraffinic PCMs/expanded vermiculite and perlite composites for energy saving in buildings," *Solar Energy Materials and Solar Cells*, vol. 137, pp. 107–112, 2015.

[8] N. Şahan and H. Paksoy, "Investigating thermal properties of using nano-tubular ZnO powder in paraffin as phase change material composite for thermal energy storage," *Composites Part B: Engineering.*, vol. 126, pp. 88–93, 2017.

[9] A. Trigui, M. Karkri, C. Boudaya, Y. Candau, and L. Ibos, "Development and characterization of composite phase change material: thermal conductivity and latent heat thermal energy storage," *Composites Part B: Engineering.*, vol. 49, pp. 22–35, 2013.

[10] M. M. Kenisarin and K. M. Kenisarina, "Form-stable phase change materials for thermal energy storage," *Renewable and Sustainable Energy Reviews*, vol. 16, no. 4, pp. 1999–2040, 2012.

[11] B. Tang, L. Wang, Y. Xu, J. Xiu, and S. Zhang, "Hexadecanol/-phase change polyurethane composite as form-stable phase change material for thermal energy storage," *Solar Energy Materials & Solar Cells.*, vol. 144, pp. 1–6, 2016.

[12] S. Pincemin, R. Olives, X. Py, and M. Christ, "Highly conductive composites made of phase change materials and graphite for thermal storage," *Solar Energy Materials & Solar Cells.*, vol. 92, no. 6, pp. 603–613, 2008.

[13] S. Tahan Latibari, M. Mehrali, M. Mehrali, T. M. I. Mahlia, and H. S. C. Metselaar, "Fabrication and performances of microencapsulated palmitic acid with enhanced thermal properties," *Energy & Fuels*, vol. 29, no. 2, pp. 1010–1018, 2015.

[14] H. Akeiber, P. Nejat, M. Z. A. Majid et al., "A review on phase change material (PCM) for sustainable passive cooling in building envelopes," *Renewable and Sustainable Energy Reviews*, vol. 60, pp. 1470–1497, 2016.

[15] N. Sun and Z. Xiao, "Synthesis and Performances of Phase Change Materials Microcapsules with a Polymer/BN/TiO2-Hybrid Shell for Thermal Energy Storage," *Energy & Fuels*, vol. 31, no. 9, pp. 10186–10195, 2017.

[16] Y. Yuan, N. Zhang, W. Tao, X. Cao, and Y. He, "Fatty acids as phase change materials: A review," *Renewable and Sustainable Energy Reviews*, vol. 29, no. 7, pp. 482–498, 2014.

[17] H. Fauzi, H. S. C. Metselaar, T. M. I. Mahlia, and M. Silakhori, "Sodium laurate enhancements the thermal properties and thermal conductivity of eutectic fatty acid as phase change material (PCM)," *Solar Energy.*, vol. 102, no. 4, pp. 333–337, 2014.

[18] H. He, Q. Yue, B. Gao, X. Zhang, Q. Li, and Y. Wang, "The effects of compounding conditions on the properties of fatty acids eutectic mixtures as phase change materials," *Energy Conversion & Management.*, vol. 69, no. 5, pp. 116–121, 2013.

[19] L. Wang and D. Meng, "Fatty acid eutectic/polymethyl methacrylate composite as form-stable phase change material for thermal energy storage," *Applied Energy.*, vol. 87, no. 8, pp. 2660–2665, 2010.

[20] S. Keleş, K. Kaygusuz, and A. Sari, "Lauric and myristic acids eutectic mixture as phase change material for low-temperature heating applications," *International Journal of Energy Research.*, vol. 29, no. 9, pp. 857–870, 2005.

[21] K. Biswas, Y. Shukla, A. Desjarlais, and R. Rawal, "Thermal characterization of full-scale PCM products and numerical simulations, including hysteresis, to evaluate energy impacts in an envelope application," *Applied Thermal Engineering.*, vol. 138, pp. 501–512, 2018.

[22] S. I. Golestaneh, G. Karimi, A. Babapoor, and F. Torabi, "Thermal performance of co-electrospun fatty acid nanofiber composites in the presence of nanoparticles," *Applied Energy*, vol. 212, pp. 552–564, 2018.

[23] A. Sarı, H. Sarı, and A. Önal, "Thermal properties and thermal reliability of eutectic mixtures of some fatty acids as latent heat storage materials," *Energy Conversion & Management.*, vol. 45, no. 3, pp. 365–376, 2004.

[24] A. Sarı, "Eutectic mixtures of some fatty acids for low temperature solar heating applications: thermal properties and thermal reliability," *Applied Thermal Engineering.*, vol. 25, no. 14-15, pp. 2100–2107, 2005.

[25] R. Wen, X. Zhang, Z. Huang et al., "Preparation and thermal properties of fatty acid/diatomite form-stable composite phase change material for thermal energy storage," *Solar Energy Materials and Solar Cells*, vol. 178, pp. 273–279, 2018.

[26] Y. Yuan, T. Li, N. Zhang, X. Cao, and X. Yang, "Investigation on thermal properties of capric–palmitic–stearic acid/activated carbon composite phase change materials for high-temperature cooling application," *Journal of Thermal Analysis and Calorimetry.*, vol. 124, no. 2, pp. 881–888, 2016.

[27] H. Wei, X. Xie, X. Li, and X. Lin, "Preparation and characterization of capric-myristic-stearic acid eutectic mixture/modified expanded vermiculite composite as a formstable phase change material," *Applied Energy.*, vol. 178, pp. 616–623, 2016.

[28] W. Ju, "Performance simulation and analysis of ground-source heat pump air-conditioning system," *Journal of nanchang university(engineering & technology).*, vol. 33, no. 2, pp. 185–189, 2011, in Chinese.

[29] A. Sarı, A. Bicer, A. Karaipekli, and F. A. Al-Sulaiman, "Preparation, characterization and thermal regulation performance of cement based-composite phase change material," *Solar Energy Materials & Solar Cells.*, vol. 174, pp. 523–529, 2018.

[30] L. J. Fu, F. Q. Dong, P. He, and Y. S. Yang, "Study on preparation and properties of capric-myristic acid/diatomite form-stable phase change energy storage materials," *Journal of Functional Materials.*, vol. 44, no. 10, pp. 1465–1468, 2013.

[31] G. B. Gao and C. X. Qian, "Phase transition capability of the binary system capric acid-myristic acid," *Chemical Journal of*

Chinese Universities-Chinese., vol. 30, no. 8, pp. 1658–1661, 2009.

[32] A. Karaipekli, A. Sari, and K. Kaygusuz, "Thermal properties and long-term reliability of capric acid/lauric acid and capric acid/myristic acid mixtures for thermal energy storage," *Energy Sources*, vol. 30, no. 13, pp. 1248–1258, 2008.

[33] M. N. R. Dimaano and T. Watanabe, "Performance investigation of the capric and lauric acid mixture as latent heat energy storage for a cooling system," *Solar Energy.*, vol. 72, no. 3, pp. 205–215, 2002.

[34] S. Jianli, L. Qiaoming, W. Zhengjun, and Z. Peng, "Preparation and study on phase-change energy storage materials," *New chemical materials.*, vol. 38, no. 6, pp. 92–94, 2010, in Chinese.

[35] Y. Zhang, S. Y, and X. Ge, "Prediction of the melting temperature and the fusion heat of (quasi-)eutectic PCM," *Journal of China University of science and Technology.*, vol. 25, no. 4, pp. 474–478, 1995.

[36] A. Karaipekli, A. Sarı, and K. Kaygusuz, "Thermal properties and thermal reliability of capric acid/stearic acid mixture for latent heat thermal energy storage," *Energy Sources*, vol. 31, no. 3, pp. 199–207, 2009.

Hindawi
Journal of Nanomaterials
Volume 2019, Article ID 2820962, 7 pages
https://doi.org/10.1155/2019/2820962

Research Article

Electrochemical Epitaxial Growth of TiO_2/CdS/PbS Nanocables

Peng Wang,[1,2] Zhongyang Zhang,[3] Hua Wang,[4] Tieqiang Zhang,[3] Haining Cui,[3] Yue Yang,[1] and William W. Yu[1,4]

[1]*State Key Laboratory on Integrated Optoelectronics, College of Electronic Science and Engineering, Jilin University, Changchun 130012, China*
[2]*College of Materials Science and Engineering, Beijing University of Technology, Beijing 100124, China*
[3]*State Key Laboratory of Superhard Materials, College of Physics, Jilin University, Changchun 130012, China*
[4]*Department of Chemistry and Physics, Louisiana State University, Shreveport, LA 71115, USA*

Correspondence should be addressed to Yue Yang; yangyue@jlu.edu.cn and William W. Yu; wyu6000@gmail.com

Received 7 February 2019; Accepted 3 April 2019; Published 30 April 2019

Guest Editor: Jamal Siddiqui

Electrochemical deposition as a liquid phase epitaxial growth method is widely used to fabricate different kinds of hierarchical structures. As a typical heterostructure, TiO_2/PbS is widely utilized in the areas of photovoltaics and photocatalysis. Oriented TiO_2 nanorod (NR) arrays can provide direct pathways for the electron transport of photoanode. However, the lattice mismatch between TiO_2 NR sides and PbS is very large; PbS nanoparticles (NPs) only formed on the top of TiO_2 NRs. To solve this problem, TiO_2/CdS core/shell nanocables were firstly prepared electrochemically because the lattice ratio between TiO_2 and CdS was 0.916; and then, PbS NPs were successfully deposited over CdS shells (the lattice ratio between CdS and PbS was 0.697) to form TiO_2/CdS/PbS hierarchical heterostructures. Experimental results demonstrated that the CdS interlayer could effectively promote the growth of PbS NPs on the surface and improve the fill factor and short current density of the photoanodes.

1. Introduction

Various heterostructures have been utilized in the areas of photovoltaics [1–5] and photocatalysis [6, 7], such as CdS [8, 9], CdSe [10, 11], CdTe [12], PbS [2, 13], PbSe [14–18], and AgSe [19] over the surface of TiO_2 [20–22] and ZnO [23–25], with different morphologies such as multilayered films, core/shell nanocables, and spherical dots. Several different chemical methods, including electrochemistry [12, 26, 27], chemical bath deposition (CBD) [28, 29], assembly of quantum dots (QDs) by immobilization via organic linkers [30], and successive ionic layer adsorption and reaction (SILAR) [31, 32], are commonly used to fabricate these heterostructures. Among them, electrochemistry as a liquid-phase epitaxial growth method is easy to fabricate large-area devices with facile and labor-saving superiorities, particularly on nanorod (NR) arrays.

As one of these typical heterostructures, the TiO_2/PbS heterostructure has already been widely studied. Chen and coworkers used bath deposition to fabricate a TiO_2/PbS counter electrode for QD-sensitized solar cells [33]. Mali et al. fabricated solar cells via SILAR [34]. Sargent's group utilized colloidal PbS QDs to form heterostructure solar cells [35, 36]. But the separation of the photocarriers in these structures often does not do well due to the low lattice ratio.

Here, we tried to electrically deposit PbS over TiO_2 NR arrays which could provide direct pathways for photoelectron transporting from the points of injection at the interfaces of the heterostructures between the two different materials to the transparent conducting oxide (TCO) electrodes. However, we found that PbS nanoparticles (NPs) were only grown on top of the TiO_2 NRs due to the low lattice ratio between the sides of TiO_2 NR and PbS (about 0.495), so fully covered TiO_2/PbS heterostructures were not realized. CdS/PbS heterostructures are also widely used in the area of photovoltaics [37, 38]. In this work, we coated a layer of CdS over TiO_2 NRs by electrochemistry because the lattice ratio between TiO_2 nanorod and CdS is only 0.916. Then, PbS QDs were deposited on the surfaces of core/shell TiO_2/CdS nanocables to form TiO_2/CdS/PbS

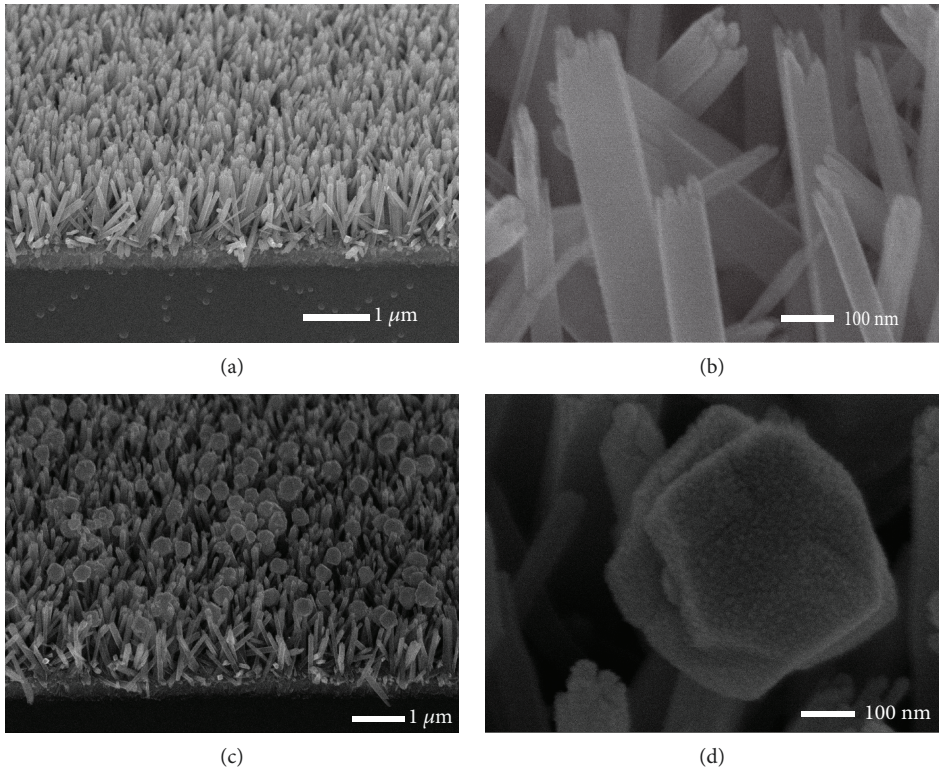

Figure 1: (a, b) SEM images of TiO_2 NR arrays. (c) SEM images of TiO_2/PbS deposited by electrochemistry for 20 min. (d) SEM images of the top of TiO_2/PbS.

heterostructures (the lattice ratio between CdS and PbS is 0.697). Due to the existence of the CdS interlayer, the fill factor and short current density of the photoanodes were greatly improved.

2. Experimental

2.1. Preparation of TiO_2 NR Arrays. TiO_2 NR arrays were fabricated through a hydrothermal synthesis [27, 39]. After mixing deionized water and concentrated hydrochloric acid (mass fraction 36.5-38%) of 60 mL each, 2 mL of titanium butoxide was added drop by drop into the solution under vigorous stirring at room temperature. A half hour later, 30 mL of the prepared precursor solution was transferred into a 100 mL stainless steel autoclave with a Teflon liner. And then, three pieces of FTO substrates which had been ultrasonically cleaned by a mixed solution (chloroform, acetone, and 2-propanol with a volume ratio of 1 : 1 : 1) for 60 min were placed with an angle against the wall (the conductive sides faced down) in the Teflon liner. The hydrothermal synthesis took place at 140°C for 14 h. When the autoclave was cooled to room temperature, the substrates were taken out, rinsed with deionized water, and dried in an oven at 150°C.

2.2. Preparation of TiO_2/PbS Heterostructures. The preparation of the TiO_2/PbS heterostructure was carried out by electrodeposition with a three-electrode system. A Pt sheet, a standard Ag/AgCl electrode, and the TiO_2 NR arrays on FTO (4.5 cm^2 working area) were used as the counter electrode, the reference electrode, and the working electrode, respectively. An electrolyte containing 0.1 M of $Pb(NO_3)_2$ and 0.1 M of thiourea in dimethyl sulphoxide (DMSO)/water (a volume ratio of 1 : 1) was kept at 90°C. After depositions from 2 to 30 min with a constant voltage of 0.5 V, the samples were taken out and washed with deionized water and ethanol, respectively.

2.3. Preparation of TiO_2/CdS Heterostructures. The preparation of the TiO_2/CdS heterostructure was carried out by electrodeposition with the same three-electrode system stated above. An electrolyte containing 0.2 M of $Cd(NO_3)_2$ and 0.2 M of thiourea in dimethyl sulphoxide (DMSO)/water (volume ratio of 1 : 1) was kept at 90°C. After depositions from 2 to 30 min with a constant voltage of 0.66 V, the samples were taken out and washed with deionized water and ethanol, respectively.

2.4. Preparation of TiO_2/CdS/PbS Heterostructures. The preparation of the TiO_2/PbS/CdS heterostructure was formed in two steps. (1) Following Section 2.3, the TiO_2/CdS heterostructure was firstly fabricated. (2) Following Section 2.2, PbS QDs were deposited over TiO_2/CdS nanocables.

2.5. Characterizations. Field emission scanning electron microscopy (FESEM, JEOL JSM-6700) was used to examine the microstructures of the samples. Transmission electron microscope (TEM) and high-resolution TEM (HRTEM) images of TiO_2/CdS heterostructures were taken by a JEM-2100F high-resolution transmission microscope. The absorption characterizations of all samples were measured

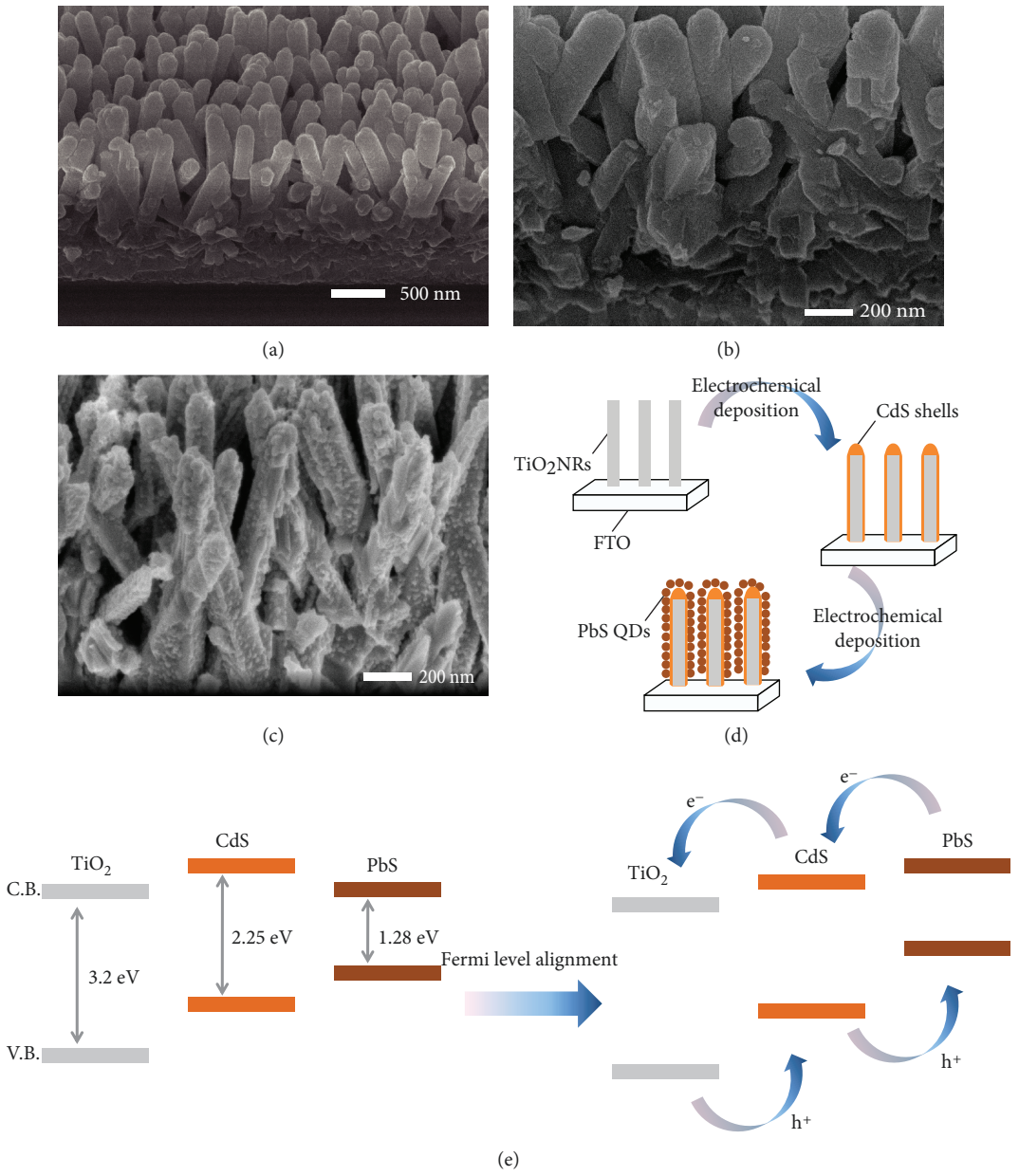

FIGURE 2: (a, b) SEM images of TiO_2/CdS nanocable arrays. (c) SEM image of TiO_2/CdS/Pb. (d) Schematic diagram of the growth process of the TiO_2/CdS/PbS heterostructures. (e) Relative band edges of TiO_2, CdS, and PbS (left) and the proposed band edges of TiO_2/CdS/PbS termed by Fermi level alignment (right).

with a UV-3150 spectrophotometer. A Rigaku D/max-2500 X-ray diffractometer (XRD) with Cu Kα radiation ($\lambda = 0.15418$ nm) was used at room temperature to analyze the crystal structures of TiO_2 and CdS. With an electrochemical workstation (Corrtest CS150), photoelectrochemical properties were tested under the three-electrode system where the samples, Pt sheet, and Ag/AgCl electrode worked as the working electrode, counter electrode, and reference electrode, respectively, in a polysulfide redox couple (S^{2-}/SO_3^{2-}) electrolyte (0.25 M Na_2S and 0.35 M Na_2SO_3 in deionized water), while a Zolix SS150 Solar Simulator was used as the illumination source with a power of 100 mW/cm^2.

3. Results and Discussion

3.1. TiO_2/PbS Heterostructures. Vertical TiO_2 NR arrays fabricated on FTO by hydrothermal synthesis are shown in Figure 1(a). The TiO_2 NRs grew orderly with a quadrangular prism morphology indicating well-crystallized structures. Their sides were very neat and smooth, which were different from their rugged tops (Figure 1(b)). Therefore, there were a lot of lattice defects at the tops. These NRs were about 2 μm long, and we could count that the planar density was 8-12 NRs per μm^2.

With these as-prepared TiO_2 NRs, PbS was deposited electrochemically, and the SEM images show the morphologies of

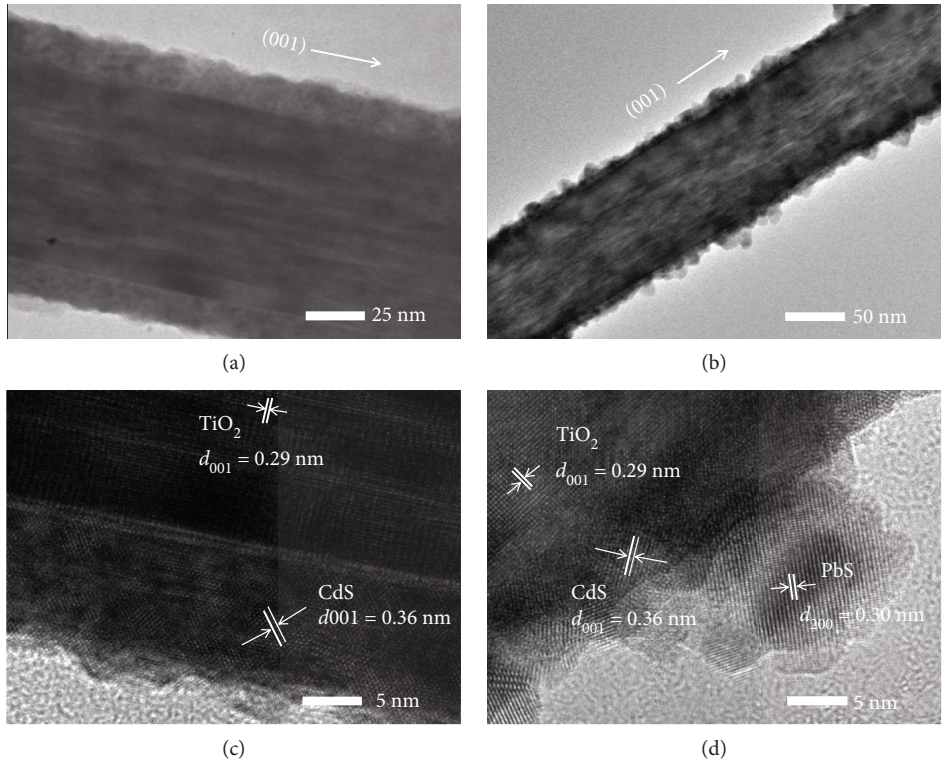

Figure 3: (a) TEM image of a TiO_2 NR coated with a CdS shell. (b) TEM image of TiO_2/CdS/PbS. (c) HRTEM image shows the interface and crystalline structure of TiO_2/CdS. (d) HRTEM image shows the interface and crystalline structure of TiO_2/CdS/PbS.

samples deposited for 20 min (Figures 1(c) and 1(d)). In Figure 1(c), it is clear to see that the quadrangular prism NRs were covered by PbS NPs (diameter around 300 nm) which were obviously distinguished in the SEM image over the top of the TiO_2 NRs.

3.2. TiO_2/CdS/PbS Heterostructures. The CdS/PbS heterostructure has already been widely used in the areas of photovoltaic and photocatalysis. Here, we would insert a CdS layer between TiO_2 and PbS to fabricate TiO_2/CdS/PbS heterostructures for our photoanodes.

With the as-prepared TiO_2 NRs, CdS was firstly deposited by the electrochemical method. Figures 2(a) and 2(b) show the morphologies of samples deposited with CdS for 30 min. The morphologies of the NRs changed from quadrangular prisms to cylinders whose diameters became ~50 nm larger, and the surface was no longer smooth. In Figure 2(b), it is clear to see that the quadrangular prism NRs were covered by CdS shells which were easily distinguished in the SEM image. Comparing with the smooth sides of TiO_2 NRs, there were more defect centers which could be good for the epitaxial growth.

Furthermore, we deposited PbS over the prepared TiO_2/CdS nanocables at the same conditions. In Figure 2(c), the SEM image shows the morphology of the sample deposited with CdS for 10 min and PbS for 10 min. It is clear to see that there are dense PbS QDs adhered all over the TiO_2/CdS nanocables. Through these observations, the growth process is summarized in Figure 2(d). CdS grew over the surface of TiO_2 NRs, and the core/shell TiO_2/CdS structures were formed. The relative band edges of TiO_2, CdS, and PbS are shown in Figure 2(e) with their band gaps, respectively, to be 3.20, 2.25, and 1.28 eV. When the TiO_2/CdS/PbS heterostructure is formed, their band edges at the interfaces would be termed by Fermi level alignment shown in the right part of Figure 2(e).

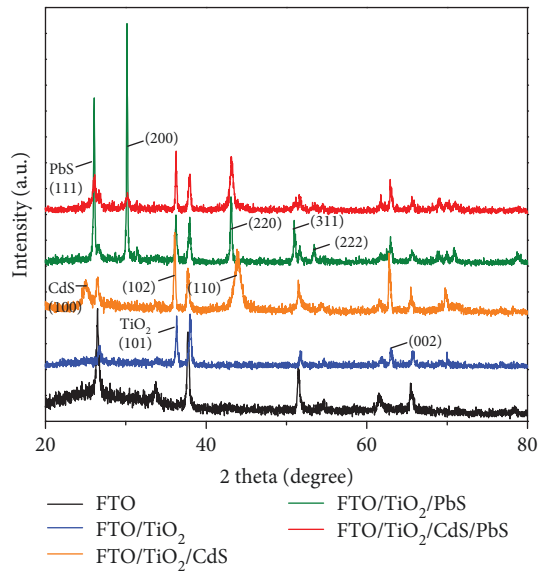

Figure 4: XRD patterns of FTO (black line), TiO_2 NRs (blue line), TiO_2/CdS (orange line), TiO_2/PbS (green line), and TiO_2/CdS/PbS (red line).

The core/shell rod structure (nanocable) could also be seen from the TEM image with CdS deposited for 15 min (Figure 3(a)), while in the HRTEM image (Figure 3(c)) it is easy to distinguish the interface between TiO_2 core and CdS shell and the d spacings of TiO_2 (001) and CdS (100) were 0.29 nm and 0.36 nm, respectively. In Figure 3(b), it shows the TEM image of TiO_2/CdS/PbS QDs deposited with CdS for 10 min and PbS for 10 min. Except the d spacings of TiO_2 (001) and CdS (100), the d spacing of PbS (200) is shown to be 0.30 nm (Figure 3(d)).

3.3. Phase Composition and Structure. In Figure 4, there are two new peaks of the XRD pattern of TiO_2 NRs (blue line) compared with the pattern of FTO (black line), and the two peaks, respectively, correspond to the different planes of tetragonal phase rutile TiO_2 (JCPDS 88-1175) exhibited as quadrangular prisms in the SEM images. The two predominant peaks at 36.4° and 63.2°, respectively, indexed to the (101) and (002) planes suggesting that the growth of the TiO_2 NRs took place along their c-axis on the FTO substrate proved in Figure 1(a). When CdS was electrochemically deposited (shell), two new diffraction peaks (orange line) appeared at 24.84° and 43.74° which, respectively, indexed to the (100) and (110) planes of the hexagonal CdS (JCPDS 77-2306). Meanwhile, the intensity of the peak around 36° was higher, because this peak was not only from the (101) plane of the tetragonal TiO_2 but also from the (102) plane of the hexagonal CdS. When PbS was deposited (nanoparticle), there were several new diffraction peaks (green line) that appeared at 25.96°, 30.07°, 43.06°, 50.76°, and 53.41° which, respectively, indexed to the (111), (200), (220), (311), and (222) planes of the galena PbS (JCPDS 05-0592). The red line represents the XRD pattern of the TiO_2/CdS/PbS heterostructure, and the typical peaks of all components could be found.

3.4. Morphologies Controlled by the Lattice Ratio. From the SEM and TEM images, TiO_2 NRs grew along the [001] direction. The lattice constants of the TiO_2 NRs (JCPDS 88-1175) and PbS NPs (JCPDS 05-0592) shown in Table 1 are, respectively, $a = b = 0.4517$ nm, $c = 0.294$ nm, and $a = b = c = 0.5936$ nm. At the sides of the TiO_2 NRs, the lattice ratio between TiO_2 ($c = 0.294$ nm) and PbS ($a = b = c = 0.5936$ nm) is 0.495. At the top of TiO_2 NRs, the lattice ratio between TiO_2 ($a = b = 0.4517$ nm) and PbS ($a = b = c = 0.5936$ nm) is 0.761. Therefore, PbS NPs were deposited on the top of TiO_2 NRs.

Proved from the XRD pattern, the lattice constants of the CdS (JCPDS 77-2306) shown in Table 1 are $a = b = 0.4136$ nm, $c = 0.6713$ nm. The lattice ratio between TiO_2 ($a = 0.4517$ nm) and CdS ($a = b = 0.4136$ nm) is 0.916. Because of the high lattice ratio, CdS could be deposited all over the TiO_2 nanorods and the core/shell TiO_2/CdS nanocables were therefore formed. The lattice ratio between CdS ($a = b = 0.4136$ nm) and PbS ($a = b = c = 0.5936$ nm) is 0.697, so PbS could easily deposit on CdS.

3.5. UV-Vis Absorption. The UV-Vis absorption spectra of all samples with different treatments are shown in Figure 5.

Table 1: Lattice constants of TiO_2, CdS, and PbS.

Lattice constant	a (nm)	b (nm)	c (nm)
TiO_2	0.4517	0.4517	0.294
CdS	0.4163	0.4163	0.6713
PbS	0.5936	0.5936	0.5936

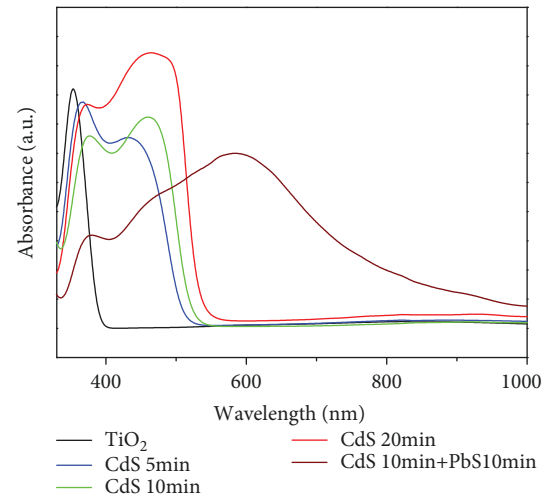

Figure 5: UV-Vis absorption spectra of TiO_2 NRs (black line); TiO_2/CdS deposited with CdS for 5 min (blue line), 10 min (green line), and 20 min (red line); and TiO_2/CdS/PbS deposited with CdS for 10 min and PbS for 10 min (wine line). The electrolyte for CdS contained 0.2 M of $Cd(NO_3)_2$ and 0.2 M of thiourea; the electrolyte or PbS contained 0.1 M of $Cd(NO_3)_2$ and 0.1 M of thiourea.

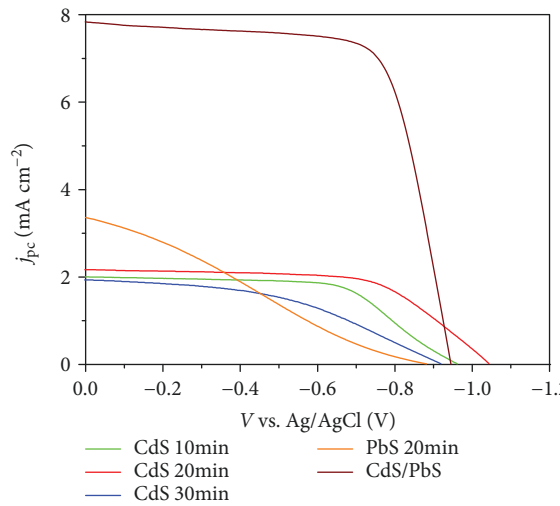

Figure 6: Photocurrent density-output potential difference (J-V) curves of TiO_2/CdS deposited with CdS for 10 min (green line), 20 min (red line), and 30 min (blue line); TiO_2/PbS deposited with PbS for 20 min (orange line); and TiO_2/CdS/PbS deposited with CdS for 20 min and PbS for 20 min (wine line).

Comparing the black line (TiO_2) and the blue line (deposited with CdS for 5 min), it is clear to see that the absorption range was broadened from the UV region to the visible light region

Table 2: Photovoltage characteristics of photoanodes.

Sample	Photocurrent density (mA cm^{-2})	Output potential difference V vs. Ag/AgCl (V)	Fill factor
CdS 10 min	2.04	0.98	0.57
CdS 20 min	2.17	1.03	0.62
CdS 30 min	1.92	0.92	0.42
PbS 10 min	3.36	0.90	0.26
CdS 10 min + PbS 10 min	7.83	0.94	0.63

with CdS over TiO_2 NRs. Comparing the blue line (deposited with CdS for 5 min) to the green (deposited with CdS for 10 min) and red lines (deposited with CdS for 20 min), the absorption ranges of TiO_2/CdS were further broadened with the increase in deposition time (more CdS). When PbS was deposited, the absorption range was extended to the near infrared region shown as the wine line. With a larger area of absorption range, the photoanode could be excited by more photons and a higher short current density would be achieved.

3.6. Photovoltaic Performance of the Electrodes. In Figure 6, it shows the photocurrent density-output potential difference (J-V) curves of the photoanodes fabricated by different conditions. When PbS was deposited over TiO_2 NRs (orange line), the photovoltage characteristics are given in Table 2 with the photocurrent density, output potential difference, and fill factor, respectively, to be 3.36 mA cm^{-2}, 0.90 V, and 0.26. The rather low fill factor was consistent with the SEM images that PbS NPs just grew on the top of TiO_2 NRs and they did not grow on the sides. Shown in Figure 6 and Table 1, the photocurrent density of TiO_2/CdS increased at first and then decreased and the output potential differences had no obvious change with more CdS deposition time. The highest photocurrent density of TiO_2/CdS was 2.17 mA cm^{-2} when CdS was deposited for 20 min. After TiO_2/CdS/PbS formed, the absorption range was broadened and PbS NPs densely covered all over the nanocables. Thus, it is clear to see that the photocurrent density and fill factor were largely increased from 3.36 mA cm^{-2} to 7.83 mA cm^{-2} and from 0.26 to 0.63 (Figure 6 and Table 2).

4. Conclusions

With a suitable lattice distance between PbS and TiO_2, CdS was selected to coat on the surface of TiO_2 nanorods and then PbS QDs were epitaxially grown all over the surface of TiO_2/CdS nanocables to form a TiO_2/CdS/PbS heterostructure. This strategy solves the difficulty to directly grow PbS QDs on TiO_2 NR arrays and makes use of the optoelectronic property of PbS QDs for superior photovoltage characteristics of the TiO_2/CdS/PbS photoanode.

Data Availability

The data used to support the findings of this study are available from the corresponding author upon request.

Conflicts of Interest

There is no conflict of interest.

Acknowledgments

This work was supported by the National Natural Science Foundation of China (51772123 and 11674127), Jilin Province Science Fund for Excellent Young Scholars (20170520129JH), and Board of Regents Support Funds Professorship.

References

[1] G. Wei, S. Wang, K. Renshaw, M. E. Thompson, and S. R. Forrest, "Solution-processed squaraine bulk heterojunction photovoltaic cells," *ACS Nano*, vol. 4, no. 4, pp. 1927–1934, 2010.

[2] D. A. R. Barkhouse, A. G. Pattantyus-Abraham, L. Levina, and E. H. Sargent, "Thiols passivate recombination centers in colloidal quantum dots leading to enhanced photovoltaic device efficiency," *ACS Nano*, vol. 2, no. 11, pp. 2356–2362, 2008.

[3] A. A. Bakulin, S. Neutzner, H. J. Bakker, L. Ottaviani, D. Barakel, and Z. Chen, "Charge trapping dynamics in PbS colloidal quantum dot photovoltaic devices," *ACS Nano*, vol. 7, no. 10, pp. 8771–8779, 2013.

[4] M. T. Rizi and M. H. Shahrokh Abadi, "Numerical investigation on efficiency improvement of double layer antireflection coating AZO/buffer/Cu_2O/CuO on back-surface fluorine-doped tin oxide heterostructure solar cells," *Journal of the Optical Society of America B*, vol. 36, no. 4, pp. 1155–1165, 2019.

[5] S. R. Rosario, I. Kulandaisamy, A. M. S. Arulanantham et al., "Fabrication and characterization of lead sulfide (PbS) thin film based heterostructure (FTO/CdS/PbS/Ag) solar cell by nebulizer spray method," *Materials Research Express*, vol. 6, no. 5, 2019.

[6] S. Kumar, S. Khanchandani, M. Thirumal, and A. K. Ganguli, "Achieving enhanced visible-light-driven photocatalysis using type-II $NaNbO_3$/CdS core/shell heterostructures," *ACS Applied Materials & Interfaces*, vol. 6, no. 15, pp. 13221–13233, 2014.

[7] W. J. Lee, J. M. Lee, S. T. Kochuveedu et al., "Biomineralized N-doped CNT/TiO_2 core/shell nanowires for visible light photocatalysis," *ACS Nano*, vol. 6, no. 1, pp. 935–943, 2012.

[8] D. R. Baker and P. V. Kamat, "Photosensitization of TiO_2 nanostructures with CdS quantum dots: particulate versus tubular support architectures," *Advanced Functional Materials*, vol. 19, no. 5, pp. 805–811, 2009.

[9] N. N. Hewa-Kasakarage, M. Kirsanova, A. Nemchinov et al., "Radiative recombination of spatially extended excitons in (ZnSe/CdS)/CdS heterostructured nanorods," *Journal of the American Chemical Society*, vol. 131, no. 3, pp. 1328–1334, 2009.

[10] P. Brown and P. V. Kamat, "Quantum dot solar cells. Electrophoretic deposition of CdSe–C_{60} composite films and capture of photogenerated electrons with nC_{60} cluster shell," *Journal of*

the American Chemical Society, vol. 130, no. 28, pp. 8890-8891, 2008.

[11] K. S. Leschkies, R. Divakar, J. Basu et al., "Photosensitization of ZnO nanowires with CdSe quantum dots for photovoltaic devices," *Nano Letters*, vol. 7, no. 6, pp. 1793–1798, 2007.

[12] X. Wang, H. Zhu, Y. Xu et al., "Aligned ZnO/CdTe core–shell nanocable arrays on indium tin oxide: synthesis and photoelectrochemical properties," *ACS Nano*, vol. 4, no. 6, pp. 3302–3308, 2010.

[13] R. Plass, S. Pelet, J. Krueger, M. Grätzel, and U. Bach, "Quantum dot sensitization of organic–inorganic hybrid solar cells," *The Journal of Physical Chemistry B*, vol. 106, no. 31, pp. 7578–7580, 2002.

[14] W. Ma, S. L. Swisher, T. Ewers et al., "Photovoltaic performance of ultrasmall PbSe quantum dots," *ACS Nano*, vol. 5, no. 10, pp. 8140–8147, 2011.

[15] X. Zhang, Y. Zhang, L. Yan et al., "High photocurrent PbSe solar cells with thin active layers," *Journal of Materials Chemistry A*, vol. 3, no. 16, pp. 8501–8507, 2015.

[16] X. Zhang, Y. Zhang, L. Yan et al., "PbSe nanocrystal solar cells using bandgap engineering," *RSC Advances*, vol. 5, no. 80, pp. 65569–65574, 2015.

[17] X. Zhang, Y. Zhang, H. Wu et al., "PbSe quantum dot films with enhanced electron mobility employed in hybrid polymer/nanocrystal solar cells," *RSC Advances*, vol. 6, no. 21, pp. 17029–17035, 2016.

[18] H. Wu, X. Zhang, Y. Zhang et al., "Colloidal PbSe solar cells with molybdenum oxide modified graphene anodes," *ACS Applied Materials & Interfaces*, vol. 7, no. 38, pp. 21082–21088, 2015.

[19] C. Ji, Y. Zhang, X. Zhang et al., "Paper synthesis and characterization of $Ag_2S_xSe_{1-x}$ nanocrystals and their photoelectrochemical property," *Nanotechnology*, vol. 28, no. 6, article 065602, 2017.

[20] L. Etgar, T. Moehl, S. Gabriel, S. G. Hickey, A. Eychmüller, and M. Grätzel, "Light energy conversion by mesoscopic PbS quantum dots/TiO_2 heterojunction solar cells," *ACS Nano*, vol. 6, no. 4, pp. 3092–3099, 2012.

[21] J. J. Wu and C. C. Yu, "Aligned TiO_2 nanorods and nanowalls," *The Journal of Physical Chemistry B*, vol. 108, no. 11, pp. 3377–3379, 2004.

[22] D. Kuang, J. Brillet, P. Chen et al., "Application of highly ordered TiO_2 nanotube arrays in flexible dye-sensitized solar cells," *ACS Nano*, vol. 2, no. 6, pp. 1113–1116, 2008.

[23] A. K. Chandiran, M. Abdi-Jalebi, M. K. Nazeeruddin, and M. Grätzel, "Analysis of electron transfer properties of ZnO and TiO_2 photoanodes for dye-sensitized solar cells," *ACS Nano*, vol. 8, no. 3, pp. 2261–2268, 2014.

[24] M. Law, L. E. Greene, A. Radenovic, T. Kuykendall, J. Liphardt, and P. Yang, "ZnO–Al_2O_3 and ZnO–TiO_2 core–shell nanowire dye-sensitized solar cells," *The Journal of Physical Chemistry B*, vol. 110, no. 45, pp. 22652–22663, 2006.

[25] B. Carlson, K. Leschkies, E. S. Aydil, and X.-Y. Zhu, "Valence band alignment at cadmium selenide quantum dot and zinc oxide $(10\bar{1}0)$ interfaces," *The Journal of Physical Chemistry C*, vol. 112, no. 22, pp. 8419–8423, 2008.

[26] X. Y. Yu, J. Y. Liao, K. Q. Qiu, D. B. Kuang, and C. Y. Su, "Dynamic study of highly efficient CdS/CdSe quantum dot-sensitized solar cells fabricated by electrodeposition," *ACS Nano*, vol. 5, no. 12, pp. 9494–9500, 2011.

[27] P. Wang, Y. Zhang, L. Su et al., "Photoelectrochemical properties of CdS/CdSe sensitized TiO_2 nanocable arrays," *Electrochimica Acta*, vol. 165, pp. 110–115, 2015.

[28] C. H. Chang and Y. L. Lee, "Chemical bath deposition of CdS quantum dots onto mesoscopic TiO_2 films for application in quantum-dot-sensitized solar cells," *Applied Physics Letters*, vol. 91, no. 5, article 053503, 2007.

[29] S. Gimenez, T. Lana-Villarreal, R. Gomez, S. Agouram, V. Munoz-Sanjose, and I. Mora-Sero, "Determination of limiting factors of photovoltaic efficiency in quantum dot sensitized solar cells: correlation between cell performance and structural properties," *Journal of Applied Physics*, vol. 108, no. 6, article 064310, 2010.

[30] B. Farrow and P. V. Kamat, "CdSe quantum dot sensitized solar cells. Shuttling electrons through stacked carbon nanocups," *Journal of the American Chemical Society*, vol. 131, no. 31, pp. 11124–11131, 2009.

[31] H. J. Lee, M. Wang, P. Chen et al., "Efficient CdSe quantum dot-sensitized solar cells prepared by an improved successive ionic layer adsorption and reaction process," *Nano Letters*, vol. 9, no. 12, pp. 4221–4227, 2009.

[32] L. J. Diguna, Q. Shen, J. Kobayashi, and T. Toyoda, "High efficiency of CdSe quantum-dot-sensitized TiO_2 inverse opal solar cells," *Applied Physics Letters*, vol. 91, no. 2, article 023116, 2007.

[33] Y. Chen, X. Zhang, Q. Tao et al., "High catalytic activity of a PbS counter electrode prepared via chemical bath deposition for quantum dots-sensitized solar cells," *RSC Advances*, vol. 5, no. 3, pp. 1835–1840, 2015.

[34] S. S. Mali, S. K. Desai, S. S. Kalagi et al., "PbS quantum dot sensitized anatase TiO_2 nanocorals for quantum dot-sensitized solar cell applications," *Dalton Transactions*, vol. 41, no. 20, pp. 6130–6136, 2012.

[35] A. H. Ip, S. M. Thon, S. Hoogland et al., "Hybrid passivated colloidal quantum dot solids," *Nature Nanotechnology*, vol. 7, no. 9, pp. 577–582, 2012.

[36] A. G. Pattantyus-Abraham, I. J. Kramer, A. R. Barkhouse et al., "Depleted-heterojunction colloidal quantum dot solar cells," *ACS Nano*, vol. 4, no. 6, pp. 3374–3380, 2010.

[37] H. J. Lee, H. C. Leventis, S.-J. Moon et al., "PbS and CdS quantum dot-sensitized solid-state solar cells: "old concepts, new results"," *Advanced Functional Materials*, vol. 19, no. 17, pp. 2735–2742, 2009.

[38] J. Hernández-Borja, Y. V. Vorobiev, and R. Ramírez-Bon, "Thin film solar cells of CdS/PbS chemically deposited by an ammonia-free process," *Solar Energy Materials and Solar Cells*, vol. 95, no. 7, pp. 1882–1888, 2011.

[39] B. Liu and E. S. Aydil, "Growth of oriented single-crystalline rutile TiO_2 nanorods on transparent conducting substrates for dye-sensitized solar cells," *Journal of the American Chemical Society*, vol. 131, no. 11, pp. 3985–3990, 2009.

Hindawi
Journal of Nanomaterials
Volume 2019, Article ID 2769519, 8 pages
https://doi.org/10.1155/2019/2769519

Research Article

One-Pot Synthesis of Photoluminescent Self-Assembled Carbon Dot Monolayer Films

Hongchong Guo,[1] Wei Li,[1] Gang Sun,[2] and Bo You [1]

[1]*Department of Materials Science and the Advanced Coatings Research Center of the China Educational Ministry, Fudan University, Shanghai 200433, China*
[2]*Department of Aeronautics and Astronautics, Fudan University, Shanghai 200433, China*

Correspondence should be addressed to Bo You; youbo@fudan.edu.cn

Received 12 December 2018; Revised 25 February 2019; Accepted 26 February 2019; Published 4 April 2019

Guest Editor: Nour F. Attia

We propose a facile and simple synthesis of photoluminescent (PL) carbon dot self-assembled monolayer films (CD-SAMFs) at oil-water interfaces. By using styrene both as the carbon source and the oil phase medium, we got our amazing CD-SAMFs under the copper acetate and hydrogen peroxide ($Cu(Ac)_2$-H_2O_2) catalytic-oxidation system. Without any surface modification, the spontaneously formed CD-SAMFs exhibit ultrathin thickness (<10 nm), bright luminescence, high transparency, and hydrophobicity, which have the potential as a new alternative to be used on multifunctional coating films, anticounterfeiting, displays, sensors, and optical devices.

1. Introduction

The advent of two-dimensional (2D) materials opens up new opportunities and challenges [1]. Most notably, self-assembled monolayers (SAMs) have served as an excellent candidate for the fabrication of technologically important ultrathin film materials for sensors, optical devices, and magnetic storage media [2–7]. In particular, semiconductor quantum dot (QD: CdTe or CdSe/ZnS) SAMs have advantageous features in the field of luminescent materials [8–10]. However, compared to these traditional quantum dots, carbon quantum dots (CDs), as a new class of nanomaterial, possessed captivating properties such as excellent photostability, low toxicity, low cost, and easy synthesis [11, 12]. Recently, the self-assembly monolayers of the carbon nanoparticles on metal surfaces hold great potential for novel electronic and optoelectronic properties [13–16]. However, there is rarely any report about the methods of CD self-assembled films.

Here, we developed a simple and one-pot synthesis of carbon dot self-assembled monolayer films (CD-SAMFs). By using styrene both as the reactant (carbon source) and oil phase medium, the CD-SAMFs formed at the oil-water interfaces through copper acetate and hydrogen peroxide ($Cu(Ac)_2$-H_2O_2) catalytic oxidation. Without modified agents or harsh conditions (such as Chemical Vapor Deposition (CVD), electrophoresis deposition, and layer-by-layer (LBL) self-assembly) [13–18], the as-produced hydroxyl-enriched CDs can be spontaneously self-assembled into the carbon dot monolayer films via hydrogen bond interactions. The ultrathin CD-SAMFs (<10 nm) possessed brightly luminescent, highly transparent, and hydrophobic properties. Besides, this method can also help other benzene series including benzene, benzyl alcohol, and xylene be converted to CDs under the same conditions, which is an environmentally friendly way to reuse these volatile organic compound (VOC) wastes and is very promising for industrial application.

The one-pot synthesis of the CD-SAMFs is as follows: deionized water, $Cu(Ac)_2$, H_2O_2, and styrene were added to a 100 mL conical flask with stopper under stirring at 60 degrees Celsius. The system was sealed at the designated temperature for 12 hours. As shown in Figure 1(a), when the H_2O_2 was added into the blue $Cu(Ac)_2$ solution, the color

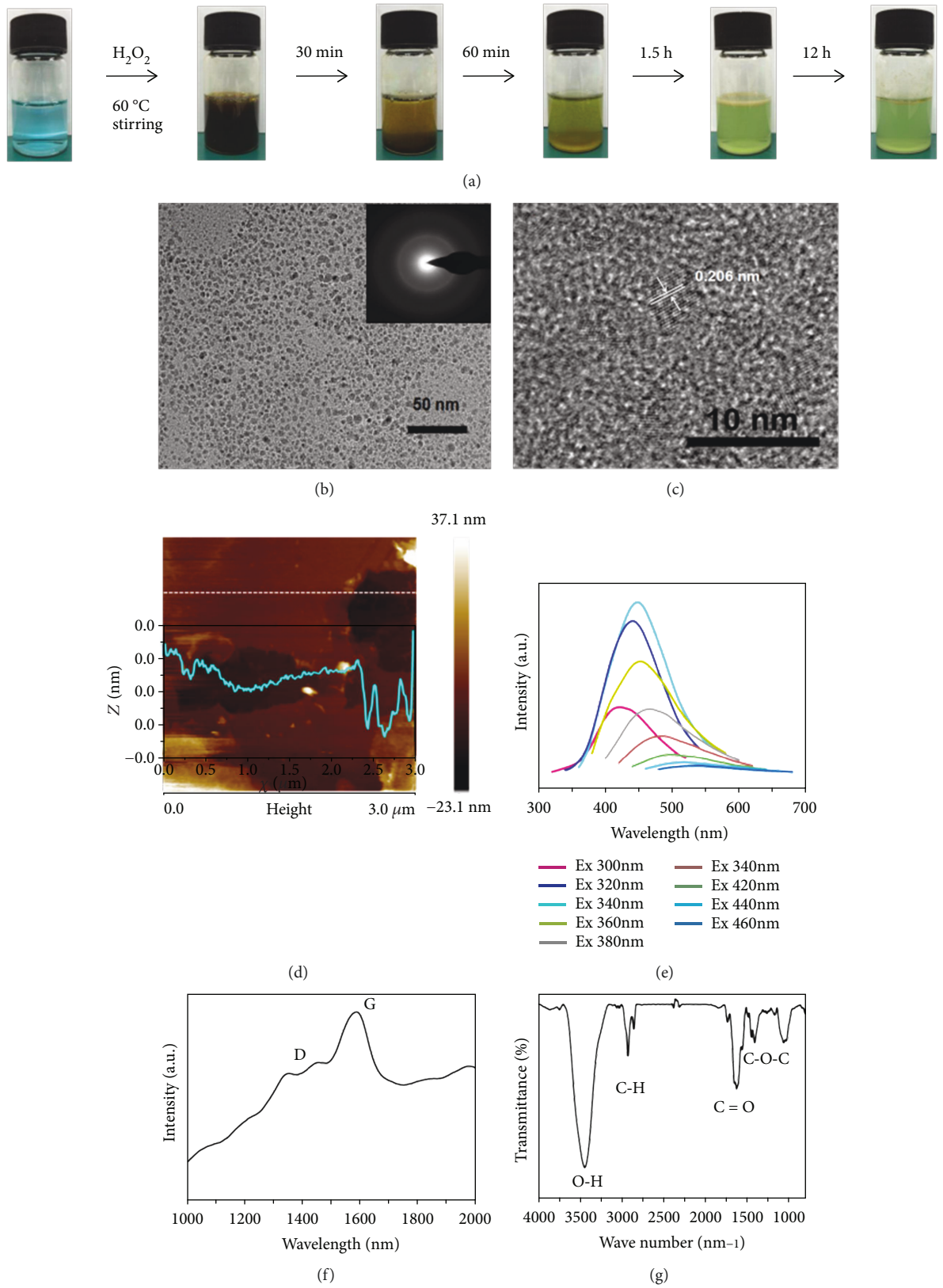

Figure 1: Preparation and structural characterization of CD-SAMFs: (a) Synthetic procedure; (b, c) HRTEM images and SAED; (d) AFM images, inset: height profile of cross-sections of the monolayers, *Z*: height (nm); *s*: distance (μm); (e) PL emission spectra based on different excitation wavelength; (f) Raman spectrum; (g) FTIR spectrum.

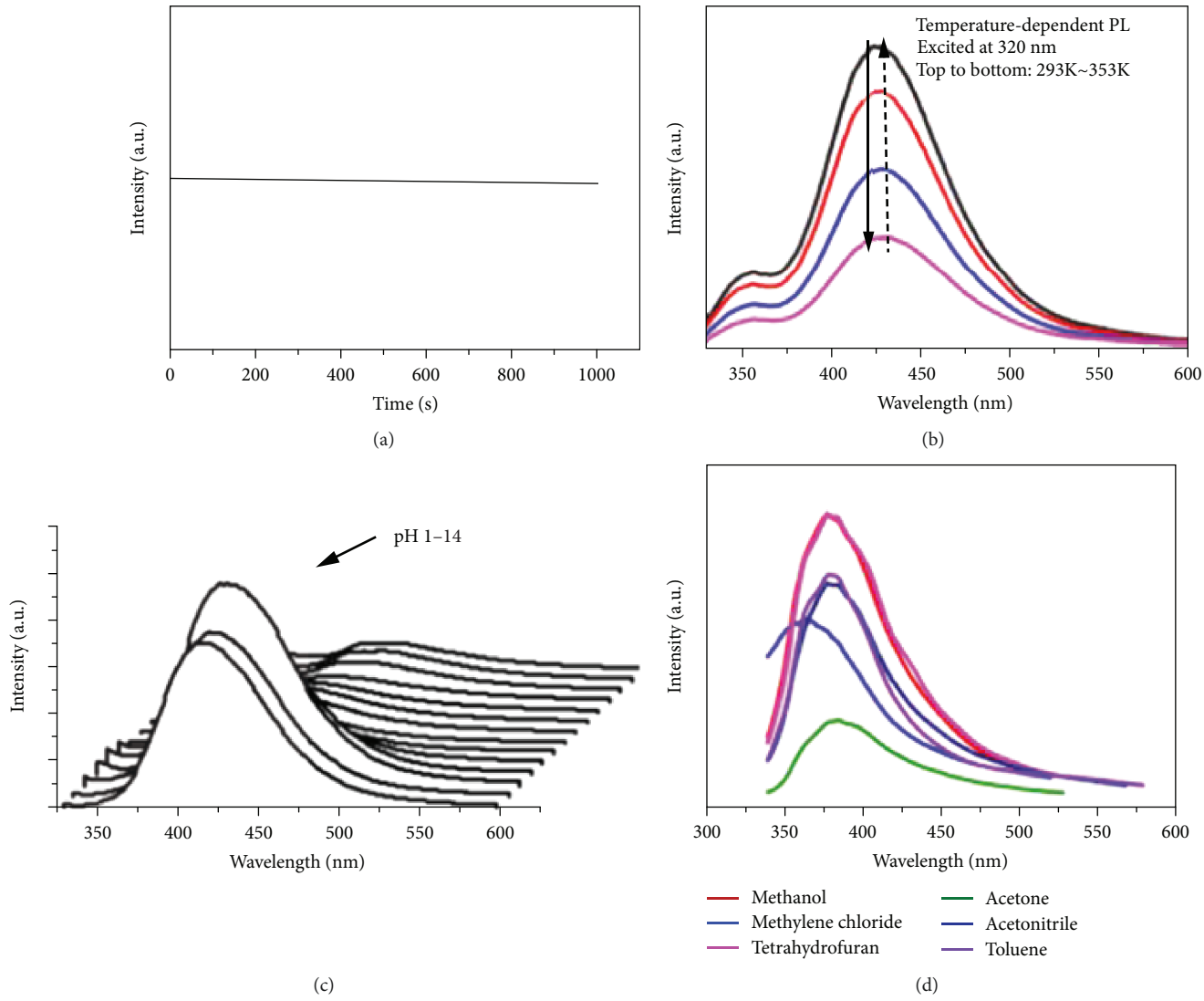

Figure 2: PL properties of CD-SAMFs: (a) time-based PL spectrum; (b) temperature-dependent PL spectra from 293 to 353 K at 320 nm excitation; (c) pH-dependent PL spectra; (d) PL emission spectra of CD-SAMFs dispersed in different polar solvents.

of the solution rapidly turned from blue to red brown, then became yellow. About one and a half hour later, the solution turned green eventually. Some cream-colored products were suspended on the surface of the solution. It is possible that a lot of copper intermediates of different oxidation state were produced; meanwhile, a large quantity of CDs was produced, which then self-assembled to the carbon dot nanofilms at the oil-water interfaces between the styrene oil phase and the solution. As shown in Figures 1(b) and 1(c), the high-resolution transmission electron microscopy (HRTEM) images revealed that the CDs were self-assembled to the ultrathin carbon dot nanofilms. The CDs were well dispersed with a Gaussian size distribution and an average size of 4.75 ± 0.58 nm (Figure S1), which presented good uniformity. HRTEM images confirmed the CDs' crystalline nature and revealed a lattice spacing of 0.203 ± 0.003 nm (Figure 1(c)), which corresponds to the (111) diffraction plane of the diamond structure [19]. The atomic force microscope (AFM) images showed that the ultrathin carbon dot nanofilm was about <10 nm high (Figure 1(d) inset), which was consistent with the lateral sizes of the CDs and further demonstrated that the film was a monolayer. The resultant fluorescence spectra obviously showed that CD-SAMFs possessed a multiemission nature depending on the excitation wavelength, which might rely not only on the energy gap governed by the surface oxidation states and the size of the CDs [20] but also on the different emissive sites on each carbon dot [21] (Figure 1(e) and Figure S2 for other benzene series VOCs). As the excitation wavelength changed from 300 nm to 500 nm, the emission exhibited an obvious red shift from 400 nm to 540 nm correspondingly, which displayed an emission maximum at 450 nm under excitation at wavelength 340 nm. The UV-Vis spectra of benzene series-CDs presented a broad absorption band (200-600 nm) as previously reported [21]. A clear shoulder absorption peak of styrene CDs at 230 nm was attributed to the π-electron system, suggesting the existence of the sp^2 aromatic

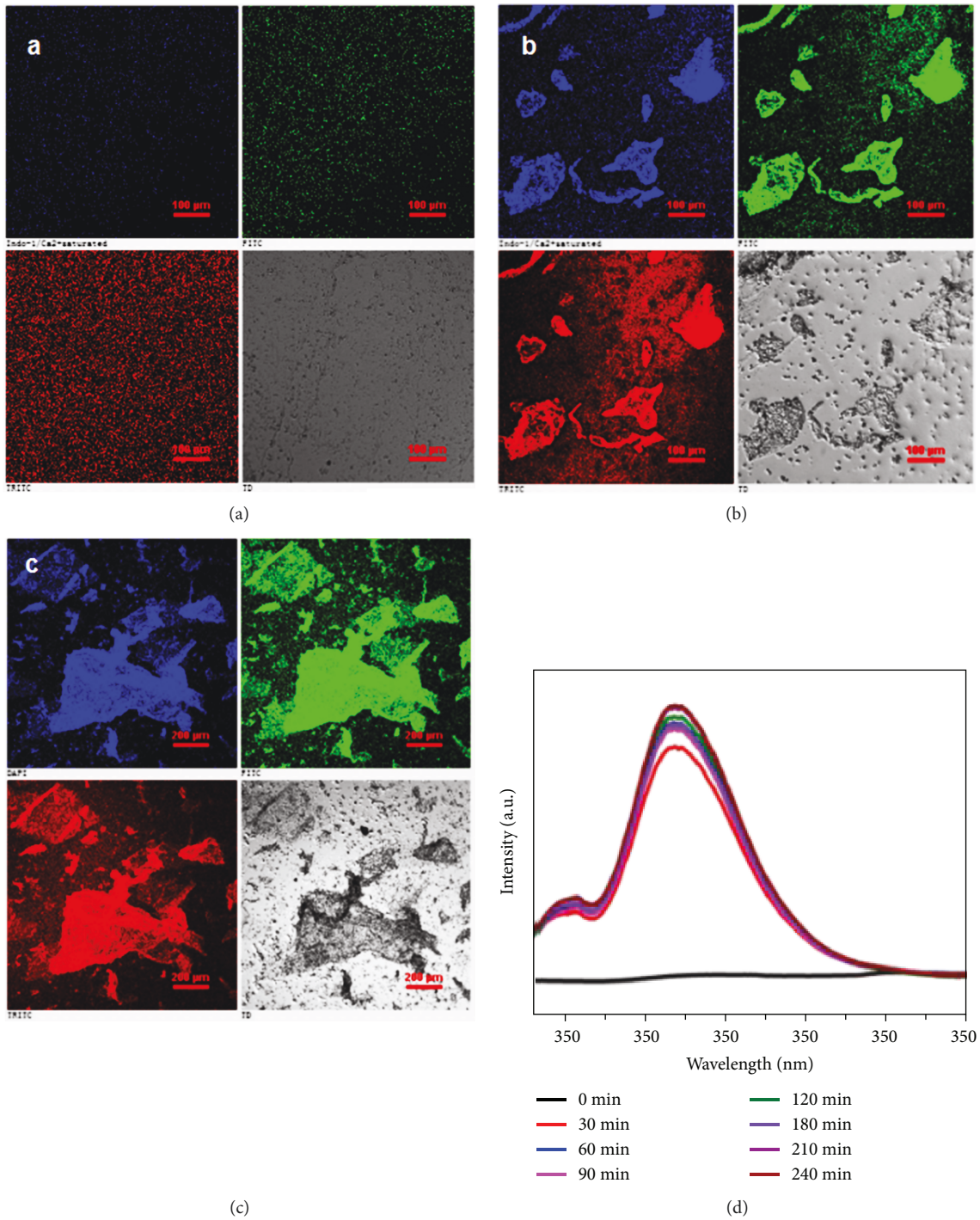

FIGURE 3: Fluorescent images of CD-SAMFs at different reaction times: (a) 10 min, (b) 60 min, (c) 12 h, and (d) PL emission spectra of CD-SAMFs (Ex = 340 nm). Scale: (a, b) 100 μm, (c) 200 μm.

structure units [22], which might originate from the impurities of the styrene (Figure S2). As shown in Figure 1(f), a strong Raman signature from the G band assigned to sp^2 carbons appeared at the energy peak of 1590 cm^{-1}. Its intensity was much higher than the sp^3 Raman peak (D band at 1338 cm^{-1}), which indicated the large degree of graphitization of CDs (Figure S3) [23]. FTIR results further indicated that all the CDs are abundant oxygen-containing functional groups (carbonyl and hydroxyl group) (Figure 1(g) and Figure S4).

The CD-SAMFs possessed high photostability at 1000s (Figure 2(a)) and reversible thermosensitivity with the temperature varying from 293 K to 393 K (Figure 2(b)). Another interesting phenomenon was the pH-dependent behavior as the PL intensities increased in solutions with high pH values, while they almost kept stable when the pH was changed from

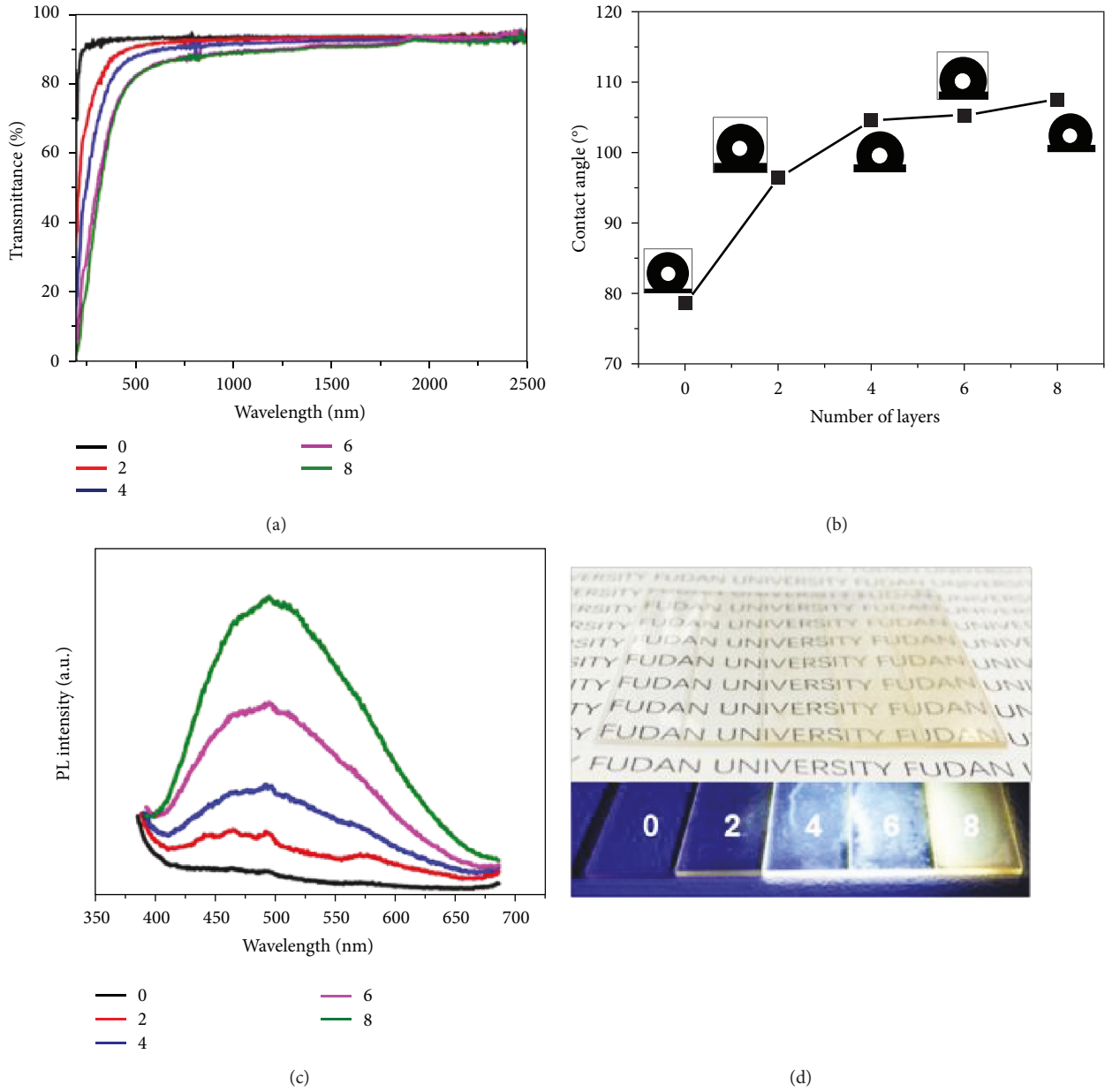

Figure 4: Optical transmittance and hydrophobicity test. (a) Transmittance of the control (quartz glass) and multilayer CD-SAMFs on the quartz glass. (b) Water contact angle of the control and CD-SAMFs on the quartz glass. (c) PL emission spectra of CD-SAMFs (Ex = 365 nm). (d) Photographs of these CD-SAMFs under visible light (top) and UV irradiation (365 nm) (down).

1 to 11 (Figure 2(c)). Without any surface passivation, the acquired CDs exhibited fluorescent properties and well dispersion in organic solvents (such as methanol, methylene chloride, tetrahydrofuran, acetone, acetonitrile, and toluene) (Figure 2(d)).

The formation mechanism of the CD-SAMFs in the $Cu(Ac)_2$-H_2O_2 system is through the catalytic-oxidation reaction at the oil-water interfaces. Different from the self-assembled nanospheres via CDs in a copper sulfate and hydrogen peroxide ($CuSO_4$-H_2O_2) catalytic-oxidation system as our previous work presented [24], copper acetate is a weak acid and weak base salt (pH 4.8), so the divalent copper ion and the acetate radical were hydrolyzed to form copper hydroxide and acetic acid firstly (step 1). When H_2O_2 was added to the solution, the whole possible reaction could be proposed as follows:

$$Cu(C_2H_3O_2)_2 + 2H_2 \rightleftharpoons Cu(OH)_2 + 2CH_3COOH \quad (1)$$

$$Cu(OH)_2 + H_2O_2 \rightarrow CuO_2 + 2H_2O \quad (2)$$

$$2CuO_2 \triangleq 2CuO + O_2\uparrow \quad (3)$$

$$3CuO + 4CH_3COOH + 4H_2O \rightarrow \left[2Cu(C_2H_3O_2)_2\right] \cdot [CuO] \cdot [6H_2O] \quad (4)$$

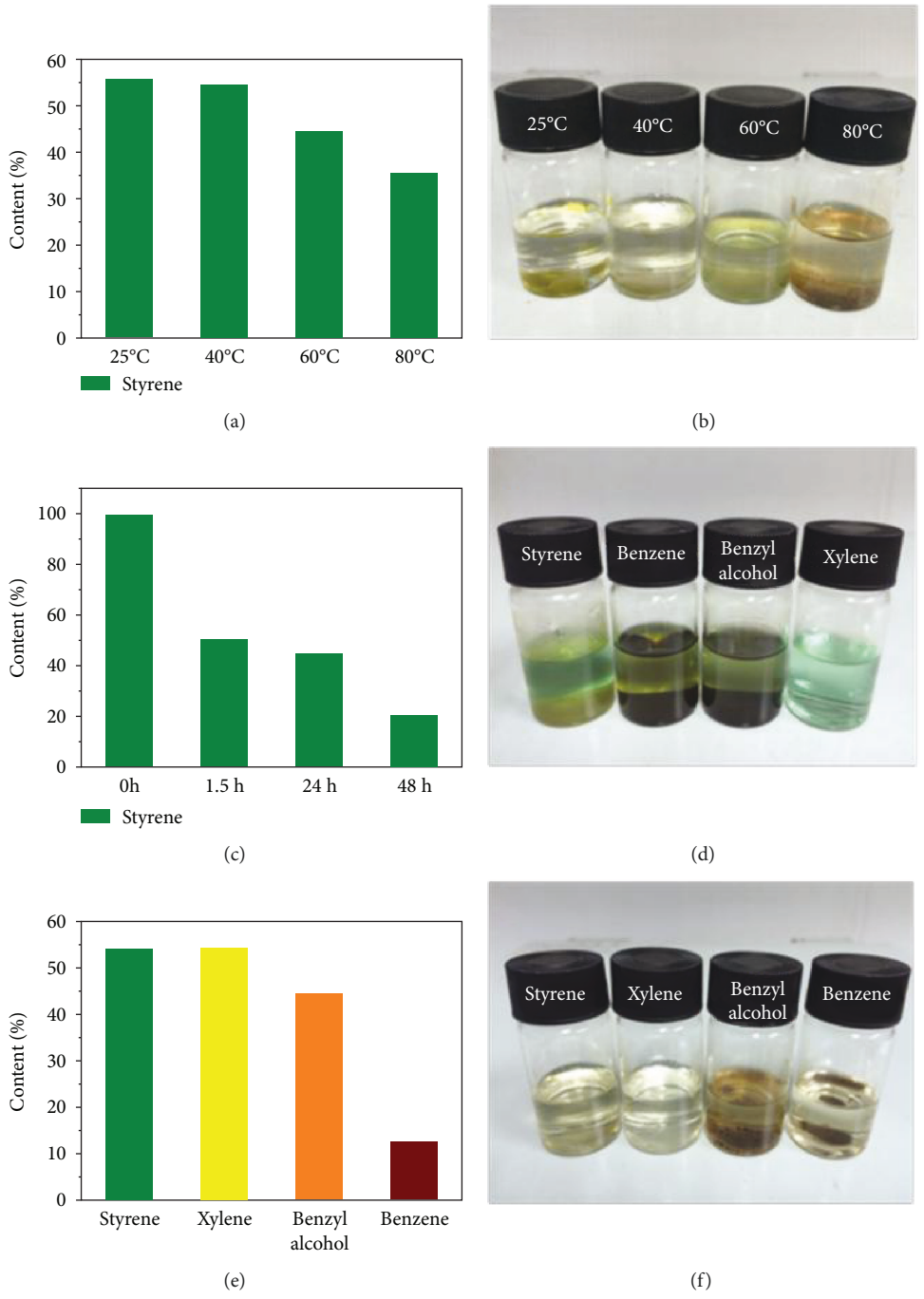

Figure 5: Degradation of benzene series VOCs by GC-MS test. (a, b) The content and the photograph of the styrene after reaction at different temperatures (24 h). (c) The content of styrene after reaction at different reaction times at 60°C. (d–f) The raw solution, the content, and the butyl acetate extract of benzene series VOCs after reaction (24 h) at 25°C, respectively.

Then, copper hydroxide reacted with hydrogen peroxide to form copper peroxide (step 2). With the heating of the reaction process, the brown copper peroxides decomposed, accompanied by a large amount of heat and O_2 (step 3). In the weak acid solution, the resulting copper oxide reacted with acetic acid to form copper acetate. Meanwhile, a large amount of oxygen produced in the whole process acted as the oxidant for the oxidation of the styrene, resulting in the formation of carbon clusters C_2, C_3, C_2H_2, other small molecules, and hydrogen ions, which finally crystallized into CDs in the solution rather than further be oxidized into COx owing to the weak oxidation of the O_2. In addition, the brownish copper peroxide gradually disappeared after the reaction, and the solution became green instead of the original blue, which means the basic copper acetate salts ($[2Cu\ (C_2H_3O_2)_2]\cdot[CuO]\cdot[6H_2O]$) were formed (step 4).

During the reaction process, more and more CDs are produced. As the unreacted reactant styrene and the solution

formed two phases, self-assembled CD monolayer films appeared at the oil-water interfaces. As is shown in Figure 3, the fragments of the CD-SAMFs were first formed after 60 minutes as observed by the fluorescence microscope (Figures 3(a) and 3(b)). Then, about 12 hours later, these small fragments self-assembled into large-scale monolayer films (Figure 3(c)). In general, the fluorescence of CDs is always strongly quenched when large quantities of CDs are deposited on glass, metal, silicon, or plastic substrates owing to the formation of aggregates. However, the bright emission of the CD-SAMFs may have resulted from the self-assembly of the CDs via hydrogen bonding interaction, preventing aggregation-induced quenching [25, 26]. The fluorescence spectra also recorded this phenomenon exactly. About 60 minutes later, the fluorescence emission intensity dramatically rose to almost the maximum and then increased gently within four hours (Figure 3(d)).

Moreover, the CD-SAMFs possessed high transparency and hydrophobicity. As is shown in Figure 4(a), the transmittance of these CD-SAMFs decreased slowly with the multilayer number varying from 2 to 8. And the transmittance of different numbers of multilayers was all above 80% at the UV-Vis and near infrared band (>480 nm), which indicated that the CD-SAMFs can become favorable candidates for optics applications [27]. In addition, it was found that the water contact angle (WCA) with increasing multilayer CD-SAMFs was increased from 98° to 108° (>90°), which means the ultrathin CD nanofilms possessed a hydrophobic surface (Figure 4(b)). Like the diamond-like carbon (DLC) films, the good transparency and hydrophobicity of the CD-SAMFs is possibly attributed to the diamond-like structures of the CDs [28]. Although small vacancies between adjacent CDs and the aggregation still existed, the WCA of the multilayer CD-SAMFs increased with the increasing number of the multilayers. It is possible that the multilayer CD-SAMFs make up for those minor defects in the CD monolayer [10]. Moreover, the PL emission spectra of CD-SAMFs showed that the PL intensities of the fluorescence bands at about 500 nm increased gradually with the increasing number of multilayers n and the CD-SAMFs emitted green light under UV irradiation (Figures 4(c) and 4(d)). Additionally, it was noteworthy that there was no significant shift or broadening of the emission band for different values of n, which demonstrated that there were no obvious changes in intermolecular interactions or of the nature of CDs in the whole assembly process as per previous reports [10].

What is more, this method may also provide a new approach to highly effectively degrade benzene series VOC waste water. During the reaction, the higher the temperature, the more CDs are produced. As is shown in Figure 5, when the temperature was increasing from 25°Cto 80°C, the styrene was greatly reduced from 56% to 36% after the reaction for 24 h (Figures 5(a) and 5(b)). Keeping the reaction temperature at 60°C, Figure 5(c) indicates that the content of styrene decreased from 51% to 21% along the reaction from 1.5 h to 48 h. Other benzene series VOCs could also be converted to CDs (Table S1), and the content of the xylene and benzyl alcohol was about 55% and 45%, respectively, but the content of benzene was greatly decreased to 12.8% after 24 h reaction at 25°C, which was possibly attributed to the stronger reducibility than that of other benzene series (Figures 5(d)–5(f)).

2. Conclusions

In summary, we have developed a facile and one-pot synthesis of PL CD-SAMFs at the oil-water interfaces by $Cu(Ac)_2$-H_2O_2 catalytic-oxidation reaction. Different from the semiconductor QDs, the hydroxyl-enriched CDs can be spontaneously self-assembled to the carbon dot monolayer films via hydrogen bond interactions at the oil-water interfaces without any surface modification. The as-produced CD-SAMFs by the diamond-like CDs possessed ultrathin thickness (<10 nm), which was comparable to the diamond-like carbon (DLC) films. With increase of the multilayer number, the PL intensities and the hydrophobicity were also enhanced. Moreover, their superior performances with high transparency and hydrophobicity showed potential application for multifunctional coating films, anticounterfeiting, displays, sensors, and optical devices. What is more, it is effective not only for removing organic contaminants (such as VOCs) but also for reducing the industrial waste gas CO_2 emissions which greatly protects the environment.

Data Availability

(1) The HRTEM, AFM, PL spectra, Raman, FTIR, and fluorescent image data used to support the findings of this study are included within the article. (2) The additional HRTEM, UV-Vis spectra, Raman, FTIR, and GC-MS of other benzene series data used to support the findings of this study are included within the supplementary information file(s). (3) Previously reported data were used to support this study and are available at [doi:10.1039/c8ra03723j]. These prior studies (and datasets) are cited at relevant places within the text as references [20].

Additional Points

Notes and References. In a typical procedure, styrene (0.208 g, Aladdin, purity > 98%) and H_2O_2 (400 μL) were added to $Cu(Ac)_2$ (0.4g) solution (10 mL) at 60°C under stirring for 12 h. The final CD-SAMFs were purified by extracting with butyl acetate and water several times to remove the impurities including the residual organic and inorganic molecules. Then, the purified CD-SAMFs were dried at 60°C for structural characterization and measurements. The synthetic procedure for the CDs by using other benzene series VOCs was similar to that of the styrene CDs except for the addition of different benzene series in the same media: 0.2 mol/L benzene, 0.2 mol/L benzyl alcohol, and 0.2 mol/L xylene.

Conflicts of Interest

There are no conflicts to declare.

Supplementary Materials

Figure S1: HRTEM of carbon dot self-assembled monolayer films (CD-SAMFs). (a, b) The related size distribution of carbon dots in the CD-SAMFs. Figure S2: UV-Vis spectra of the benzene series (a) and PL emission spectra of CDs by other benzene series: (b) benzene, (c) benzyl alcohol, and (d) xylene. Figure S3: Raman spectra of CDs synthesized by other benzene series. Figure S4: FTIR spectra of CDs synthesized by other benzene series. Table S1: GC-MS test. *(Supplementary Materials)*

References

[1] K. S. Novoselov, D. Jiang, F. Schedin et al., "Two-dimensional atomic crystals," *Proceedings of the National Academy of Sciences of the United of America*, vol. 102, no. 30, pp. 10451–10453, 2005.

[2] L. Hu, M. Chen, W. Shan et al., "Stacking-order-dependent optoelectronic properties of bilayer nanofilm photodetectors made from hollow ZnS and ZnO microspheres," *Advanced Materials*, vol. 24, no. 43, pp. 5872–5877, 2012.

[3] H. Bao, C. M. Li, X. Cui, Q. Song, H. Yang, and J. Guo, "Single-crystalline Bi_2S_3 nanowire network film and its optical switches," *Nanotechnology*, vol. 19, no. 33, article 335302, 2008.

[4] A. A. Tahir, M. A. Ehsan, M. Mazhar, K. G. U. Wijayantha, M. Zeller, and A. D. Hunter, "Photoelectrochemical and photoresponsive properties of Bi_2S_3 nanotube and nanoparticle thin films," *Chemistry of Materials*, vol. 22, no. 17, pp. 5084–5092, 2010.

[5] S. Sahoo, S. Husale, B. Colwill, T. M. Lu, S. Nayak, and P. M. Ajayan, "Electric field directed self-assembly of cuprous oxide nanostructures for photon sensing," *ACS Nano*, vol. 3, no. 12, pp. 3935–3944, 2009.

[6] W. Tian, C. Zhang, T. Zhai et al., "Flexible SnO_2 hollow nanosphere film based high-performance ultraviolet photodetector," *Chemical Communications*, vol. 49, no. 36, pp. 3739–3741, 2013.

[7] W. Tian, T. Zhai, C. Zhang et al., "Low-cost fully transparent ultraviolet photodetectors based on electrospun ZnO-SnO_2 heterojunction nanofibers," *Advanced Materials*, vol. 25, no. 33, pp. 4625–4630, 2013.

[8] H. Y. Kim, D.-E. Yoon, J. Jang et al., "Quantum dot/siloxane composite film exceptionally stable against oxidation under heat and moisture," *Journal of the American Chemical Society*, vol. 138, no. 50, pp. 16478–16485, 2016.

[9] R. Liang, D. Yan, R. Tian et al., "Quantum dots-based flexible films and their application as the phosphor in white light-emitting diodes," *Chemistry of Materials*, vol. 26, no. 8, pp. 2595–2600, 2014.

[10] X. Liu, X. Zhang, R. Wu et al., "All-quantum-dot emission tuning and multicolored optical films using layer-by-layer assembly method," *Chemical Engineering Journal*, vol. 324, pp. 19–25, 2017.

[11] S. Y. Lim, W. Shen, and Z. Gao, "Carbon quantum dots and their applications," *Chemical Society Reviews*, vol. 44, no. 1, pp. 362–381, 2015.

[12] S. N. Baker and G. A. Baker, "Luminescent carbon nanodots: emergent nanolights," *Angewandte Chemie International Edition*, vol. 49, no. 38, pp. 6726–6744, 2010.

[13] L. Camilli, J. H. Jørgensen, J. Tersoff et al., "Self-assembly of ordered graphene nanodot arrays," *Nature Communications*, vol. 8, no. 1, p. 47, 2017.

[14] B. Wang, Y. Chen, Y. Wu et al., "Aptamer induced assembly of fluorescent nitrogen-doped carbon dots on gold nanoparticles for sensitive detection of AFB_1," *Biosensors and Bioelectronics*, vol. 78, pp. 23–30, 2016.

[15] K. T. Narasimha, C. Ge, J. D. Fabbri et al., "Ultralow effective work function surfaces using diamondoid monolayers," *Nature Nanotechnology*, vol. 11, no. 3, pp. 267–272, 2016.

[16] J. Mao, X. Y. Kong, D. Wang, and Z. Zou, "Assembly of metallic carbon nanodots aligned on a vicinal Si (111)-7×7 surface," *Journal of the American Chemical Society*, vol. 129, no. 13, pp. 3782-3783, 2007.

[17] L. Schmidlin, V. Pichot, S. Josset et al., "Two-dimensional nanodiamond monolayers deposited by combined ultracentrifugation and electrophoresis techniques," *Applied Physics Letters*, vol. 101, no. 25, article 253111, 2012.

[18] C. J. Tang, S. M. S. Pereira, A. J. S. Fernandes et al., "Synthesis and structural characterization of highly <100>-oriented {100}-faceted nanocrystalline diamond films by microwave plasma chemical vapor deposition," *Journal of Crystal Growth*, vol. 311, no. 8, pp. 2258–2264, 2009.

[19] N. R. Greiner, D. S. Phillips, J. D. Johnson, and F. Volk, "Diamonds in detonation soot," *Nature*, vol. 333, no. 6172, pp. 440–442, 1988.

[20] L. Bao, C. Liu, Z.-L. Zhang, and D.-W. Pang, *Advanced Materials*, vol. 27, no. 10, pp. 1663–1667, 2015.

[21] Y.-P. Sun, B. Zhou, Y. Lin et al., "Quantum-sized carbon dots for bright and colorful photoluminescence," *Journal of the American Chemical Society*, vol. 128, no. 24, pp. 7756-7757, 2006.

[22] S. C. Hess, F. A. Permatasari, H. Fukazawa et al., "Direct synthesis of carbon quantum dots in aqueous polymer solution: one-pot reaction and preparation of transparent UV-blocking films," *Journal of Materials Chemistry A*, vol. 5, no. 10, pp. 5187–5194, 2017.

[23] W. Y. Fan, J. Röpcke, and P. B. Davies, "Effect of oxygen on methyl radical concentrations in a CH_4/H_2 chemical vapor deposition reactor studied by infrared diode laser spectroscopy," *Journal of Vacuum Science & Technology A: Vacuum, Surfaces, and Films*, vol. 14, no. 5, pp. 2970–2972, 1996.

[24] H. Guo, B. You, S. Zhao et al., "Full-color tunable photoluminescent carbon dots based on oil/water interfacial synthesis and their applications," *RSC Advances*, vol. 8, no. 42, pp. 24002–24012, 2018.

[25] S. Zhu, Q. Meng, L. Wang et al., "Highly photoluminescent carbon dots for multicolor patterning, sensors, and bioimaging," *Angewandte Chemie*, vol. 125, no. 14, pp. 4045–4049, 2013.

[26] S. Qu, X. Wang, Q. Lu, X. Liu, and L. Wang, "A biocompatible fluorescent ink based on water-soluble luminescent carbon nanodots," *Angewandte Chemie, International Edition*, vol. 51, no. 49, pp. 12215–12218, 2012.

[27] C. Popov, A. Gushterov, L. Lingys, C. Sippel, and J. P. Reithmaier, "Structural and optical properties of ultrananocrystalline diamond/InGaAs/GaAs quantum dot structures," *Thin Solid Films*, vol. 518, no. 5, pp. 1489–1492, 2009.

[28] G. Zhang, L. J. Guo, Z. Liu, and X. Zheng, "Application of diamond-like carbon film as protection and antireflection coatings of ZnS elements," *Optical Engineering*, vol. 33, no. 4, pp. 1330–1334, 1994.